

Ion Beam Sputter Deposition of Piezoelectric AlN Thin Films

By

NEHA SHARMA

Enrolment No: PHYS02 2011 04013

*A thesis submitted to the
Board of Studies in Physical Sciences*

In partial fulfillment of requirements

for the Degree of

DOCTOR OF PHILOSOPHY

of

HOMI BHABHA NATIONAL INSTITUTE



August, 2016

Homi Bhabha National Institute


Recommendations of the Viva Voce Committee

As members of the Viva Voce Committee, we certify that we have read the dissertation prepared by Neha Sharma entitled "Ion Beam Sputter Deposition of Piezoelectric AlN Thin Films" and recommend that it may be accepted as fulfilling the thesis requirement for the award of Degree of Doctor of Philosophy.

Chairman - Dr. Sitaram Dash

 Date: 27/02/2017

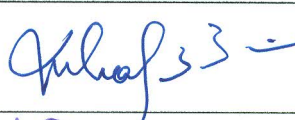
Guide / Convener - Dr. A. K. Tyagi

 Date: 27/02/2017

Examiner - <Name>

 Date: 27/2/2017

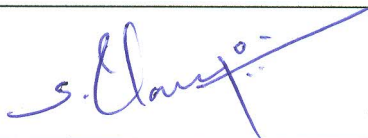
Member 1- Dr. M. Kamruddin

 Date: 27/2/17

Member 2- Dr. Sandip K. Dhara

 Date: 28/2/17

Technical Adviser- Dr. S. Ilango

 Date: 27/2/17.

Final approval and acceptance of this thesis is contingent upon the candidate's submission of the final copies of the thesis to HBNI.

I/We hereby certify that I/we have read this thesis prepared under my/our direction and recommend that it may be accepted as fulfilling the thesis requirement.

Date: 27/02/2017

Place: Kalpakkam

<Signature>

Guide



STATEMENT BY AUTHOR

This dissertation has been submitted in partial fulfillment of requirements for an advanced degree at Homi Bhabha National Institute (HBNI) and is deposited in the Library to be made available to borrowers under rules of the HBNI.

Brief quotations from this dissertation are allowable without special permission, provided that accurate acknowledgement of source is made. Requests for permission for extended quotation from or reproduction of this manuscript in whole or in part may be granted by the Competent Authority of HBNI when in his or her judgment the proposed use of the material is in the interests of scholarship. In all other instances, however, permission must be obtained from the author.



Neha Sharma

DECLARATION

I, hereby declare that the investigation presented in the thesis has been carried out by me. The work is original and has not been submitted earlier as a whole or in part for a degree / diploma at this or any other Institution / University.

Neha Sharma

Neha Sharma

List of Publications arising from the thesis

Journal

Published/Accepted

1. *Growth kinetics of ion beam sputtered Al-thin films by dynamic scaling theory*, Neha Sharma*, K. Prabakar, S. Dash, A.K. Tyagi, *Thin Solid Films* 573(2014) 84–89.
2. *Application of dynamic scaling theory for growth kinetic studies of AlN-thin films deposited by ion beam sputtering in reactive assistance of nitrogen plasma*, Neha Sharma*, K. Prabakar, S. Ilango, S. Dash, A.K. Tyagi, *Appl. Surf. Sci.*, 347 (2015) 875–879.
3. *Charged vacancy induced enhanced piezoelectric response of reactive assistive IBSD grown nanocrystalline AlN thin films*, Neha Sharma*, Martando Rath, S. Ilango, T. R. Ravindran, M. S. R. Rao, S. Dash and A. K. Tyagi, *Journal of Physics D: Applied Physics*, 50(2017) 015601.
4. *Optical band-gap and associated Urbach energy tails in defected AlN thin films grown by ion beam sputter deposition: Effect of assisted ion energy*, Neha Sharma*, K. Prabakar, S. Ilango, S. Dash and A.K. Tyagi, *Advanced Materials Proceedings*, Accepted (2016)

Under Review

5. *Optical band gap and associated band-tails in nanocrystalline AlN thin films grown by reactive IBSD at different substrate temperatures*, Neha Sharma*, Shilpam Sharma, K. Prabakar, S. Amirthapandian, S. Ilango, S. Dash and A. K. Tyagi, *Under Review, Material Science in Semiconductor Processing*
6. *XPS studies on AlN thin films grown by ion beam sputtering in reactive assistance of N^+/N_2^+ ions: Substrate temperature induced compositional variations*, Neha Sharma*, S. Ilango, S. Dash and A. K. Tyagi, *Under Review, Thin Solid Films*

Under Preparation

7. *Piezoelectric response of reactive assistive IBSD grown AlN thin films by XRD and C-V measurements*
Neha Sharma*, K. Prabakar, S. Ilango, S. Dash and A.K. Tyagi

Conferences

1. Annual General Meeting, MRSI -2013, IGCAR, Kalpakkam; *Reactive Ion Beam Sputter Deposition of AlN, TiN Thin Films.*
Neha Sharma*, S. Dash and A. K. Tyagi
2. Regional Conference of Young Scientists on Nanoscience & Nanomaterials, 2015, JNCASR, Bangalore; *Growth Kinetics of Ion Beam Sputtered Al and AlN thin films: Modifications due to reactive assistance of N₂ plasma.*
Neha Sharma*, K. Prabakar, S. Ilango, S. Dash and A. K. Tyagi
3. Bringing The Nanoworld Together (BTNT-2015), IITM, Chennai.
Neha Sharma*
4. Int. Conf. Mat. Sci. & Tech., 2016, DU, Delhi; *Spectrophotometry of nanocrystalline AlN thin films grown by reactive IBAD for piezoelectric device fabrication.*
Neha Sharma*, K. Prabakar, S. Ilango, S. Dash and A.K. Tyagi

Neha Sharma

To My Teachers

Who taught me to learn

ACKNOWLEDGEMENTS

I would like to thank my supervisor Dr. A. K. Tyagi for his guidance and constant encouragement during tenure of the thesis. I would like to express my deep and sincere gratitude to Dr. Sitaram Dash, for his encouragement, suggestions, scientific and technical discussions which helped me a lot in completing this dissertation.

I thank the Director, IGCAR for providing me the opportunity to continue the research work at IGCAR. I thank the Director, MSG for facilitating the research activities. I would like to express my sincere thanks to Dr. Baldev Raj and Dr. K. Laha to keep my moral high by their appreciations.

I would like to thank my colleagues and collaborators Dr. K. Prabakar for his help when it was needed the most, Dr. R. Ravindran, Dr. V. Sivasubramanian, Dr. S. Ilango, Dr. S. Amirthapandian, Ms. P. C. Clinsha, Dr. Shamima Hussain, Dr. Arindam Das, Dr. S. Abhaya, Sunitha and Twisha for their help in measurements and fruitful discussions on many parts of my thesis work. I am deeply indebted to Dr. M. S. R. Rao and his student Mr. Martando Rath at IIT, Madras for their unconditional help in piezo force microscopic measurements.

I am thankful to my parents and siblings for their support, love, encouragement and belief in me. Especially, my mother and elder sister, who took care of my son when he was just 3 months old. Last, but not least, I would like to thank my husband Dr. Shilpam Sharma who gave me strength and support during tough times. He not only motivated me but also played a vital role in completion of this dissertation.

CONTENTS

Title	Page No.
Synopsis	I
List of Figures	X
List of Tables	XVIII
CHAPTER 1 Piezoelectric Thin Films: An Overview	1-20
1.1 Need of Piezoelectric Thin Films	1
1.2 Piezoelectricity	2
1.3 Brief History of Piezoelectricity	3
1.4 Common Piezoelectric Thin Film Materials	5
1.4.1 Lead Zirconate Titanate (PZT)	5
1.4.2 Zinc Oxide (ZnO)	8
1.5 Piezoelectric Aluminum Nitride (AlN)	9
1.6 Piezoelectric AlN Thin Films for Energy Harvesting	14
References	15
CHAPTER 2 Thin Film Deposition and Characterization	21-53
2.1 Ion - Solid Interaction: Mechanism of Sputtering	22
2.2 Ion Beam Sputter Deposition System: Experimental Set-up	29
2.2.1 6 cm RF Ion Source	30
2.2.2 End-Hall Assisted Ion Source	31
2.2.3 RF Neutralizer	33
2.3 Deposition Modes in IBSD	33
2.4 Characterization Techniques	35
2.4.1 Atomic Force Microscopy (AFM)	35
2.4.2 Scanning Electron Microscopy (SEM)	37
2.4.3 X-ray Diffraction (XRD)	39
2.4.4 Transmission Electron Microscopy (TEM)	44
2.4.5 X-ray photoelectron Spectroscopy (XPS)	46
2.4.6 Positron Annihilation Lifetime Spectroscopy (PALS)	48

2.4.7	Photoluminescence Spectroscopy	49
2.4.8	UV-VIS Spectrophotometer: Design and working principle	51
	References	52
CHAPTER 3	Growth Kinetics of Ion Beam Sputtered AlN Thin Films	54-87
3.1	Definition of Thin Film: A semantic problem	55
3.2	Thin Film Growth Process	56
3.3	Growth Kinetics: Dynamic Scaling Theory (DST)	57
3.3.1	Theoretical Background	60
3.4	Growth kinetics of aluminum (Al) thin films by DST	63
3.4.1	Aluminum (Al) - Thin Film Deposition	63
3.4.2	Observations and Discussion	64
3.5	Growth Kinetics of Aluminum Nitride (AlN) Thin Films by DST	73
3.5.1	AlN - Thin Film Deposition	74
3.5.2	Observations and Discussion	75
3.6	Conclusion	83
	References	85
CHAPTER 4	Growth Optimizations of AlN Thin Films by Reactive Assistive IBSD	88-119
4.1	Optimization of Assisted Ion Energy	89
4.2	Optimization of Substrate Temperature	90
4.3	Optimization of Deposition Time	114
4.4	Conclusion	116
	References	117
CHAPTER 5	Spectrophotometry of Reactive Assistive IBSD Grown AlN Thin Films	120-140
5.1	Reflection and Its Analysis	121
5.2	Deposition of AlN Thin Films	124
5.3	Calculation of Optical Band Gap Energy (E_g)	124
5.4	Determination of Urbach (E_u) and Weak Absorption Tail Energy (E_t)	129
5.5	Refractive Index and Extinction Coefficient	133

5.6 Conclusion	137
References	138
CHAPTER 6 Piezoelectric Properties of Reactive Assistive IBSD Grown AlN Thin Films	141-174
6.1 The Piezoelectric Effect	142
6.2 Mathematical Formulation of Piezoelectricity: The Piezoelectric Coefficients	143
6.3 Tensor Form of Piezoelectric Coefficient ' <i>d</i> '	146
6.4 Physical Significance of Piezoelectric Coefficients <i>d</i> ₃₃ , <i>d</i> ₃₁ and <i>d</i> ₁₅	148
6.5 Why Piezoelectric Aluminum Nitride (AlN) Thin Films?	150
6.6 Specimen Preparation	152
6.6.1 For PFM Studies	152
6.6.2 For XRD and C-V Measurements	153
6.7 Crystallographic Investigations on AlN Thin Films	154
6.8 Piezo Force Microscopy (PFM) on AlN Thin Films	155
6.9 Measurement of Longitudinal Piezoelectric Coefficient Using XRD	159
6.10 Longitudinal Piezoelectric Coefficient by C-V Measurements	163
6.11 Origin of High Piezoelectricity in a-axis Oriented AlN Thin Films	165
6.12 Conclusion	170
References	171
CHAPTER 7 Summary and Future Scope	175-177

SYNOPSIS

The continuing reduction in size and power consumption of complementary metal oxide semiconductor (CMOS) circuitry has led to a focused research on piezoelectric material based electromechanical transduction. Over the last few decades, bulk piezoelectric materials have been widely employed for the fabrication of a diverse range of macroscale transducers and microelectromechanical systems (MEMS). Major technological challenges have emerged as MEMS architecture is miniaturized with increased integration density for addressing the requirements of fast response and large motions. Continued down scaling to nanoelectromechanical systems (NEMS) requires revolutionary advances in the field of transducers. This has necessitated the development of high quality piezoelectric thin films. The thin films and multilayered hetrostructures of piezoelectric materials have emerged as efficient candidates for electromechanical transduction coupled to micro-machinability through standard processing tool. MEMS and NEMS based on piezoelectric thin films provide the required large linear forces with fast actuation at small drive voltages.

In this context, the most common piezoelectric material used for making macroscale transducers is Lead Zirconate Titanate (PZT). But PZT has several drawbacks when put to micro- and nanoscale fabrication of electronic devices. Some of the difficulties are, (i) processing and integration into thin film configuration with silicon as a substrate, (ii) low quality factors for some of the important RF based applications, (iii) special concerns with regard to IC fabrication owing to contamination risks encountered in CMOS fabrication

process. Thin film Zinc Oxide (ZnO) also suffers from similar issues and its reactivity with other IC materials has made it hard to integrate with standard CMOS process.

With the introduction of Aluminum Nitride (AlN) and especially the commercial success of the thin film bulk acoustic wave resonators (TFBAR or FBAR), interest in piezoelectric AlN thin film based micro- and nanoscale devices has blossomed. Unique aspects of AlN thin films which make it attractive for MEMS/NEMS applications are following:

- i. Ability to be deposited directly on silicon.
- ii. High mechanical quality factor (Q_m)
- iii. High Curie temperature ($T_c > 1000^\circ\text{C}$)
- iv. Free from any toxic element enabling contamination free device fabrication.
- v. Though AlN thin films possess a small coupling coefficient (k) but the ratio k^2/ϵ , where ϵ is the dielectric constant, is comparable to those of PZT thin films.

Thus for the growth of AlN thin films on silicon, the quest for appropriate and reproducible physical vapor deposition (PVD) technique has resulted in the evolution of ion beam sputter deposition (IBSD). IBSD is one of the best techniques to deposit device quality thin films with smooth surface and clean interface.

To this end, main motivation behind present thesis is to explore the deposition feasibility of piezoelectric AlN thin films by IBSD under reactive

assistance of N^+/N_2^+ ions. Growth kinetics of AlN thin films has been investigated to delineate the role of N^+/N_2^+ ions on growth characteristics. For this, films were grown for different durations and growth governing phenomena was identified at each stage using dynamic scaling theory (DST). Concomitantly, deposition parameters were optimized for the growth of highly textured wurtzite AlN thin film on Si(100) substrate with a preferred orientation. Their morphological, structural and compositional analyses have been carried out using an array of analytical techniques like atomic force microscopy (AFM), scanning electron microscopy (SEM), X-ray diffraction (XRD), high resolution transmission electron microscopy (HR-TEM) and X-ray photoelectron spectroscopy (XPS). Presence of defects in film microstructure was investigated with positron annihilation and photoluminescence (PL) spectroscopies. The optical band-gap with associated band tails formed by Urbach energy and weak absorption transitions along with refractive index and extinction coefficient were determined using UV-VIS spectrophotometry. Finally, piezo response of IBSD grown AlN thin films was explored using three different techniques. These are, (i) Piezo Force Microscopy (PFM) - an atomic force microscope (AFM) based technique. Piezo response loops were obtained to find out effective values of longitudinal piezoelectric coefficient ($d_{33(eff)}$), (ii) Capacitance-Voltage (C-V) measurements on Ti/AlN/Ti/Si(100) capacitive heterostructures to deduce change in capacitance which was correlated to the change in film dimensions for extracting $d_{33(eff)}$, and (iii) XRD based characterization where change in full width at half maxima

(FWHM) of rocking curves upon application of DC bias voltage (V_{DC}) was used to calculate $d_{33(eff)}$.

Findings of this dissertation demonstrate the technical feasibility of synthesizing a metal-insulator-metal heterostructure by sandwiching AlN thin film between Ti-electrodes by using reactive assisted IBSD to obtain high $d_{33(eff)}$ comparable to PZT based piezoelectric ceramics. This Thesis is organized into seven chapters. Following sections describe highlights of each chapter.

Chapter 1: Piezoelectric Thin Films: An Overview

This introductory chapter provides a brief account of the need of piezoelectric thin films along with historical perspective on piezoelectricity. Commonly used piezoelectric materials like lead Zirconate Titanate (PZT), zinc oxide (ZnO) and difficulties encountered in their integration into thin film form on silicon are discussed. Review on PZT and ZnO thin films and their piezo responses are presented. Interest in piezoelectric aluminum nitride (AlN) thin films for fabrication of miniaturized electronic devices for electromechanical transduction is presented. Various physical vapor deposition (PVD) techniques for the reproducible growth of piezoelectric thin films are reviewed. Ion beam sputter deposition (IBSD) technique is discussed with respect to its superiority over other PVD techniques. Possible contribution of piezoelectric AlN thin films towards energy harvesting is touched upon.

Chapter 2: Thin Film Deposition and Characterization

This chapter describes the ion beam sputter deposition technique and experimental set-ups used for thin film characterization. Construction of IBSD

unit along with 6 cm RF and end-hall type DC ion sources is described. Deposition of AlN thin films directly on Si(100) substrate is described. Also, parameter optimizations of deposition to obtain Ti/AlN/Ti/Si(100) heterostructures is presented. AFM and SEM have been employed to observe the surface morphology at different growth conditions. HR-TEM has been used to determine the crystallographic phase and average crystallite size of IBSD grown AlN thin films at different substrate temperatures. Fraction of AlN on film surface was determined from XPS. Different geometries of XRD have been employed to investigate the wurtzite hexagonal phase of AlN thin films on Si(100) substrates. This includes texture analysis and pole figures. Due to inherent ion beam induced effects of IBSD, generation of defects in film microstructures was explored by positron annihilation and photoluminescence (PL) spectroscopies. Finally, piezoelectric response of Ti/AlN/Ti/Si(100) heterostructures was analysed using three different techniques, namely, PFM, XRD and C-V measurement. The experimental procedure followed in each of these techniques is discussed.

Chapter 3: Growth Kinetics of Ion Beam Sputtered AlN Thin Films

This chapter reports the growth kinetics of Al- and AlN -thin films in the framework of Dynamic Scaling Theory (DST) to delineate the effect of reactive assistance of N^+/N_2^+ ions. Both the films, Al and AlN were grown on Si(100) substrates for 3, 5, 8 and 15 minutes. Their surface morphologies were observed using AFM and analysed to determine the growth governing phenomenon at each deposition time. A theoretical background of DST as propounded by Family and Vicsek in 1985 is presented. Scaling relations among surface roughness (δ),

deposition time (t) and scale of measurements (L) were used to extract the static (α) and dynamic (β) scaling exponents to unravel the underlying growth characteristics. A quantitative representation on the height variation and lateral correlation is provided by the '*autocovariance function $G(r)$* ' which at different scales provides a quantitative description of correlation among heights at different points on a surface as a function of their separation ' r '. The Fourier transform of $G(r)$ yields '*power spectral density (PSD) function $g(q)$* ' which provides a comprehensive description of film roughness characterizing the growth process. To identify the growth governing surface related phenomenological events among plastic flow, evaporation-recondensation, bulk and surface diffusion, experimental $g(q)$ was fitted with that proposed theoretically by Tong et. al. In case of Al-thin films, fundamental mechanisms leading to growth of surface morphologies were found to be different for different deposition times. Upon reactive assistance of N^+/N_2^+ ions during the growth, kinetics of adatoms was found to be systematic.

Chapter 4: Growth Optimizations of AlN Thin Films by Reactive Assistive IBSD

This chapter presents compositional and structural studies on ion beam sputtered AlN thin films on Si(100) substrate. The experiments were aimed to optimize growth conditions as a function of different deposition parameters like, assisted ion energy, substrate temperature and deposition time. Having made a preliminary choice upon assisted ion energy and substrate temperature to initiate the growth optimizations, a systematic study was undertaken by varying the substrate temperature from room temperature (RT) to 500°C in the steps of 100°C. An

extensive HR-TEM investigation was carried out on microstructural variations, AlN phase formation and evolution of average crystallite size as a function of temperature. In order to obtain the highest fraction of AlN on film surface, XPS was employed to unravel the compositional variations of film surface at RT, 100°C and 500°C. The binding energies of Al-2p, N-1s and O-1s core electrons indicated formation of 2H polytypoid of AlN. The increase in concentration of AlN on film surface was elucidated through detailed analysis with calculated elemental atomic concentrations. After optimization of deposition parameters, growth of textured AlN thin films with preferred orientation could be achieved by introducing a Ti-under layer. An investigation on texture analysis of AlN/Ti/Si(100) heterostructure is presented. Different diffraction geometries, namely, symmetric ω -2 Θ scan, rocking curves (ω -scan) and pole figure measurements were used to confirm the pseudomorphic heteroepitaxial growth of AlN thin film. Positron annihilation and PL spectroscopies were used to investigate the presence of defects in film microstructure.

Chapter 5: Spectrophotometry of Reactive Assistive IBSD Grown AlN Thin Films

This chapter investigates the optical band-gap (E_g) and associated energy tails of reactive assistive IBSD grown AlN thin films on Si(100). The absorption spectra presented in this chapter were collected in reflectance mode. Variation of absorption coefficient (α) with photon energy ($h\nu$) is presented as a function of substrate temperature. Important features of α vs. $h\nu$ are described by classifying it into three categories. Tauc's plots were obtained to determine E_g of

nanocrystalline AlN thin films in the region of α vs. $h\nu$ where α is governed by the optical transitions from one extended state to another extended state. Occurrence of Urbach energy tails (E_U) is discussed on the basis of disorder in film microstructure causing density of electronic states tailing into the band gap. A methodology is presented to determine E_U in the classified range of α . Also weak absorption tails could be estimated for small optical absorptions (α) governed by the optical transitions from one tail state to another tail state arising from defect induced disorder. In addition, an analytical approach is presented to determine the refractive index (n) and extinction coefficient (k) of AlN thin films grown on Si(100) at different substrate temperatures.

Chapter 6: Piezoelectric Properties of Reactive Assistive IBSD Grown AlN Thin Films

This chapter presents measurement of piezoelectric properties of AlN thin films using three different techniques. Different variants of Ti/AlN/Ti/Si(100) hetrostructure were fabricated by varying thickness of AlN thin film. PFM was employed to determine $d_{(33eff)}$ and an analytical procedure is presented to use phase and amplitude data to generate piezo response loops. In addition, height, phase and amplitude images were analysed to extract the polarity of AlN thin films. XRD technique was used to determine $d_{(33eff)}$ by connecting the top and bottom electrodes of thin film capacitor Ti/AlN/Ti/Si(100) to the output of a DC power supply. For this, textured growth of AlN thin film was confirmed along the preferred direction of growth by performing symmetric ω -2 Θ scan. Piezo electric strains were calculated from the FWHM of corresponding rocking curves at each

applied DC voltage. In addition, a methodology is outlined to calculate the $d_{(33eff)}$ from C-V measurements using an LCR meter. These reactive assistive IBSD grown AlN thin films were found to possess high $d_{(33eff)}$ as compared to those reported in literature. Genesis of their enhanced piezoelectric response is discussed by proposing suitable phenomenological models.

Chapter 7: Summary and Future Scope

This chapter summarizes important experimental findings on IBSD grown piezoelectric AlN thin films, implications on technology and recommendations for future works.

LIST OF FIGURES

<u>Figure 1.1</u>	Unit cell of PZT containing one molecular formula unit. Pb at cube corners, oxygen at face centers and Zr or Ti atom at the body center [7].	6
<u>Figure 1.2</u>	Variation of longitudinal piezoelectric coefficient (d_{33}) of PZT thin film as a function of its composition [8].	7
<u>Figure 1.3</u>	Tetrahedral coordination of Zn and O in ZnO crystal structure. The c-axis is in vertical direction in this figure.	8
<u>Figure 1.4</u>	Piezoelectric response (d_{33}) of ZnO thin films of various thicknesses [13].	9
<u>Figure 1.5</u>	(A) Arrangement of Al^{3+} and N^{3-} ions eventually bonded into tetrahedral coordination in wurzite hexagonal crystal. (B) Al^{3+} and N^{3-} ions are arranged along c-axis of the unit cell.	11
<u>Figure 1.6</u>	Deformation of tetrahedron on the application of compressive and tensile stresses.	12
<u>Figure 2.1</u>	Incident ions on the target surface and ejection of sputtered particles.	27
<u>Figure 2.2</u>	Experimental set-up of ion beam sputter deposition (IBSD) system.	30
<u>Figure 2.3</u>	Internal arrangement of RF ion source with three grid Accelerator system.	31
<u>Figure 2.4</u>	Schematic representation of End-hall ion source.	32
<u>Figure 2.5</u>	Schematic diagram of basic components of RF Neutralizer (RFN).	33
<u>Figure 2.6</u>	Scanning of surface morphology using atomic force microscopy (AFM).	36
<u>Figure 2.7</u>	2D and 3D surface morphology of AlN thin films deposited on Si(100) substrate for 15 minutes using reactive assistive IBSD.	37

<u>Figure 2.8</u>	Schematic diagram of scanning electron microscope (SEM).	38
<u>Figure 2.9</u>	SEM images of AlN thin films at different substrate temperatures.	38
<u>Figure 2.10</u>	Schematic diagrams of X-rays by a crystal (Brag condition).	39
<u>Figure 2.11</u>	Schematic of four axis of diffractometer showing different showing different angles between incident X-ray beams and sample surface.	41
<u>Figure 2.11.1</u>	Asymmetric-reflection scan or GIXRD geometry for measurements on thin film samples.	42
<u>Figure 2.11.2</u>	Symmetric-reflection scan geometry.	42
<u>Figure 2.11.3</u>	Rocking curve geometry on a textured thin film sample.	43
<u>Figure 2.12</u>	XRD analysis of AlN thin films grown on Si (100) substrate at 500°C temperature in different geometries, (A) GIXRD, (B) Symmetric ($\Theta/2\Theta$ scan) and inset shows corresponding rocking curve (ω -scan).	44
<u>Figure 2.13</u>	Schematic diagram of a conventional transmission electron microscope showing different lenses and trajectories.	45
<u>Figure 2.14</u>	Dark field image and corresponding selected area electron diffraction (SAED) pattern of AlN thin films deposited on Si(100) substrate at 400°C.	46
<u>Figure 2.15</u>	Schematic diagram of X-ray photoelectron spectroscopy (XPS).	47
<u>Figure 2.16</u>	Survey spectrum of AlN thin film grown on Si(100) substrate at 500°C temperature.	48
<u>Figure 2.17</u>	Schematic diagram of a photoluminescence (PL) spectrometer.	50
<u>Figure 2.18</u>	Basic block diagram of a spectrophotometer showing constituent components.	52
<u>Figure 3.1</u>	Schematic representation of three modes of thin film growth. Here Θ is the overlayer coverage in monolayer (ML).	56
<u>Figure 3.2</u>	Representative 3D AFM images ($1 \times 1 \mu\text{m}^2$) of the evolution of surface morphology for the films grown for different deposition time as, (A) 3 minutes, (B) 5 minutes, (C) 8 minutes and (D) 15 minutes.	65

<u>Figure 3.3</u>	Representative line profiles across the sample surface for different deposition time: (A) 3 minutes, (B) 5 minutes, (C) 8 minutes, (D) 15 minutes.	66
<u>Figure 3.4</u>	Plot of the interface width of the substrate surface as a function of length scale for several different deposition time varied as (A) 3 minutes (B) 5 minutes (C) 8 minutes and (D) 15 minutes.	67
<u>Figure 3.5</u>	Comparison of α -exponents obtained from two different techniques for different deposition times.	68
<u>Figure 3.6</u>	Dynamic scaling constant ' β ' governing the growth for different deposition times with different slopes.	69
<u>Figure 3.7</u>	Autocovariance function for different deposition times depicting how heights are co-related at different points across lateral direction.	70
<u>Figure 3.8</u>	Spectral power density and critical lengths obtained corresponding to different deposition time.	71
<u>Figure 3.9</u>	Fitting of experimentally obtained $g(q)$ with equation (7) for different deposition times indicating towards dominating roughening/smoothening phenomena. The data are presented as log-log plots where (A) 3 minutes, (B) 5 minutes, (C) 8 minutes and (D) 15 minutes.	73
<u>Figure 3.10</u>	Representative 3D atomic force microscope images ($1 \times 1 \mu\text{m}^2$) along with line profiles across the sample Surface displaying the evolution of surface morphology for the films grown for different deposition time as, (A) 3 minutes, (B) 5 minutes, (C) 8 minutes and (D) 15 minutes.	76
<u>Figure 3.11</u>	Log-Log plots of interface width (ξ) vs. length scale (L) for different growth time varied as (A) 3 minutes (B) 5 minutes (C) 8 minutes and (D) 15 minutes.	78
<u>Figure 3.12</u>	Variation of static scaling exponent ' α ' with deposition time. Dynamic scaling exponent ' β ' is extracted from the slope of $\text{Log}(\delta)$ vs. $\text{Log}(t)$ curve shown in the inset.	80
<u>Figure 3.13</u>	Autocovariance function for different deposition times depicting how heights are co-related at different points	

	across lateral direction.	81
<u>Figure 3.14</u>	Power spectral density $g(q)$ obtained for thin films deposited for different deposition time.	81
<u>Figure 3.15</u>	Fitting of experimentally obtained power spectral density $g(q)$ with equation (7) for different deposition time, (A) 3 minutes, (B) 5 minutes, (C) 8 minutes and (D) 15 minutes.	83
<u>Figure 4.1</u>	Plots of X-ray diffraction (XRD) measurements on AlN thin films deposited by reactive assistive IBSD at different assisted ion energy.	90
<u>Figure 4.2</u>	Grazing incidence X-ray diffraction (GIXRD) measurements on AlN thin films deposited at different substrate tmperatures. The films were found to be amorphous in nature.	91
<u>Figure 4.3</u>	Surface morphology of AlN thin films deposited at different substrate temperatures acquired by atomic force microscopy (AFM). Some distinct morphological features are appeared at 500°C which are marked as dotted circles.	92
<u>Figure 4.4</u>	Morphology of the AlN thin films as seen by scanning electron microscope (SEM) when deposited at different substrate temperatures.	93
<u>Figure 4.5(A)</u>	Dark field images acquired by TEM at each substrate temperature revealing structural transformations from room temperature (RT) to 500°C of AlN thin films. Selected area electron diffraction (SAED) patterns of the films prepared from RT to 200°C are shown in their in-set. While films deposited at 300°C to 500°C, crystalline region of interest are highlighted with bright rings.	94
<u>Figure 4.5(B)</u>	Selected area electron diffraction (SAED) patterns along with average crystallite size (d) distribution for the samples prepared at 300°C to 500°C substrate temperature.	96
<u>Figure 4.6</u>	1000 eV wide survey scans of AlN thin films deposited at (A) RT, (B) 100°C and (C) 500°C substrate temperatures.	99

<u>Figure 4.7</u>	A series of plots deconvoluted into constituent subpeaks of, (A) Al-2p peak, (B) N-1s peak, (C) O-1s. These plots progress from top to bottom in cumulative substrate temperature as (a) RT, (b) 100°C and (c) 500°C.	100
<u>Figure 4.8</u>	X-ray photoelectron spectroscopy (XPS) of AlN thin films, deposited at 500°C, at a depth of 50 nm from the surface; (A) Survey scan; (B) Al-2p core level spectrum; (C) N-1s core level spectrum and (D) O-1s core level spectrum.	109
<u>Figure 4.9</u>	Compositional variation of AlN along with Al ₂ O ₃ domains and Al-O interaction at the grain boundaries with substrate temperature. A distinct increase in AlN phase fraction is observed at 500°C substrate temperature.	111
<u>Figure 4.10</u>	Variation of S-parameter (S) with positron beam energy (E _p) for different substrate temperatures. For reference, S vs E _p curve of Si(100) substrate is also plotted.	112
<u>Figure 4.11</u>	VEPFIT deduced S _{AlN} vs. substrate temperature.	113
<u>Figure 4.12</u>	Growth of AlN thin films for different deposition time. Formation of wurtzite hexagonal (WH) phase of AlN takes place for 45 minutes of deposition.	115
<u>Figure 5.1</u>	Reflection from a surface; (A) specular reflection, (B) Diffuse reflection.	122
<u>Figure 5.2</u>	Absorption coefficient (α) as a function of photon energy ($h\nu$), (A) at RT, (B) 100°C to 500°C substrate temperatures. These plots are classified into three regions. In each region, α depends upon $h\nu$ differently.	126
<u>Figure 5.3</u>	Tauc's plots to estimate the optical band gap energy at each substrate temperature. at RT, E_g is found to be 5.08 eV. As the temperature of the substrate is increased to 100°C, E_g increases subsequently to 5.13 eV. Maintaining this rising trend with further increase in substrate temperature E_g becomes 5.19 eV, 5.20 eV and 5.21 eV, respectively, for	

	300°C, 400°C and 500°C.	128
<u>Figure 5.4</u>	Comparative variation of E_g with net $E_u + E_t$. When fitted with a straight line, intercept of the linear fit (~ 6.24 eV) represents the optical band gap energy of the films when there is no disorder in their microstructure.	133
<u>Figure 5.5</u>	Reflection and transmission events of light traveling through a medium of refractive index n_1 deposited on the substrate of refractive index n_2 in a surrounding medium of refractive index n_o .	134
<u>Figure 5.6</u>	Variation of average refractive index (n_a) and extinction coefficient (k_a) of AlN thin films on Si(100) substrate with temperature.	136
<u>Figure 6.1</u>	(A) Direct piezoelectric field, (B) Converse piezoelectric field.	142
<u>Figure 6.2</u>	Molecular model of piezoelectricity, (A) center of gravity of all negative and positive charges of each molecule coincides, (B) generation of little dipoles due to separation of gravity centers of negative and positive charges, (C) generation of linked charges and hence the polarization on the surface.	143
<u>Figure 6.3</u>	Input and output scheme of direct piezoelectric effect.	144
<u>Figure 6.4</u>	Input and output scheme of converse piezoelectric effect.	145
<u>Figure 6.5</u>	Right-handed Cartesian co-ordinate system used in tensor representation of piezoelectric coefficients.	146
<u>Figure 6.6</u>	Schematic representation of longitudinal piezoelectric coefficient d_{33} .	148
<u>Figure 6.7</u>	Schematic representation of transverse piezoelectric coefficient d_{31} .	149
<u>Figure 6.8</u>	Schematic representation of shear piezoelectric coefficient d_{15} .	149
<u>Figure 6.9</u>	Layer geometry of AlN/Ti/Si(100) hetrostructures. Inset shows the photographs of specimens S-60 and S-75.	153
<u>Figure 6.10</u>	Layer geometry of Ti/AlN/Ti/Si(100) hetrostructures with circular top electrodes. Inset shows the photographs	

	of specimens S1-60 and S1-75.	153
<u>Figure 6.11</u>	Layer geometry of Ti/AlN/Ti/Si(100) hetrostructures with square top electrode. Inset shows the photographs of specimens S2-60.	154
<u>Figure 6.12</u>	High resolution X-ray diffraction (HR-XRD) analyses of (A) S-60, and (B) S-75. Inset shows the rocking curve for each respective specimen.	155
<u>Figure 6.13</u>	Schematic view of piezo force microscopy (PFM) measurement system.	156
<u>Figure 6.14</u>	Piezo force microscopy (PFM) of sample S-60, (A) Height scan, (B1), piezo response phase image, (C1), piezo response amplitude image, (B2) electrical hysteresis, (C2) mechanical hysteresis (butterfly loop), (D) piezo response loop.	157
<u>Figure 6.15</u>	Piezo force microscopy (PFM) results of S-75, (A) Height scan, (B1), piezo response phase image, (C1), piezoresponse amplitude image, (B2) electrical hysteresis, (C2) mechanical hysteresis (butterfly loop), (D) piezoresponse loop.	158
<u>Figure 6.16</u>	Experimental set-up for the measurement of Longitudinal piezoelectric coefficient ' d_{33} ' using X-ray diffraction (XRD) on the samples with circular and square top electrodes.	160
<u>Figure 6.17</u>	Change in the position and full width at half maxima (FWHM) peaks in the rocking curves for the (100) reflection from a crystalline wurtzite hexagonal AlN thin films under the voltage ranging between 0-5V applied between the electrodes.	162
<u>Figure 6.18</u>	Variation of longitudinal piezoelectric coefficient $d_{33(eff)}$ of AlN thin films obtained for 60 minutes (S1-60) and 75 minutes (S1-75). Insets show the change in strain as a function of applied electric field corresponding to S1-60 and S1-75.	162
<u>Figure 6.19</u>	Piezoelectric response of AlN thin films sandwiched	

	between two titanium electrodes. (A) no voltage between the electrodes, (B) when voltage is applied between the electrodes.	163
<u>Figure 6.20</u>	Capacitance-voltage (C-V) curves of AlN thin films grown for 60 minutes (S1-60) and 75 minutes (S1-75).	164
<u>Figure 6.21</u>	Longitudinal piezoelectric coefficient $d_{(33eff)}$ of AlN thin films grown for 60 and 75 minutes (S1-60 and S1-75). For S1-75, a negative strain axis indicated that the direction of applied electric field and resulting strain in thickness are in opposite directions.	165
<u>Figure 6.22</u>	Photoluminescence (PL) measurements of S1-60 and S1-75 confirming the presence of V_{Al}^- and V_N^+ .	166
<u>Figure 6.23</u>	Model for charged vacancy induced enhancement in lattice polarization, (A) a-axis oriented AlN/Ti/Si(100) hetrostructure, (B) V_{Al}^- and V_N^+ as spherical cavities in a dielectric, (C) Formation of defect dipoles by the presence of two spherical cavities of opposite surface charge at the nearest possible distance.	168

LIST OF TABLES

<u>Table 1.1</u>	Properties of wurtzite hexagonal AlN.	12
<u>Table 1.2</u>	Values for c-axis oriented AlN thin films reported in literature.	13
<u>Table 2.1</u>	Characterization tools used to investigate different properties of reactive assistive IBSD grown AlN thin films.	35
<u>Table 3.1</u>	Comparison of α , L_c and δ for different deposition times.	68
<u>Table 3.2</u>	Comparison of fits of equation (7) for different deposition times.	72
<u>Table 3.3</u>	Comparison of static scaling exponent (α), critical length (LC) and rms roughness (δ) of AlN-thin films.	79
<u>Table 3.4</u>	Comparison of fitting parameters obtained by fitting power spectral density $g(q)$ with equation (4) for different deposition times.	82
<u>Table 4.1</u>	Microstructural details of the films extracted from TEM and AFM.	96
<u>Table 4.2</u>	Variation of binding energy of each subpeak with substrate temperature.	104
<u>Table 4.3</u>	Atomic concentration at different substrate temperatures.	108
<u>Table 4.4</u>	Optimized deposition parameters for cubic and hexagonal AlN thin films using reactive assistive IBSD.	117
<u>Table 5.1</u>	Comparison of optical band gap energy (E_g), Urbach energy (E_u) and WAT energy (E_t) at different substrate temperatures.	130

Chapter 1

Piezoelectric Thin Films: An Overview

This chapter briefly summarizes the technological need of piezoelectric thin films for energy harvesting. Basic introduction to piezoelectricity along with historical perspective is provided. The crystal structure, origin of piezoelectricity and values of longitudinal piezoelectric coefficient (d_{33}) for commonly used piezoelectric materials like lead zirconate titanate (PZT), zinc oxide (ZnO) are described. Piezoelectric AlN thin film is discussed with respect to its crystal structure and genesis of piezoelectricity. A concise discussion on deposition techniques used to grow AlN thin films is presented to emphasize upon ion beam sputter deposition (IBSD) in reactive assistive mode as one of the promising technique to grow device grade AlN thin films. At the end, possible contribution of piezoelectric AlN thin films towards energy harvesting is touched upon.

1.1 Need of Piezoelectric Thin Films

In recent past, piezoelectric materials have attracted the attention of scientific as well as industrial community due to their great potential for micro-and nanoscale devices. They offer efficient electromechanical transduction with added advantage of easy micromachining using standard processing tools. Piezoelectric micro-electro-mechanical-system (MEMS) has been proven to be an attractive technology for energy harvesting in the form of sensors and actuators. Major challenges have emerged as MEMS move to smaller size and increased integration density while requiring fast response and large motions. Continued scaling to nano-electro-mechanical-systems (NEMS) requires revolutionary advances in sensors, actuators and transducers. These advances are enabled by the

rapidly growing field of piezoelectric thin films [1]. MEMS and NEMS, utilizing piezoelectric thin films, provide the required large linear forces with fast actuation at small drive voltages. This, in turn, provides accurate displacements at high integration densities, reduces the voltage burden on the integrated control electronics and decreases MEMS/NEMS complexity. With these advantages, the field of piezoelectric thin films has burgeoned over the past decade and requires significant progress on the development of new piezoelectric materials and way to enhance the piezoelectric response of existing piezoelectric thin film materials.

1.2 Piezoelectricity

The word piezoelectricity means electricity resulting from pressure. It is derived from the Greek word *piezo* or *piezein* which means to squeeze or press, and *electric* or *electron*, which means amber, an ancient source of electric charge. Thus ***piezoelectricity*** is the electric charge that accumulates in certain solid materials in response to applied mechanical stress. Piezoelectricity was discovered in 1880 by French physicists Jacques and Pierre Curie.

The piezoelectric effect is understood as the linear electromechanical interaction between the mechanical and the electrical states in crystalline solids that are devoid of inversion symmetry. It is further classified into two types of processes:

- I. Direct Piezoelectric Effect:** The internal generation of electrical charge resulting from an applied mechanical force.
- II. Converse Piezoelectric Effect:** The internal generation of a mechanical strain resulting from an applied electrical field.

Piezoelectricity is a reversible process i.e. materials exhibiting direct piezoelectric effect also exhibit converse piezoelectric effect. Piezoelectricity and its mathematical description is discussed in more details in Chapter 6.

1.3 Brief History of Piezoelectricity

The first experimental demonstration of linear interaction between mechanical and electrical behaviour of crystalline materials was reported by French physicists Jacques and Pierre Curie in 1880. Their experiment consisted of a conclusive measurement of surface charges appearing on special class of crystals which were subjected to mechanical stress [2]. In order to distinguish it from other areas of physical phenomena such as ‘contact electricity’ (friction generated static electricity) and ‘pyroelectricity’ (electricity generated from crystals by heating), it was quickly named as ‘*piezoelectricity*’ in the scientific community of those days. However, the Curie brothers did not predict that crystals exhibiting direct piezoelectric effect (electricity from applied stress) would also exhibit converse piezoelectric effect (stress in response to applied electric field). This property was mathematically deduced from fundamental thermodynamic principles by Lippmann in 1881. Curies immediately confirmed the existence of the ‘converse effect’, and continued on to obtain quantitative proof of the complete reversibility of electro-elasto-mechanical deformations in piezoelectric crystals.

In 1882, after only two years of interactive work within the European scientific community, the core of piezoelectric applications science was established by following revelations:

- Identification of piezoelectric crystals on the basis of asymmetric crystal structure
- Reversible exchange of electrical and mechanical energy
- Usefulness of thermodynamics in quantifying complex relationships among mechanical, thermal and electrical variables.

In the following 25 years (leading up to 1910), much more work was done to make this core grow into a versatile and complete framework which defined completely, the 20 natural crystal classes in which piezoelectric effects occur, and defined all 18 possible macroscopic piezoelectric coefficients accompanying a rigorous thermodynamic treatment of crystalline solids using appropriate tensor formalism. The first serious application work on piezoelectric devices took place during World War I. In 1917, P. Langevin and French coworkers began to develop an ultrasonic submarine detector. Since then the continuing development of sonar transducers, circuits, systems, and materials has never ceased in scientific as well as industrial community.

In the period of 1940-1965, advances in materials science in the field of piezoelectricity fall into three categories:

- Development of the barium titanate (BaTiO_3) and lead zirconate titanate (ZrTiO_3) family of piezoceramics.
- The development of an understanding of the correspondence of perovskite crystal structure to electromechanical activity.
- The development of a rationale for doping both of these families with metallic impurities achieving desired properties such as dielectric

constant, stiffness, piezoelectric coupling coefficients and ease of poling etc.

All of these advances contributed to establishing an entirely new method of piezoelectric device development [2].

Presently, the commercial success of piezoelectric thin films has attracted the attention of industries worldwide and spurred a new effort to develop successful piezoceramic thin film products as can be understood from the increased rate of article publication in the field of piezoelectric thin film materials and their applications.

1.4 Common Piezoelectric Thin Film Materials

1.4.1 Lead Zirconate Titanate (PZT)

Lead zirconate titanate (PZT) is a ferroelectric ceramic that is widely used in most of the transducers and actuators. It is one of the best-known piezoelectric materials with excellent piezoelectric and mechanical properties which can be used in polycrystalline form also [5]. The chemical formula of lead zirconate titanate is PbZr(Ti)O_3 . It is a solid solution of two oxides: lead zirconate (PbZrO_3), which is antiferroelectric and lead titanate (PbTiO_3), which is ferroelectric. The crystal structure of PZT is perovskite and its unit cell is shown in Figure 1.1. The unit cell contains one formula molecular unit with the lead atoms at the corners (1 atom), oxygen atoms at the face centers (3 atoms), and Zr or Ti atoms at the body centre. The zirconium and titanium atoms are octahedrally coordinated to the oxygen atoms. The Curie temperature (T_C) of PZT is about

350°C. Above T_C , the structure is cubic, and the material is in the paraelectric phase [6].

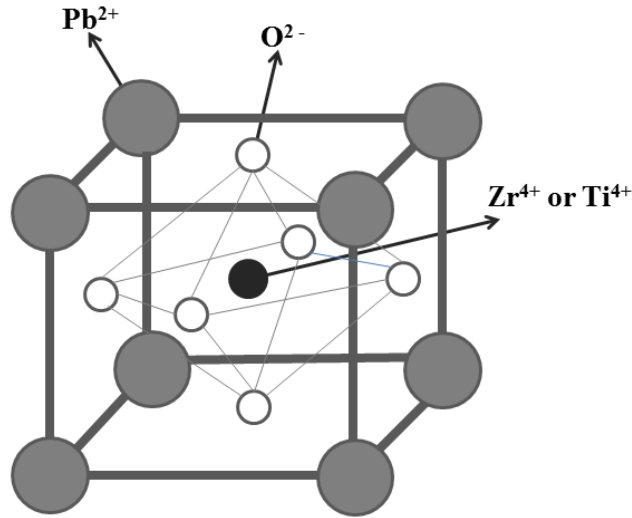


Figure 1.1 Unit cell of PZT containing one molecular formula unit. Pb at cube corners, oxygen at face centers and Zr or Ti atom at the body center [7].

The crystal structure below T_C depends on the composition of the solid solution. Below T_C , the solid solution is useful as a practical piezoelectric ceramic only over a small composition of about 48% of PbTiO₃ and 52% of PbZrO₃. Figure 1.2 depicts the longitudinal piezoelectric coefficient (d_{33}) of PZT as a function of its composition. It can easily be observed that d_{33} coefficient shows a peak at the composition of 48% PbTiO₃ and 52% PbZrO₃ and provides an idea about the piezoelectric sensitivity of PZT in terms of d_{33} [7, 8].

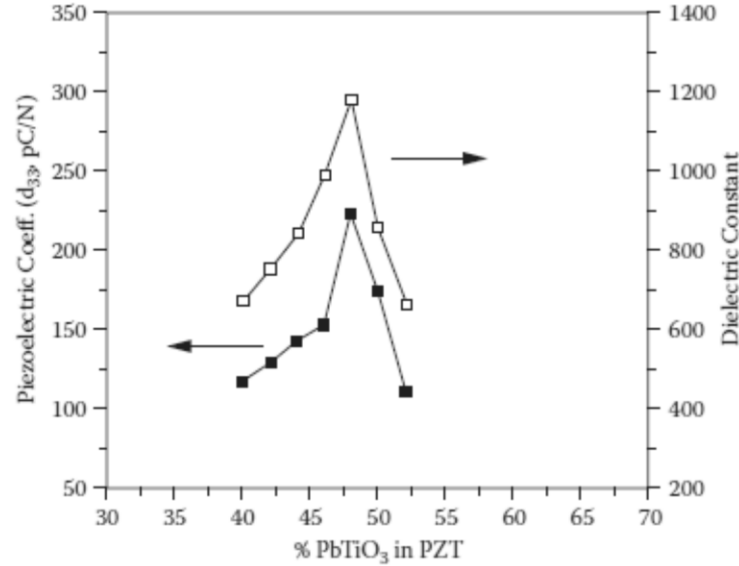


Figure 1.2 Variation of longitudinal piezoelectric coefficient (d_{33}) of PZT thin film as a function of its composition [8].

Incorporation of PZT into MEMS and NEMS pushes it into the field of thin films where its behaviour can be very different from its bulk properties. Significant progress has been made in the last decade over the development of several deposition techniques for the growth of PZT thin films. Among them, pulsed laser deposition (PLD), RF sputtering and plasma enhanced chemical vapor deposition (PECVD) techniques are most commonly used [9, 10]. But one critical disadvantage of PZT is that it contains more than 60 percent lead (Pb) by weight. This large Pb-content creates hazards during processing (Pb volatilizes and is released into the atmosphere) and is potentially toxic during disposal into the environment which limits its applications (e.g., *in vitro*). Over the past few years, regulatory agencies world-wide emphasized upon the restricted use of lead, with the exception of the electronics industry due to the lack of a suitable replacement to PZT [11]. Also, its T_C is very low which restricts the limit of safe

operation for PZT based piezoelectric devices. Thus suitable lead-free piezoelectric materials with improved T_C and piezoelectric properties comparable to PZT are still being developed and motivate the present research work.

1.4.2 Zinc Oxide (ZnO)

Zinc Oxide (ZnO) crystals in the form of thin films or other nanostructural forms such as nanowires and nanotubes have been studied extensively for their piezoelectric response. The crystal structure of ZnO is hexagonal wurtzite with 6mm symmetry. Due to this symmetry, a single crystal of ZnO has a unique polar direction (c -axis). ZnO thin films with high c -axis orientation exhibit good piezoelectric properties [12]. It can be seen in figure 1.3, that the fundamental building block of the crystal is a puckered hexagonal ring in which both Zn and O have tetrahedral coordination.

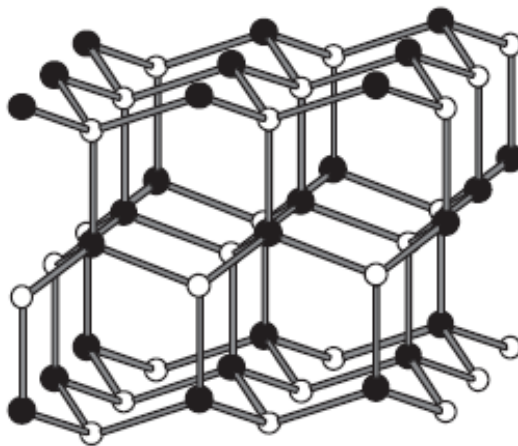


Figure 1.3 Tetrahedral coordination of Zn and O in ZnO crystal structure. The c -axis is in vertical direction in this figure.

To have a gross idea about the piezoelectric response of ZnO thin films as a function of their thickness, its d_{33} is shown in figure 1.4 as reported by Ke-ming Zhang et al. [13].

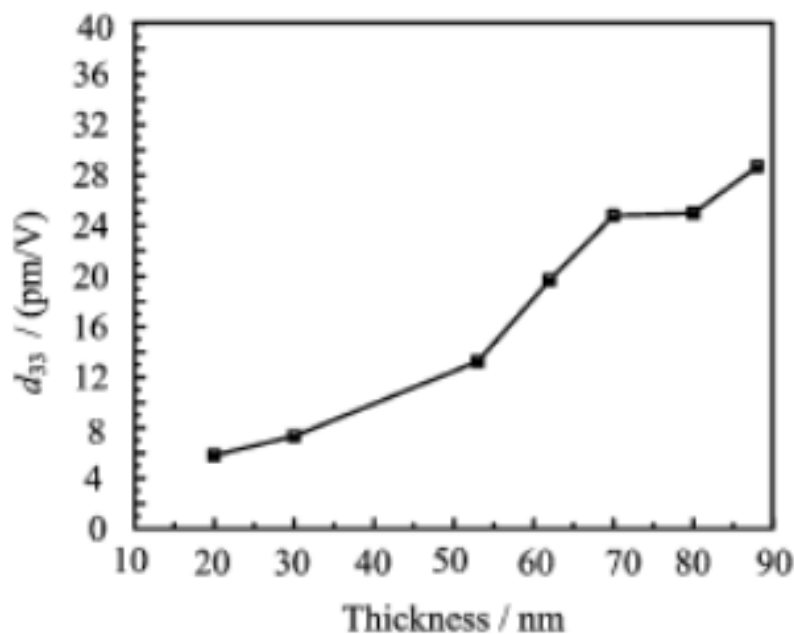


Figure 1.4 Piezoelectric response (d_{33}) of ZnO thin films of various thicknesses [13].

But ZnO also poses serious difficulties when processed in to the thin film form. It is difficult to process and integrate into thin film configuration on silicon as a substrate. Also, it is very reactive to other integrated circuit (IC) materials which make it very hard to integrate with standard complementary metal oxide semiconductor (CMOS) processes [14].

1.5 Piezoelectric Aluminum Nitride (AlN)

Aluminum Nitride (AlN) is a III-group nitride that exhibits synergistic combination of physical, chemical and mechanical properties. These property attributes have made this material indispensable in several technical applications pertaining to thin film devices and sensors [12, 15]. Hence, the study on surface microstructure of AlN thin films is of great interest from both academic and technological point of view. AlN is an ionic/covalent compound in which Al^+ and N^- ions are bonded together by covalent bonds having sp^3 hybridization and

crystallize into two polytypes. One is wurtzite hexagonal structure with the space group C_{6v}^4 ($P6_3mc$). Another is the zinc-blende structure with T_d^2 ($F\bar{4}3m$) symmetry. The ground-state properties are obtained by minimizing the total energy with respect to the cell volume. In zinc-blende structure, the volume is directly related to the cubic lattice constant ' a_0 ', while in wurtzite structure, the volume is governed by the two hexagonal lattice constants ' a ' and ' c ' [12]. Only wurtzite hexagonal AlN will be discussed as it possesses higher utility for piezoelectric applications. Figure 1.5(A) shows the basic wurtzite hexagonal crystal structure. The bond stacking of AB type is shown in hexagonal [0001] direction. According to the number of bilayers needed to guarantee the translational symmetry in [0001] direction, the wurtzite hexagonal polytype is labeled with 2H. When viewed altogether, the atomic positions are the same as in a hexagonal crystal structure but locally each atom has a tetrahedral coordination [16].

At the same time, III-group nitrides are unique among the III-V semiconductors because nitrogen is the smallest and most electronegative of the group-V elements. The metal-nitrogen covalent bond has a greater degree of ionicity than other III-V covalent bonds. Since the wurtzite III-Ns do not have inversion symmetry along the c-axis, the strong ionicity of the metal-nitrogen bond results in a large macroscopic polarization along [0001] crystal direction [17-19]. Since this polarization effect occurs in the equilibrium lattice of the III-N at zero strain, it is termed spontaneous polarization (P_s). The degree of non-

ideality of the crystal lattice governs the strength of the spontaneous polarization.

Important parameters of wurtzite hexagonal AlN are listed in table 1.1 [16].

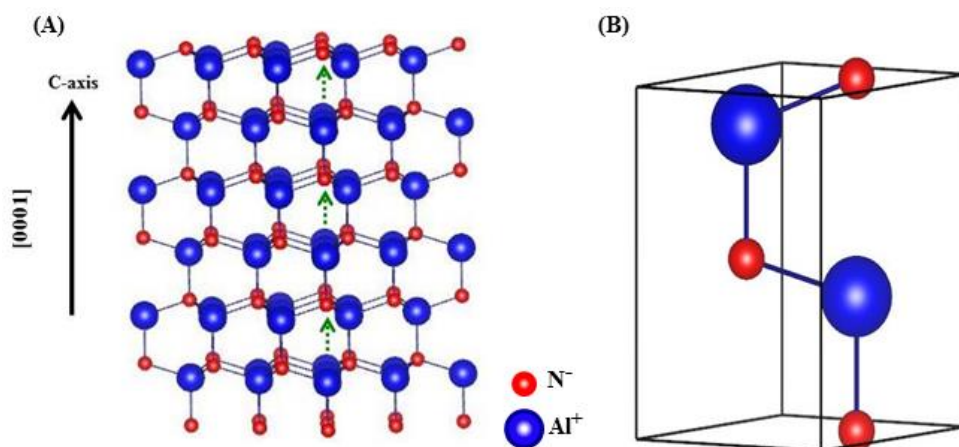


Figure 1.5 (A) Arrangement of Al⁺ and N⁻ ions eventually bonded into tetrahedral coordination in wurzite hexagonal crystal. (B) Al⁺ and N⁻ ions are arranged along c-axis of the unit cell.

Here it is worth noticing that in last few decades, AlN has been a subject of extensive research due to its piezoelectric properties. Being a partially ionic III-group nitride it exhibits encouraging piezoelectric effects. Piezoelectric polarization is induced for internal displacements of the group-III ion relative to the N⁻ ion in an elementary cell. However, even under the equilibrium conditions, the lower-symmetry wurtzite polytypes possess an intrinsic spontaneous polarization field along the c-axis (Figure 1.5(B)).

Figure 1.6 illustrates the mechanism of piezoelectricity in AlN. In AlN, the puckered rings are superimposed on each other, stacked parallel to the c-axis. The result is a structure in which all of the AlN₄ tetrahedral units have the same orientation. Figure 1.6 shows that all of the Al⁺ ions have one N⁻ neighbor directly above it along the c-axis, and three N⁻ neighbors below it. When AlN is

compressed along the c-axis, the material deforms by changing the $\text{N}^- - \text{Al}^+ - \text{N}^-$ bond angle, since this angle is more readily compressed than the AlN bond. As the tetrahedron deforms, the center of positive and negative charges of the unit cell are displaced, producing the polarization that is the hallmark of piezoelectricity [12].

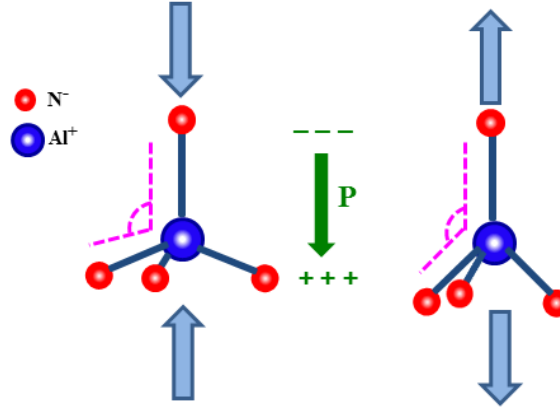


Figure 1.6 Deformation of tetrahedron on the application of compressive and tensile stresses.

Herein, it is worth noticing that in bulk AlN, it is assumed that rearrangement of surface charges nullifies the spatially uniform spontaneous polarization. The effect of spontaneous polarization fields can therefore only be observed in layered structures such as wurtzite AlN thin films and its heterostructure variants [20].

Table 1.1 Properties of wurtzite hexagonal AlN.

Wurtzite Polytype		
Lattice Constants	$a = 3.112 \text{ \AA}$	$c = 4.982 \text{ \AA}$
Thermal expansion	$\frac{\Delta a}{a} = 4.2 \times 10^{-6}/\text{K}$	$\frac{\Delta c}{c} = 5.3 \times 10^{-6}/\text{K}$
Thermal Conductivity	$K = 2 \text{ W/cmK}$	
Index of Refraction	$n(3 \text{ eV}) = 2.15 \pm 0.05$	
Dielectric Constant	$\epsilon_0 = 8.5 \pm 0.2$	$\epsilon_\infty = 4.68 - 4.84$

A number of research articles have discussed the piezoelectric response of c-axis oriented AlN thin films on silicon substrate [21, 22]. Table 1.2 presents a collection of effective $d_{33(\text{eff})}$ values reviewed and reported by Hyunchang Shin et al. [23] for c-axis oriented AlN thin films on different substrates.

Table 1.2 Values for c-axis oriented AlN thin films reported in literature.

Sr. No.	Measurement Method	$d_{33(\text{eff})}$ (pm/V)	Literature
1	Mach-Zehnder interferometer	5.1	Lueng et al.[12]
2	Single beam laser interferometer with top electrode layer	5.6	Guy et al.[13]
3	Single beam laser interferometer with top electrode layer	4.17	Chen et al.[14]
4	PFM with top electrode layer	4.9	Mortet et al.[8]
5	PFM with top electrode layer	6.94	Tonisch et al.[9]

Furthermore, any change in microstructural attributes of the film can eventually alter its piezoelectric response. There are several deposition techniques by which AlN thin films have been grown on various substrates such as RF and DC reactive magnetron sputtering [24, 25], pulsed-DC reactive sputtering [26], molecular beam epitaxy (MBE) [27], reactive ion beam assisted sputter deposition (IBAD) [28, 29]. As the growth of a-axis oriented AlN thin films on silicon substrate is difficult, information on the piezoelectric response of epitaxial AlN thin films with a-axis orientation is rather sparse. Only few studies exist in the literature reporting the $d_{33(\text{eff})}$ of a-axis oriented epitaxial AlN thin films [30, 31].

In this context, unique features of reactive assistive IBSD provide more degrees of freedom to manipulate the direction of preferred orientation in epitaxial AlN thin films. In reactive assistive IBSD, two separate ion sources are employed. The main ion source provides inert ions (generally Ar^+) to sputter the aluminum target and the assisted ion source provides reactive flux of nitrogen ions (N^+/N_2^+) to form AlN at the surface of the substrate. Ion beam sputter deposition (IBSD) has several additional advantages over other sputtering techniques, like independent control over incident ion beam energy and incident ion current [32, 33]. IBSD is described in more details from a fundamental point of view in Chapter 2.

The above mentioned facts together provide the impetus to the present research work with two principle motives.

- I. Growth of epitaxial AlN thin films on Si (100) substrate with preferred orientation along a-axis using reactive assistive ion beam sputter deposition (IBSD).
- II. Measurement of piezoelectric response of reactive assistive IBSD grown a-axis oriented AlN thin films.

1.6 Piezoelectric AlN Thin Films for Energy Harvesting

AlN is the main piezoelectric material of wurtzite family. It exhibits a permanent polarization, which indicates that it is a pyroelectric material, and therefore piezoelectric in nature. Regarding energy harvesting, AlN has been extensively used as it allows extraction of decent magnitude of harvested energy at higher impedance than PZT. As it is simpler to process this material at low temperature, it becomes economically amenable for device fabrication [34].

In 2010, Elfrink *et al.* reported the first autonomous wireless sensor node powered by a vacuum-packaged AlN thin film based piezoelectric MEMS energy harvester [35]. This device harvested 100 μW at 572 Hz and 10 ms^{-2} acceleration. In 2011, Ricart *et al.* showed that a simple AlN layer on the top of Si cantilever was able to harvest 100 μW at 100 Hz and 2 ms^{-2} [36]. These two examples are among the best results on piezoelectric thin films in case of vibrating harvesters. Since the 2000s, AlN has largely benefited from the huge development of acoustic resonators for RF filters. Indeed, AlN proves to be easier to process than ZnO. Its stability over a period of time is also good. Although, it exhibits 10 times smaller piezoelectric coefficients basically than perovskites but can potentially work at much higher temperatures as no depolarization occurs [37]. The continuously growing interest in highly piezoelectric AlN thin films for MEMS has led to a focused research on the improvement of its piezoelectric response, which constitutes one of the principal motivations of the present dissertation.

References

- [1] C.-B. Eom, S. Trolier-McKinstry, Thin-film piezoelectric MEMS, MRS Bulletin, 37 (2012) 1007-1017.
- [2] W.P. Mason, Piezoelectricity, its history and applications, The Journal of the Acoustical Society of America, 70 (1981) 1561-1566.
- [3] W. Heywang, K. Lubitz, W. Wersing, Piezoelectricity: Evolution and Future of a Technology, Springer Berlin Heidelberg, 2008.
- [4] S. Katzir, The Beginnings of Piezoelectricity: A Study in Mundane Physics, Springer, 2007.

- [5] P.C. McIntyre, M.R.S. Meeting, *Ferroelectric Thin Films: Symposium*, Materials Research Society, 2000.
- [6] M.S. Vijaya, *Piezoelectric Materials and Devices: Applications in Engineering and Medical Sciences*, CRC Press, 2016.
- [7] G. Helke, K. Lubitz, *Piezoelectric PZT Ceramics*, in: *Piezoelectricity: Evolution and Future of a Technology*, Springer Berlin Heidelberg, Berlin, Heidelberg, 2008, pp. 89-130.
- [8] E. Defaÿ, *Integration of Ferroelectric and Piezoelectric Thin Films: Concepts and Applications for Microsystems*, Wiley, 2013.
- [9] P. Verardi, M. Dinescu, F. Craciun, Pulsed laser deposition and characterization of PZT thin films, *Applied Surface Science*, 154–155 (2000) 514-518.
- [10] W.G. Lee, Y.J. Kwon, Preparation of ferroelectric PZT thin films by plasma enhanced chemical vapor deposition using metalorganic precursors, *Journal of Industrial and Engineering Chemistry*, 14 (2008) 89-93.
- [11] R. Ghodssi, P. Lin, *MEMS Materials and Processes Handbook*, Springer US, 2011.
- [12] B. Gil, *Physics of Wurtzite Nitrides and Oxides: Passport to Devices*, Springer International Publishing, 2014.
- [13] Z. Ke-ming, Z. Ya-pu, H. Fa-quan, L. Dong-qing, Piezoelectricity of ZnO Films Prepared by Sol-Gel Method, *Chinese Journal of Chemical Physics*, 20 (2007) 721.

- [14] C. Jagadish, S.J. Pearton, Zinc Oxide Bulk, Thin Films and Nanostructures: Processing, Properties, and Applications, Elsevier Science, 2011.
- [15] K. Tonisch, V. Cimalla, C. Foerster, H. Romanus, O. Ambacher, D. Dontsov, Piezoelectric properties of polycrystalline AlN thin films for MEMS application, *Sensors and Actuators A: Physical*, 132 (2006) 658-663.
- [16] S.J. Pearton, GaN and Related Materials, Taylor & Francis, 1997.
- [17] O. Hiroshi, T. Yusuke, T. Toshiharu, S. Kenichi, N. Shoichi, Preparation of c -Axis Oriented AlN Thin Films by Low-Temperature Reactive Sputtering, *Japanese Journal of Applied Physics*, 31 (1992) 3446.
- [18] S. Khan, M. Shahid, A. Mahmood, A. Shah, I. Ahmed, M. Mehmood, U. Aziz, Q. Raza, M. Alam, Texture of the nano-crystalline AlN thin films and the growth conditions in DC magnetron sputtering, *Progress in Natural Science: Materials International*, 25 (2015) 282-290.
- [19] B. Jakoby, M.J. Vellekoop, A.T. Tran, H. Schellevis, H.T.M. Pham, C. Shen, P.M. Sarro, Eurosensory XXIV Conference Influence of seed layer on crystallinity and orientation of pulsed — DC sputtered AlN thin-films for piezoelectric actuators, *Procedia Engineering*, 5 (2010) 886-889.
- [20] B. Gil, Low-dimensional Nitride Semiconductors, Oxford University Press, 2002.
- [21] G.F. Iriarte, Structural characterization of highly textured AlN thin films grown on titanium, *Journal of Materials Research*, 25 (2010) 458-463.

- [22] S. Saravanan, E.G. Keim, G.J.M. Krijnen, M. Elwenspoek, Growth and surface characterization of piezoelectric AlN thin films on silicon (100) and (110) substrates, in: A.G. Cullis, J.L. Hutchison (Eds.) *Microscopy of Semiconducting Materials: Proceedings of the 14th Conference*, April 11–14, 2005, Oxford, UK, Springer Berlin Heidelberg, Berlin, Heidelberg, 2005, pp. 75-78.
- [23] H. Shin, Piezoelectric Coefficient Measurement of AlN Thin Films at the Nanometer Scale by Using Piezoresponse Force Microscopy, *Journal of the Korean Physical Society*, 56 (2010) 580-585.
- [24] S. Uzgur, D. Hutson, K. Kirk, Thickness optimization of AlN thin films deposited by RF Magnetron Sputtering, in: *Proceedings of ISAF-ECAPD-PFM 2012*, 2012, pp. 1-4.
- [25] X.-H. Xu, H.-S. Wu, C.-J. Zhang, Z.-H. Jin, Morphological properties of AlN piezoelectric thin films deposited by DC reactive magnetron sputtering, *Thin Solid Films*, 388 (2001) 62-67.
- [26] C. Stoeckel, C. Kaufmann, R. Hahn, R. Schulze, D. Billep, T. Gessner, Pulsed DC magnetron sputtered piezoelectric thin film aluminum nitride – Technology and piezoelectric properties, *Journal of Applied Physics*, 116 (2014) 034102.
- [27] C.M. Lueng, H.L.W. Chan, C. Surya, C.L. Choy, Piezoelectric coefficient of aluminum nitride and gallium nitride, *Journal of Applied Physics*, 88 (2000) 5360-5363.

- [28] H.-Y. Chen, S. Han, H.C. Shih, The characterization of aluminum nitride thin films prepared by dual ion beam sputtering, *Surface and Coatings Technology*, 200 (2006) 3326-3329.
- [29] R. Dhunna, C. Lal, V. Sisodia, D.K. Avasthi, V. Ganesan, I.P. Jain, Structural and optical properties of AlN/Si system, *Materials Science in Semiconductor Processing*, 11 (2008) 126-130.
- [30] S. Wu, R. Ro, Z.-X. Lin, M.-S. Lee, Rayleigh surface acoustic wave modes of interdigital transducer/(100) AlN/(111) diamond, *Journal of Applied Physics*, 104 (2008) 064919.
- [31] J.-L.H. Sean Wua, f, Hsin-Jou Linb, Ding-Fwu Liic, Yi-Chun Chend, and James C. Sunge, Characterization and Piezoelectric Properties of Reactively Sputtered Highly A-axis AlN Thin Films on Diamond Structure IEEE Nanotechnology Materials and Devices Conference (IEEE NMDC 2013), WP (2013) 3-5.
- [32] P.J. Martin, H.A. Macleod, R.P. Netterfield, C.G. Pacey, W.G. Sainty, Ion-beam-assisted deposition of thin films, *Appl. Opt.*, 22 (1983) 178-184.
- [33] A.A. Galuska, Mechanisms of adhesion enhancement using reactive ion mixing, *Nuclear Instruments and Methods in Physics Research Section B: Beam Interactions with Materials and Atoms*, 59 (1991) 487-490.
- [34] R.A. Steven, A.S. Henry, A review of power harvesting using piezoelectric materials (2003–2006), *Smart Materials and Structures*, 16 (2007) R1.

- [35] R. Elfrink, M. Renaud, T.M. Kamel, C.d. Nooijer, M. Jambunathan, M. Goedbloed, D. Hohlfeld, S. Matova, V. Pop, L. Caballero, R.V. Schaijk, Vacuum-packaged piezoelectric vibration energy harvesters: damping contributions and autonomy for a wireless sensor system, *Journal of Micromechanics and Microengineering*, 20 (2010) 104001.
- [36] T. Ricart, P.P. Lassagne, S. Boisseau, G. Despesse, A. Lefevre, C. Billard, S. Fanget, E. Defay, Macro energy harvester based on Aluminium Nitride thin films, in: 2011 IEEE International Ultrasonics Symposium, 2011, pp. 1928-1931.
- [37] D. Briand, E. Yeatman, S. Roundy, O. Brand, G.K. Fedder, C. Hierold, J.G. Korvink, O. Tabata, *Micro Energy Harvesting*, Wiley, 2015.

Chapter 2

Thin Film Deposition and Characterization

This chapter describes ion beam sputtering process based on the concept of ion-solid interaction. Depending on the incident energy, ions interact through Rutherford, weakly-screened Coulomb and hard-sphere collisions. Relation between the collision diameter and screening radius is discussed in each case. Sputter yield is discussed with its dependence on various parameters. Subsequently, experimental setup of ion beam sputter deposition (IBSD) system is described in detail with working principle and specifications of its main components. Characterization tools used to explore surface morphology, structure, composition, optical and piezoelectric response of IBSD grown AlN thin films are discussed in detail with underlying working principle followed by the associated experimental measurement.

Ion beam sputter deposition is one of the established techniques to deposit device-grade thin films. Though it was first used in the late 1960s, but the emission of target particles under the impact of energetic neutral or charged particles on the target material has been a subject matter of investigation for more than a century. The rapid increase of interest in probing sputtering phenomena over last few decades may be explained by the increased recognition of sputtering process in the field of controlled deposition of thin films of almost any material. Generally, sputtering is a process whereby particles are ejected from a solid target material due to bombardment of target by energetic particles. The energetic particles in sputtering may be ions, neutral atoms, electrons or photons. Since most relevant and efficient sputtering applications are performed under bombardment with ions, it is generally defined as the interaction between

energetic incident ions and surface atoms of the target. Ions impinging onto a solid can cause different ion–solid interaction effects because of nuclear and electronic energy losses incurred by the striking ions. These incident ions set off collision cascades in the target. When such cascades recoil and reach the target surface with an energy greater than the surface binding energy, an atom would be ejected. Thus, the interaction between energetic ions and atoms of the solids forms the basis for the understanding of ion beam sputter deposition of thin films which is discussed in details in the succeeding section.

2.1 Ion - Solid Interaction: Mechanism of Sputtering

Two theoretical models have been proposed for sputtering:

- I.** Thermal vaporization theory: The surface of the target is heated enough to be vaporized due to the bombardment of energetic ions.
- II.** Momentum transfer theory: Surface atoms of the target are emitted when kinetic moments of incident particles are transferred to target atoms residing on surface.

The thermal vaporization theory was supported by Hippel in 1926, Sommermeyer in 1935 and Townes in 1944 due to their experimental observations of the Kundsens cosine emission distribution. At that time, the thermal vaporization theory was considered the most important mechanism.

The momentum transfer theory was first proposed by Stark in 1908 and Compton in 1934. The detailed studies by Wehner in 1956, including the observation of spot patterns in single crystal sputtering, suggested that the most important mechanism is not thermal vaporization but the momentum transfer

process. At present sputtering is believed to be caused by a collision cascade in the surface layers of a solid.

The nuclei of the target atoms are screened by electron clouds. The type of collision between an incident particle and the target is determined by incident ion energy and the degree of electron screening [1]. The interaction potential between the incident particle of mass m and a 'stationary' lattice atom of mass M is the screened Coulomb potential between the two nuclei. This potential has the form:

$$V(r) = \frac{Z_1 Z_2}{r} e^2 \exp\left(-\frac{r}{a}\right) \quad (1)$$

Where r is the separation of the two nuclear charges, a is the screening radius of the orbital electrons, and Z_1 and Z_2 are the atomic numbers of the incident particle and the target atom, respectively [2].

For the screening radius a , which can be chosen to fit the Thomas-Fermi field, Bohr suggested the relation:

$$a = \frac{a_0}{(Z_1^{2/3} + Z_2^{2/3})^{1/2}} \quad (2)$$

In this expression, a_0 is the Bohr radius of the hydrogen atom ($= 0.57 \times 10^{-8}$ cm). Another important scattering parameter is the collision diameter b . It is the distance of nearest approach of the two nuclei in a head-on collision in the absence of screening (Rutherford scattering). The parameter b is given by the relation:

$$b = \frac{2Z_1 Z_2 e^2}{\mu v^2} \quad (3)$$

where $\mu = mM/(m + M)$ is the reduced mass and v is the velocity of the incident particle.

Depending on the energy of the incident ions, three types of interaction need to be considered.

- i. Ions with high energies (>10 KeV) interact through the Coulombic repulsions of their nuclear charges (Rutherford collisions).
- ii. At medium energies ($0.1 - 10$ KeV), the electron clouds cause a partial screening of the positively charged nuclei and the collisions are treated as weakly-screened Coulomb collisions.
- iii. At low energies (< 0.1 KeV), there is little penetration of the electron clouds and the collisions approximate hard-sphere type.

Rutherford collisions

The laws of classical Rutherford scattering will be applicable when the screening radius a and collision diameter b satisfy the following condition:

$$\frac{b}{a} \ll 1 \quad \text{and} \quad b \gg \frac{\hbar}{\mu v}$$

Also, Rutherford collisions predominate when the energy E of the incident ion is greater than a limiting energy E_B given by the relation [3]:

$$E_B = 4E_R^2 Z_1^2 Z_2^2 (Z_1^{2/3} + Z_2^{2/3}) \frac{m}{ME_D} \quad (4)$$

where E_B is the Rydberg energy for hydrogen (13.68 eV) and E_d is the energy required to displace an atom from its lattice site. For aluminum (Al), $E_d = 16$ eV.

For the energy range $E > E_B$, expresses the cross section σ_d for a Rutherford collision in which an energy greater than E_d is transferred as [2]:

$$\sigma_d = 4 \frac{m}{M} Z_1^2 Z_2^2 E_R^2 \left(\frac{1 - E_D}{\Lambda E} \right) \quad (5)$$

where,

$$\Lambda = \frac{4mM}{(m+M)^2} \quad (6)$$

Because the term $(1 - E_d/\Lambda E)$ is close to unity in the energy range considered, the mean recoil energy E of the struck atom is:

$$\bar{E} = E_d \ln \left(\frac{E_{\max}}{E_d} \right) \quad \text{for} \quad E_{\max} \gg E_d \quad (7)$$

With

$$E_{\max} = \frac{4mM}{(m+M)^2} E \quad (8)$$

Weak-Screening Collisions

If the kinetic energy E of the incident particle lies within the energy range $E_A < E < E_B$, the screening of the nuclei by the orbital electrons becomes important. The energy limit E_A is given by the relation [2]:

$$E_A = 2E_R Z_1 Z_2 \left(Z_1^{2/3} + Z_2^{2/3} \right)^{1/2} \frac{m+M}{M} \quad (9)$$

The displacement cross section in this energy range is roughly constant and is given by:

$$\sigma = \pi a^2 \quad (10)$$

where, a is screening radius given by equation (2).

The mean recoil energy of the struck atom is:

$$\bar{E} = E_d \left(\frac{E_B}{E} \right) \ln \left(1 + \frac{4E^2}{E_A^2} \right) \quad (11)$$

Hard-Sphere Collisions

The collisions are approximately of the hard-sphere type if the screening radius a and collision diameter b satisfy the following condition:

$$\frac{b}{a} \gg 1 \quad \text{and} \quad a \gg \frac{\hbar}{\mu v} \quad (12)$$

Where, mean-free path, $\lambda = \frac{h}{\mu v}$.

The collision cross section in hard-sphere conditions for the energy range $E < E_A$ is given by:

$$\sigma_d = \left(1 - \frac{E_d}{E_{max}}\right) \pi R^2 \quad (13)$$

where R is the distance of closest approach under hard-sphere conditions and is obtained by solution of :

$$E = \frac{Z_1 Z_2 e^2}{R} \exp\left(\frac{-R}{a}\right) \quad (14)$$

The solution can be expressed in the form

$$R = \frac{a}{\left(Z_1^{2/3} + Z_2^{2/3}\right)^{1/2}} \ln\left(\frac{Z_1 Z_2 e^2 (m+M)}{4\pi R E M}\right) \quad (15)$$

The calculated values of R for a number of target materials bombarded by noble-gas ions of different energies can be read from a graph published by Almen and Bruce [4]. Usually, for the condition shown in equation (12), the collision is considered by the elastic collision theory. The collision is isotropic and the total scattering cross section is approximated to be πR^2 . For a small E the R is approximately the atomic radius of the incident particles.

The energy distribution of the struck atoms is assumed to be uniform in the energy range $0 < E \leq E_{max}$ so that the mean energy is given by:

$$\bar{E} = \frac{1}{2} (E_{max} + E_d) \quad (16)$$

Sputtering

Thus sputtering is an event which is initiated by the first collision between incident ions and target surface atoms followed by the second and the third

collisions between the target surface atoms. The displacement of target surface atoms will eventually be more isotropic due to successive collisions and atoms may finally escape from the surface. Figure 2.1 shows the features of sputtering collision in the target surface. Efficiency of this sputtering phenomenon is determined by the sputter yield.

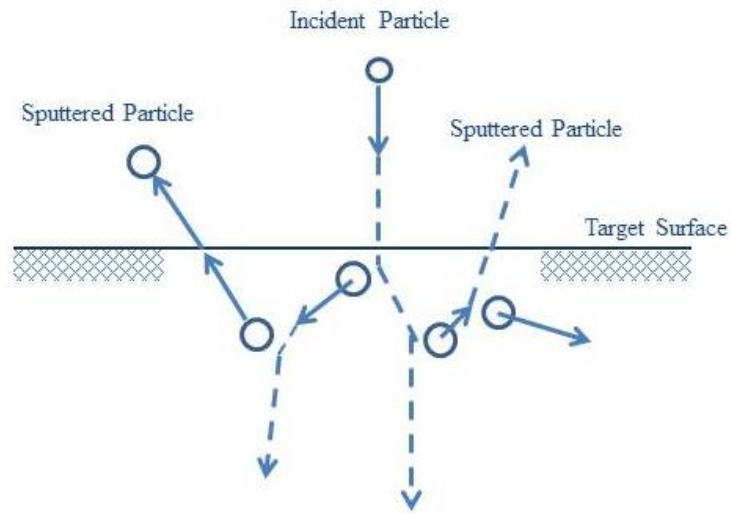


Figure 2.1 Incident ions on the target surface and ejection of sputtered particles.

The sputter yield S , which is the removal rate of surface atoms due to ion bombardment, is defined as the mean number of atoms removed from the surface of a solid per incident ion and is given by

$$S = \frac{\text{Atoms removed}}{\text{Incident ions}} \quad (17)$$

The sputter yield is generally influenced by the following factors;

- i. Energy of incident particles
- ii. Target materials
- iii. Incident angles of particles
- iv. Crystal structure of the target surface

v. Mass of the sputter gas atoms

According to the elastic-collision theory, the maximum possible energy transferred in the first collision, T_m , is given by [1]:

$$T_m = \frac{4mM}{(m+M)^2} E \quad (18)$$

where m and M represent masses of the incident ions and target atoms, respectively. E is the energy of incident ions. In the first order of approximation the sputter yield S is proportional to T_m . The sputter yield from a given target material bombarded with different elements is given by:

$$S = k \frac{1}{\lambda(E)\cos\theta} \frac{mM}{(m+M)^2} E \quad (19)$$

Where k is a constant which includes different target material constants, λ is the mean free path for elastic collisions near target surface. θ is the angle between the normal on the target surface and the direction of the incident ions. The mean free path is given by:

$$\lambda = \frac{1}{\pi R^2 n_o} \quad (20)$$

where n_o is the number of lattice atoms per unit volume, and R is the collision diameter given by equation (15). Almen et al. have shown that the constant k is expressed by the experimental relationship:

$$k = a \exp \left(\frac{-b\sqrt{m}}{m+M} E_B \right) \quad (21)$$

and found the sputter yield as

$$S = 4.24 \times 10^{-8} n_o R^2 E \frac{mM}{(m+M)^2} \exp \left(-10.4 \frac{\sqrt{m}}{m+M} E_B \right) \quad (22)$$

where E_B is the binding energy of the target [4].

There are several different ways to implement sputter deposition of thin films, but to get device-grade thin films, ion beam sputter deposition (IBSD) is an excellent technique that has been used in the present thesis work. Its main components are described in the next section.

2.2 Ion Beam Sputter Deposition System: Experimental Set-up

Experimental set-up of IBSD system and its main component are shown in figure 2.2. The main deposition chamber is equipped with a turbo molecular pump (TMP) backed by a scroll pump to evacuate it to the base pressure of 2×10^{-7} mbar. A titanium sublimation pump (TSP) is also provided in the main deposition chamber for selective removal of other background reactive gases like oxygen (O_2 and H_2O -vapors). The load lock chamber is pumped by a separate TMP backed by a scroll pump which usually achieves a base pressure of 5×10^{-8} mbar. For deposition, the substrate is loaded into the load-lock chamber and is transferred into the main chamber with a linear transfer rod through an isolation valve. This prevents the deterioration of base vacuum of the main deposition chamber and maintains atmospheric purity within the chamber. To enable systematic monitoring of deposition parameters, the chamber is equipped with a number of measuring instruments such as quartz crystal thickness monitor, residual gas analyzer, and high vacuum gauges. A substrate manipulator is also provided to allow substrate heating and rotation during deposition.

During deposition, the metal atom flux is provided by sputtering target material with an ion beam extracted from a 6 cm RF ion source. Reactive and assistive flux is provided directly to the substrate surface using an end-Hall type

DC ion source. Thus IBSD system can be used in assistive as well as reactive-assistive mode. The specifications and working principle of 6 cm RF ion source and assistive end-hall type ion source are described briefly in the following sections.

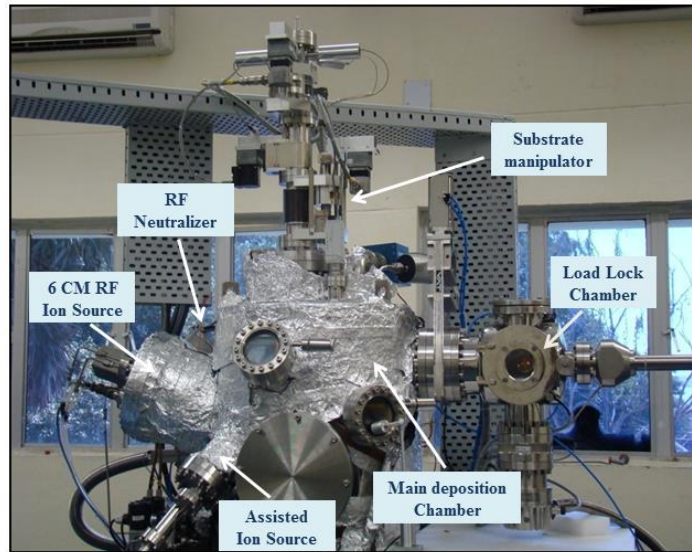


Figure 2.2 Experimental set-up of ion beam sputter deposition (IBSD) system.

2.2.1 6 cm RF Ion Source: Specifications of the main ion source are following.

- Beam size (at grids): - 6 cm
- Maximum beam current: -150 mA
- Beam Energy: -100 eV to 2000 eV
- Gas flow: - 6 to 15 sccm Ar
- Gases: - Ar (all inert gases), O₂, N₂ and other reactive gases
- Cooling water flow: - 2 lpm
- Grid configuration: - 3 grids
- Beam neutralization: – Radio Frequency Neutralizer

Working Principle: A schematic diagram of 6 cm RF ion source is shown in figure 2.3.

- Gas is introduced into the upstream end of the quartz discharge chamber through a specially designed gas isolator assembly.
- RF-power at 13.56 MHz is inductively coupled into the ion source discharge chamber to ionize the gas.
- Some of the ions that are produced in the discharge reach the three grids of accelerator system.
- Ions are accelerated through the apertures of the –ve accelerator grid and are focused by the +ve screen grid.
- The accelerated ions form a directed beam of mono-energetic ions.

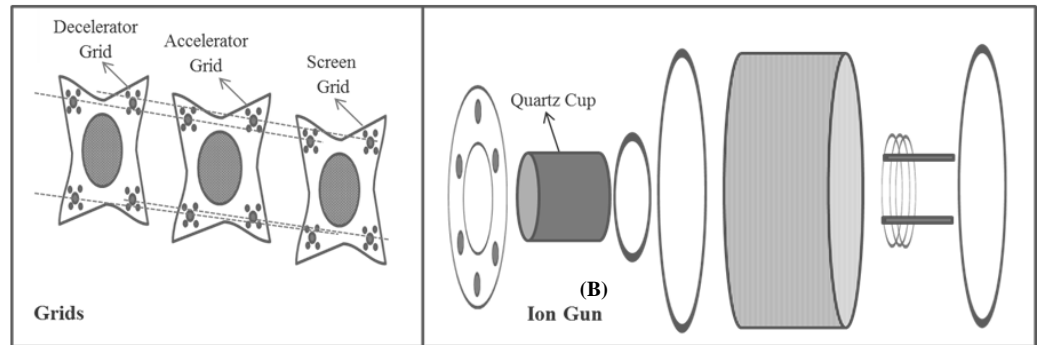


Figure 2.3 Internal arrangement of RF ion source with three grid accelerator system.

2.2.2 End-Hall Assisted Ion Source: Specifications of the assisted ion source are as following.

- Maximum discharge power – 300W max. (200W conti.)
- Discharge current, (I_A) - 0.2 to 1 A
- Mean Ion Beam Energy – 50 eV to 180 eV
- Gas flow - 2 to 20 sccm of Ar

- Gases - Ar (all inert gases), O_2 , N_2 and other reactive gases

Working Principle: A schematic diagram of end-hall ion source is shown in figure 2.4.

- Operates by producing a low pressure plasma near a cusped magnetic field that lies between an e^- emitter and angled anode.
- A DC magnetic field is formed by a permanent magnet and the source's open ended stainless steel shell.
- Primary e^- emitted from the cathode are drawn to the cone-shaped anode by means of an applied DC potential, through which a working gas is injected.
- The accelerated e^- strike and ionize the input gas atoms and form plasma.
- As the e^- drift toward the anode, the magnetic field impedes their mobility or flow.
- The resistance to e^- flow results in a space charge within the plasma near the anode.
- This spatially varying potential field ultimately accelerates ions away from the source anode to form an ion beam.

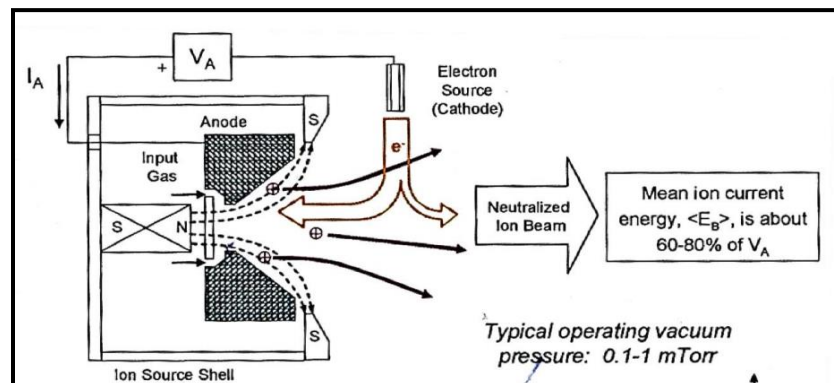


Figure 2.4 Schematic representation of End-hall ion source.

2.2.3 RF Neutralizer: Provides e^- to minimize the charging of substrate surfaces and beam divergence.

Working Principle: A schematic diagram of end-hall ion source is shown in figure 2.5.

- An inert gas is introduced in to a small SS discharge chamber.
- Gas is ionized by the fields induced by an RF coil wrapped around the discharge chamber.
- This glow discharge containing ions and electrons is further sustained by the 'collector' and 'keeper'.
- Collector collects the ions and keeper collects the electrons alone.
- Then keeper and collector are biased to emit electrons.

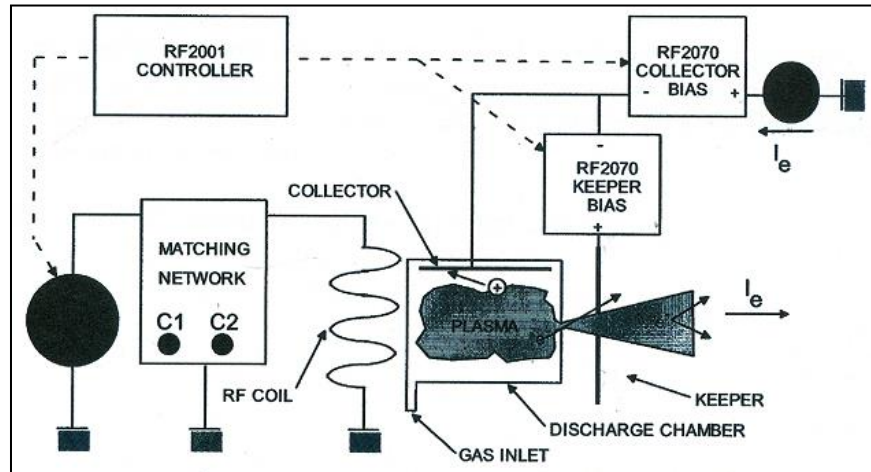


Figure 2.5: Schematic diagram of basic components of RF Neutralizer (RFN).

2.3 Deposition Modes in IBSD: Thin films can be deposited by using IBSD

system in the following two modes:

- I. **Assistive IBSD:** When same noble gas is used in the assistive ion source as is used in the main ion source (usually argon (Ar)). In this mode, only

density of nucleation sites is increased on the substrate surface which in turn increases the density as well as uniformity of the film.

II. Reactive Assistive IBSD: To deposit any compound of solid elements from periodic table with a gaseous element (like N, O, CH₄ etc.), this mode is used. In this case, the main ion source uses the flux of an inert gas (like Ar) and assisted ion source is fed with a reactive gas (like N₂, O₂ and CH₄).

Generally, deposition of AlN thin films for the present thesis was carried out in reactive assistive IBSD mode. For this, metal atom flux was obtained by sputtering an Al-target with an inert ion beam of Ar⁺ ions of certain energy extracted from the main 6 cm RF ion source. Simultaneously, nitrogen (N₂) gas was fed into the assisted ion source and a broad beam of N⁺/N₂⁺ ions was extracted and directed towards substrate surface for increasing the nucleation density as well. In this scenario, sputtered Al atoms/ions arrived on the surface of the substrate immersed in N⁺/N₂⁺ ions. As both the metal and gas are in active state on the substrate surface, they undergo a chemical reaction easily with an enhanced density of AlN thin film. Thus reactive assistive IBSD provides dense and smooth films with very clean interface. For the present investigations, different AlN thin films were grown on Si(100) substrate by changing the following parameters.

- i. Substrate temperature during growth*
- ii. Assisted ion energy*
- iii. Deposition time*

2.4 Characterization Techniques:

Characterization techniques used to assess the quality of reactive assistive IBSD grown AlN thin films on Si(100) substrates are categorized as shown in table 2.1. Each of the technique mentioned in table 1 is explained briefly in the subsequent sections.

Table 2.1 Characterization tools used to investigate different properties of reactive assistive IBSD grown AlN thin films.

Property	Characterization Tool
Surface morphology	<ul style="list-style-type: none"> ▪ Atomic Force Microscopy (AFM) ▪ Scanning electron Microscopy (SEM)
Structure	<ul style="list-style-type: none"> ▪ X-ray Diffraction (XRD) ▪ Transmission Electron Microscopy (TEM)
Composition	<ul style="list-style-type: none"> ▪ X-ray Photoelectron Spectroscopy (XPS)
Defects in microstructure	<ul style="list-style-type: none"> ▪ Photoluminescence Spectroscopy (PL) ▪ Positron Annihilation Spectroscopy
Piezoelectricity	<ul style="list-style-type: none"> ▪ Atomic Force Microscopy (AFM) ▪ X-ray Diffraction (XRD) ▪ Capacitance-Voltage (C-V) measurements

2.4.1 Atomic Force Microscopy (AFM):

Working Principle: Atomic force microscope (AFM) was invented in 1986 by Gerd Binnig, Calvin F. Quate and Christopher Herber [5]. The AFM working principle involves the measurement of the interactive force between a tip and the sample surface using special probes made of an elastic cantilever with a sharp tip on the end as shown in figure 2.6. The force applied to the tip by the surface, results in bending of the cantilever. By measuring the cantilever deflection, it is possible to evaluate the tip–surface interactive force to map the morphology of the surface [6].

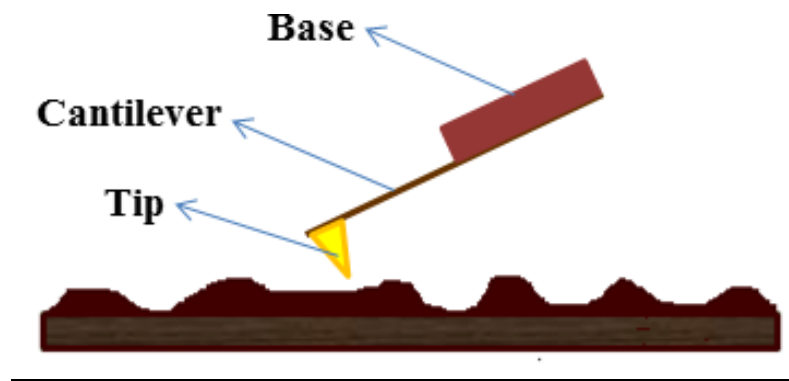


Figure 2.6: Scanning of surface morphology using atomic force microscopy (AFM).

Measurement: All the samples used in the experimental studies that form a part of the present thesis were characterized for their surface morphology using an Atomic Force Microscope (AFM) (NT-MDT, Russia). Topographic images were obtained in semi-contact mode using a commercial Si-tip cantilever with a tip radius of 35 nm. For better statistics, topographic images and corresponding line profiles were obtained at several $1 \times 1 \mu\text{m}^2$ scan area at different locations over a 10 mm x 10 mm film surface. Root mean square (rms) of surface heights at these different locations was considered as roughness value of the film. A representative image of surface morphology of AlN thin film deposited for 15 minutes is shown in figure 2.7 both in 2D and 3D view. These images are discussed in more details in chapter 3. Also, measurement of piezoelectric response of AlN thin films using AFM is presented in an elaborated way in chapter 6.

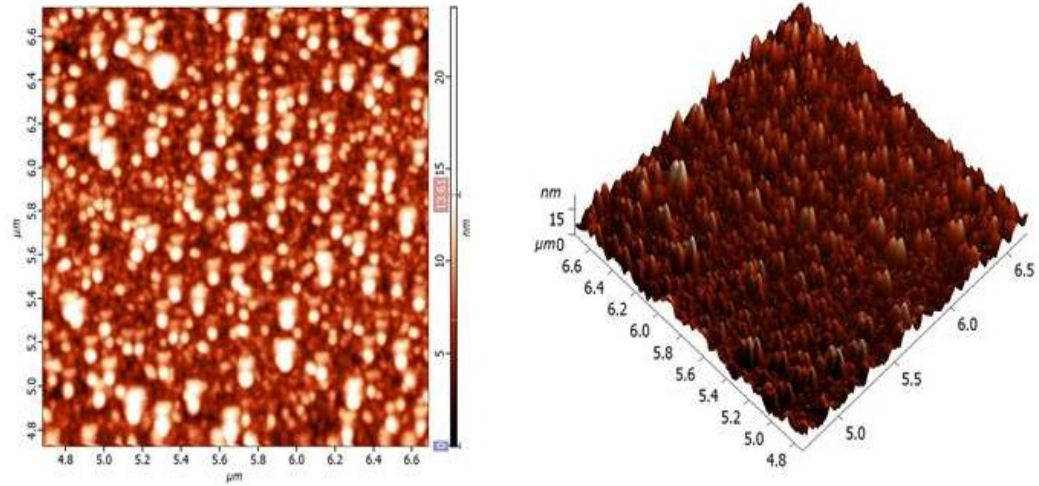


Figure 2.7: 2D and 3D surface morphology of AlN thin films deposited on Si(100) substrate for 15 minutes using reactive assistive IBSD.

2.4.2 Scanning Electron Microscopy (SEM):

Working Principle: The basic principle of scanning electron microscope (SEM) is that a beam of electrons is generated by a suitable source, typically a tungsten filament or a field emission gun under high vacuum. The electron beam is accelerated through a high voltage (e.g.: 20 kV) and pass through a system of apertures and electromagnetic lenses to produce a thin beam of electrons. Then this beam of electrons scans the surface of the specimen by means of scan coils. Electrons are emitted from the specimen by the action of the scanning beam and collected by a suitably-positioned detector [7]. A schematic diagram of SEM is shown in figure 2.8.

Measurement: The topographic features of the AlN thin films used in the present thesis work were analysed by SEM (Supra 55, Zeiss, Germany) for the films deposited at different substrate temperatures. As AlN thin films are insulating in

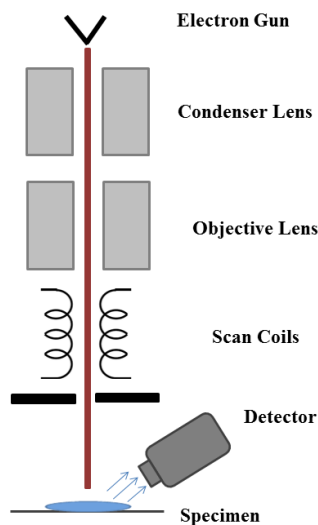


Figure 2.8 Schematic diagram of scanning electron microscope (SEM).

nature, electron gun was operated at 3kV to obtain the images. Few representative SEM images of AlN thin films deposited up to 500°C substrate temperature are shown in figure 2.9.

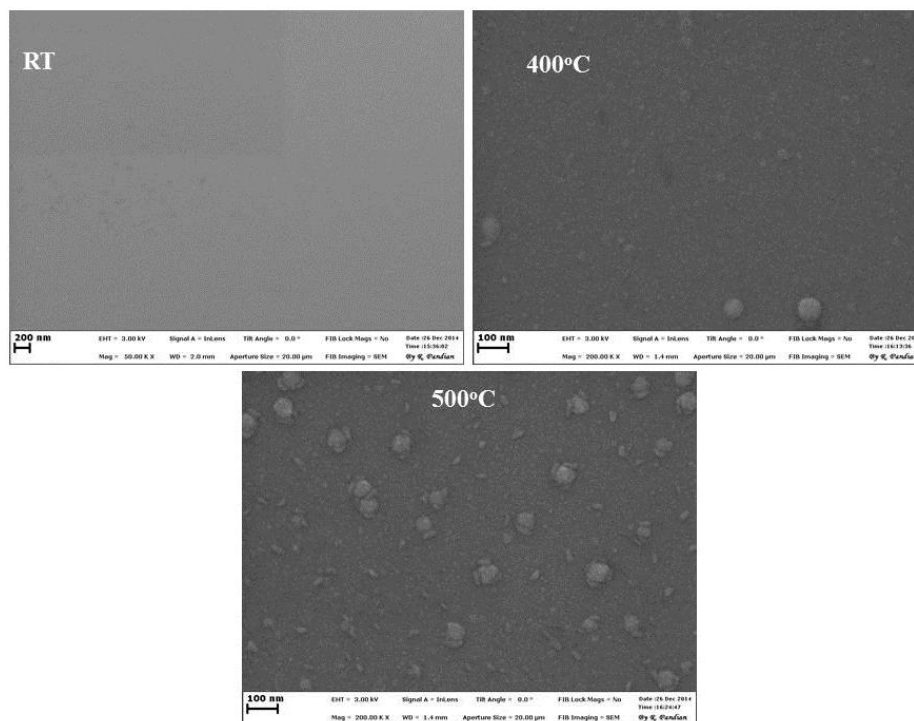


Figure 2.9 SEM images of AlN thin films at different substrate temperatures.

2.4.3 X-ray Diffraction (XRD)

Working Principle: The objective behind acquisition of X-ray diffraction pattern from crystals is to arrive upon a particular diffraction condition in which the scattered X-rays from atoms and the incident X-rays constructively reinforce each other to produce a detectable diffraction beam. In other words, the diffraction condition is satisfied when differences in path length between X-rays scattered from crystals and that of the incident X-rays becomes an integer multiple of wavelength. For this purpose, the most important and familiar method is given by Bragg law which incorporates Bragg angle. In order to facilitate the understanding of Bragg law, figure 2.10 is given. It is also required to remember the following two geometric relationships [8]:

- The angle between the incident X-ray beam and the normal to the reflection plane is equal to that between the normal and the diffracted X-ray beam. The incident X-ray beam, the plane normal, and the diffracted X-ray beam are always coplanar.
- The angle between the diffracted X-ray beam and the transmitted one is always 2θ , and this angle is called “the diffraction angle.”

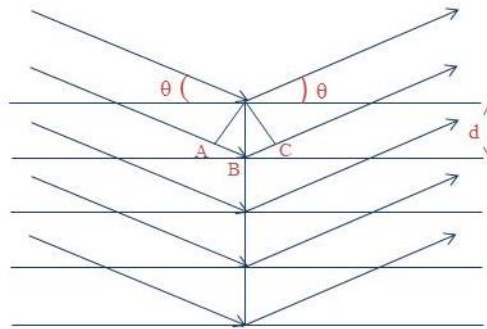


Figure 2.10 Schematic diagrams of X-rays by a crystal (Bragg condition).

If the incident X-rays of wavelength (λ) strike a crystal where all atoms are placed in a regular periodic array with interplanar spacing d , diffraction beam of sufficient intensity is detected only when the “Bragg condition” is satisfied:

$$2d\sin\theta = n\lambda$$

where n is called the order of reflection and is equal to the number of wavelengths in the path difference between diffracted X-rays from adjacent crystal planes [8](see figure 2.10).

Basic Instrument: An X-ray thin film diffractometer that enables a wide variety of measurements consists of the following five major components [9]:

- X-ray source
- Incident optical system
- Goniometer
- Receiving optical system
- Detection section

A *four-circle diffractometer* is generally composed of four axes (Figure 2.11):

- i. **ω -axis:** Sample rotation axis (Angle between incident X-rays and sample surface)
- ii. **ϕ -axis:** In-plane rotation axis
- iii. **χ -axis:** Tilting axis
- iv. **2θ -axis:** Detector axis (Angle between incident X-rays and detector)

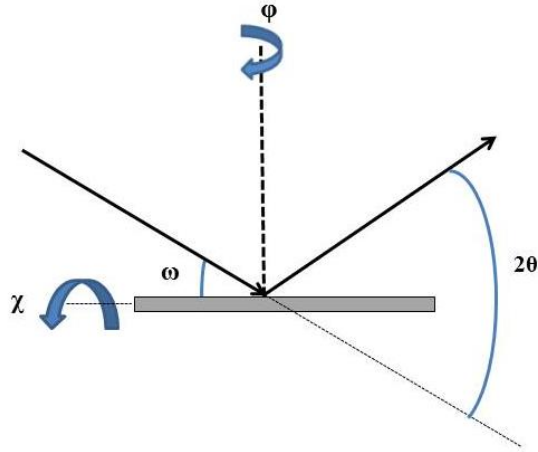


Figure 2.11 Schematic of four axis of diffractometer showing different angles between incident X-ray beams and sample surface.

Different Geometries of XRD: Main diffraction geometries used to investigate the crystal structure of reactive assistive IBSD grown AlN thin films for the present thesis work are explained briefly as following [10].

I. Asymmetric-Reflection Measurements (ω - 2θ Scan): Diffraction in this geometry is also known as grazing incidence X-ray diffraction (GIXRD). It can be used to measure diffraction peaks, specifically, from a thin film. This measurement is performed under a specific diffraction geometry in which an incident X-ray beam is kept at a small angle (ω : usually much lower than 1°) with respect to thin film surface and the detector on 2θ -axis is scanned to record diffraction intensities from a thin film. This is shown in figure 2.11.1. The X-ray penetration depth inside a thin film can be controlled precisely. Therefore, the asymmetrical-reflection measurement can be used to obtain high diffraction intensities from thin film samples suppressing signals from the substrate.

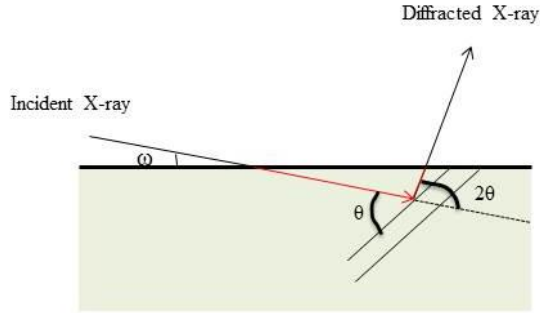


Figure 2.11.1 Asymmetric-reflection scan or GIXRD geometry for measurements on thin film samples.

II. Symmetric-Reflection Measurements (θ - 2θ Scan): In symmetric reflection, both angles of the incident and the diffracted X-rays against the sample surface plane are equal. As a result, diffraction intensities are obtained only from those lattice planes which are parallel to the sample surface as shown in figure 2.11.2. Thus for those thin films which grow with a preferred orientation, especially an epitaxial thin film, the θ - 2θ scan is a primary indicative technique.

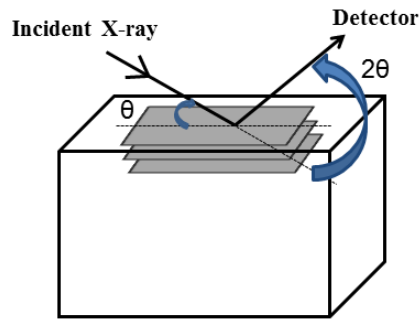


Figure 2.11.2 Symmetric-reflection scan geometry.

III. Rocking Curve (ω -Scan): It is well known that the direction (or axis) of preferred orientation and the degree of orientation are two important factors that can strongly affect the physical properties of a thin films. The orientation

axis (or texture) can be determined by a symmetric reflection measurement and the degree of preferred orientation can be obtained by a rocking curve measurement as shown in figure 2.11.3. This measurement is performed by rocking the thin film sample while the detector is kept fixed at 2θ angle to record diffraction intensities from the preferentially oriented lattice-planes. The degree (or distribution) of preferred orientation is estimated from the full width at half maxima (FWHM) of the rocking curve profile which is discussed in more details in chapter 6.

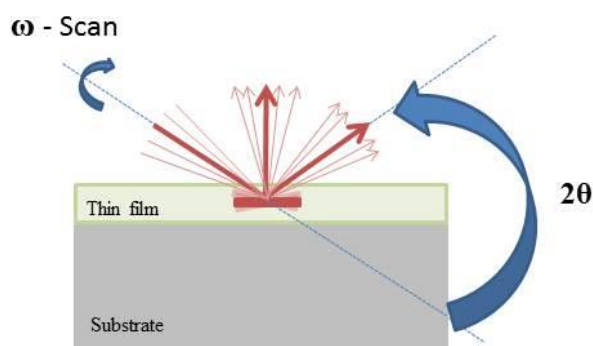


Figure 2.11.3 Rocking curve geometry on a textured thin film sample.

Measurement: Characterization of the AlN thin film samples was carried out for their microstructural phase formation in wurtzite hexagonal phase. It was carried out using high resolution X-ray diffraction (HR-XRD, Bruker D8, Germany). Gobel mirror, a graded multilayer parabolic X-ray beam conditioner was used to convert the divergent X-ray beam from a line focus tube to an intense monochromatic quasi-parallel beam of $\text{CuK}\alpha_1$ ($\lambda=1.54059 \text{ \AA}$) operated at 45 kV and 100 mA.

HR-XRD analysis of these samples was carried out in different geometries for different structural informations.

- I. Grazing incidence X-ray diffraction (GIXRD) was carried out to investigate the crystal structure of polycrystalline AlN thin films.
- II. $\Theta/2\Theta$ symmetric scan as a signature of preferred orientation in film microstructure.
- III. Rocking curve measurement (ω -scan) was performed to determine the degree of orientation and microstrain in the film microstructure.

Representative XRD measurements in different geometries performed on AlN thin films on Si(100) substrate is shown in figure 2.12. Extended results of XRD analysis for different growth conditions are presented in chapter 4.

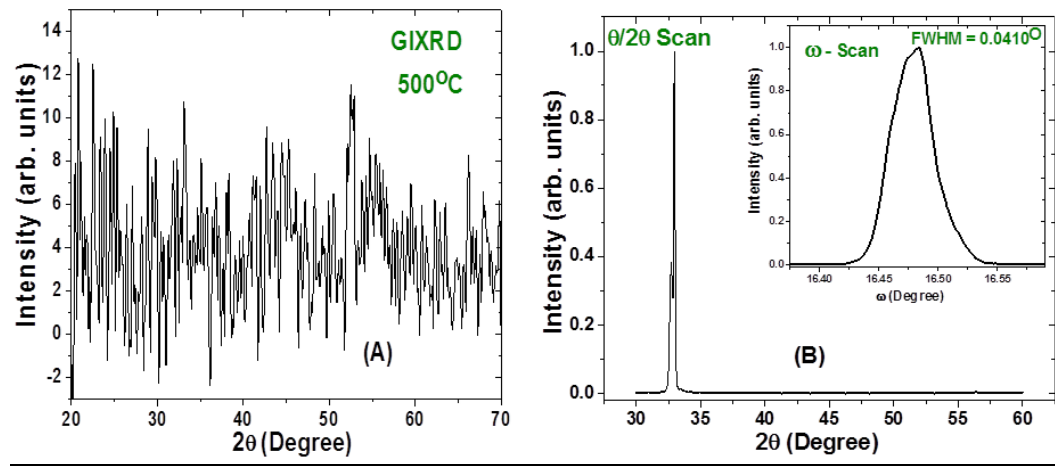


Figure 2.12: XRD analysis of AlN thin films grown on Si (100) substrate at 500°C temperature in different geometries, (A) GIXRD, (B) Symmetric ($\Theta/2\Theta$ scan) and inset shows corresponding rocking curve (ω -scan).

2.4.4 Transmission Electron Microscopy (TEM)

Working Principle: Transmission electron microscopy uses near relativistic electron beam normally accelerated by hundreds of kV supply voltage. The electron beam behaves like a wave front with wavelength about a million times shorter than light waves. When an electron beam passes through a thin-section

specimen of a material, electrons are scattered. Depending on the mode of operation, a sophisticated system of electromagnetic lenses focuses the scattered electrons into an image or a diffraction pattern, or a nano-analytical spectrum [11]. A schematic diagram of TEM is shown in figure 2.13.

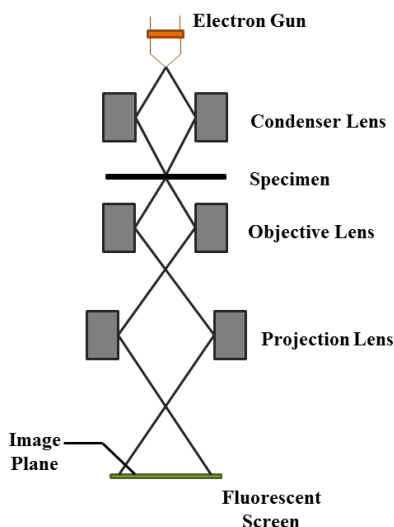


Figure 2.13 Schematic diagram of a conventional transmission electron microscope showing different lenses and trajectories.

Measurement: Structural information of the reactive assistive IBSD grown AlN thin films was also obtained with high resolution TEM (Libra 200FE/HR-TEM). Selected area electron diffraction (SAED) patterns of these films were analyzed to determine the evolution of the crystallographic phases and average crystallite size (d) at different substrate temperatures. Simultaneously, bright and dark field images were obtained to determine the crystallite size distribution in film microstructure. Representative dark field image and corresponding SAED pattern of AlN/Si(100) are shown in figure 2.14. Results on crystallite size distribution are presented and discussed in more details in chapter 4.

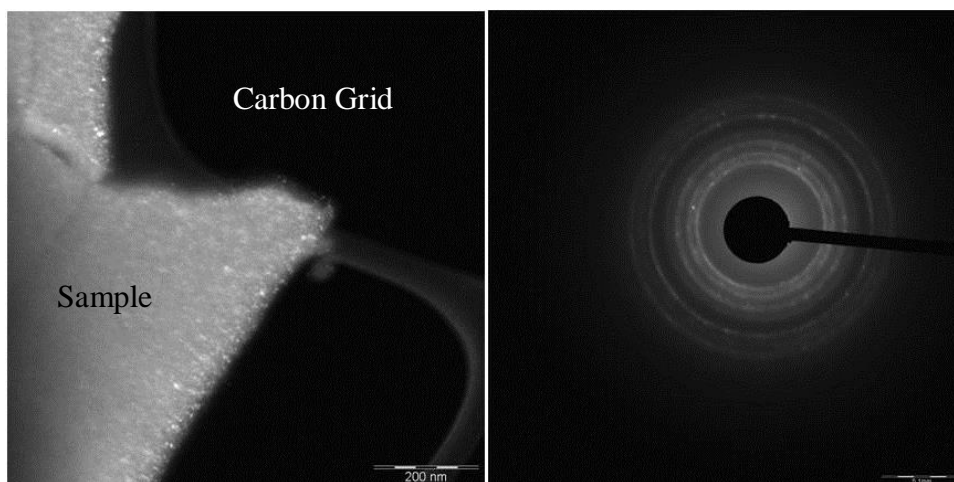


Figure 2.14: Dark field image and corresponding selected area electron diffraction (SAED) pattern of AlN thin films deposited on Si(100) substrate at 400°C.

2.4.5 X-ray photoelectron Spectroscopy (XPS)

Working Principle: X-ray photoelectron spectroscopy (XPS) is a surface characterization technique that can analyze a specimen's elemental composition on the solid surface along with their respective chemical states. Using relative sensitivity factors, their atom percentage concentrations are easily determined. It can detect all of the elements except hydrogen and helium. When the surface of the specimen is irradiated with X-rays of sufficient energy, electrons in specific bound states get excited and knock the photoelectron away from the nuclear attraction force of an element. Some of the photo-ejected electrons scatter inelastically through the sample enroute to the surface, while others undergo prompt emission and suffer no energy loss in escaping the surface into the surrounding vacuum. Once these photo-ejected electrons are in the vacuum, they are collected by an electron analyzer that measures their kinetic energy. An electron energy analyzer produces an energy spectrum of intensity (number of photo-ejected electrons versus time) versus binding energy (the energy the

electrons had before they left the atom). Each prominent energy peak on the spectrum corresponds to a specific element [12].

- i. Identification of the elements constituting the microstructure of the material.
- ii. Composition (or elemental concentration) of each element as specific energy of an elemental core level transition occurs at a specific binding energy that can uniquely be identified (and in favorable cases quantified) for a specific element.

A schematic of XPS instrument is shown in figure 2.15. Chapter 4 presents more elaborate discussion on XPS of AlN thin film and determination of its *at. %* concentration.

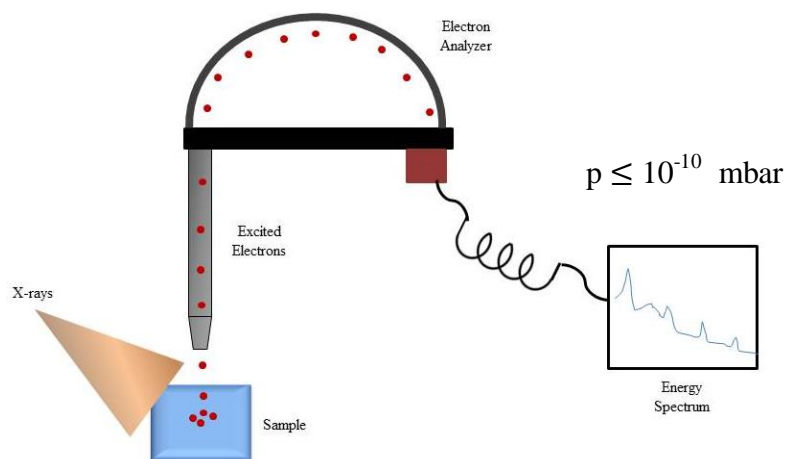


Figure 2.15 Schematic diagram of X-ray photoelectron spectroscopy (XPS).

Measurement: X-ray photoelectron spectroscopy (XPS, M/s Specs, Germany) was used to explore the composition of AlN thin films, deposited at different substrate temperatures, using a monochromatic X-ray source of aluminum with $K_{\alpha} = 1486.6$ eV operated at 15 KV and 22 mA. A concentric hemispherical analyzer of 150 mm diameter was used to analyze the photoelectrons with an

electron takeoff angle of 90° . The base pressure of the spectrometer was 2.3×10^{-10} mbar which was consistently maintained during measurement. The spectrometer was calibrated to the Ag-3d_{5/2} peak at 368.53 eV and C-1s peak at 284.6 eV. All the spectra were recorded with a resolution of 0.25 eV. For binding energy reference, C-1s peak was used. Survey spectra were obtained in the energy range 0 to 1000 eV while core level spectra were collected to determine the elemental atomic concentration of each element appearing in the corresponding survey spectrum. These results and methodology to obtain composition of AlN thin film in atom percentage is presented in chapter 4. A representative survey scan on AlN thin film on Si(100) grown at 500°C is shown in figure 2.16.

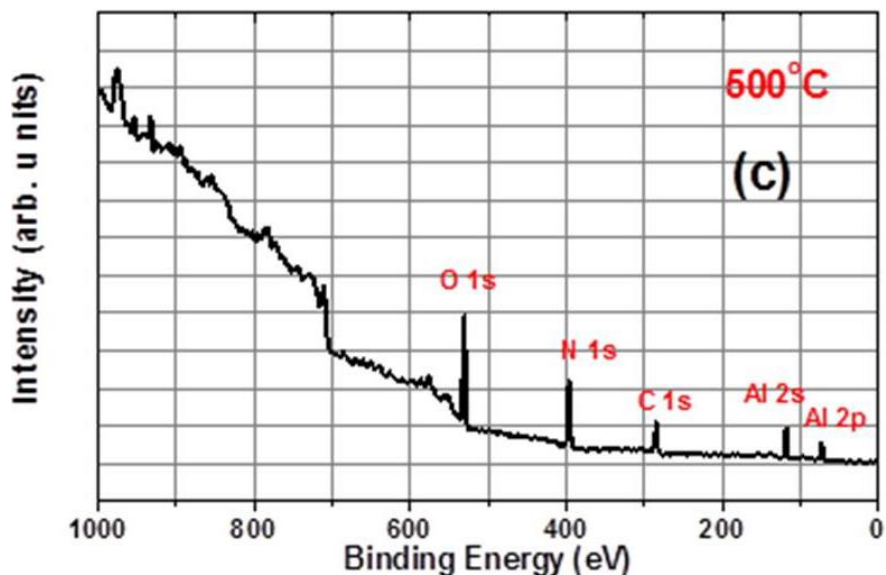


Figure 2.16: Survey spectrum of AlN thin film grown on Si(100) substrate at 500°C temperature.

2.4.6 Positron Annihilation Lifetime Spectroscopy (PALS)

Working Principle: The basic principle of positron annihilation lifetime spectroscopy (PALS) lies in the fact that a positron will annihilate through

interaction with electrons releasing gamma (γ) rays which can be detected. The time between emission of positrons from a radioactive source and detection of gamma rays due to annihilation corresponds to the lifetime of positron [13].

Doppler Broadening Spectroscopy

Doppler-broadening spectroscopy has the advantage of a compact setup with a higher counting rate and allows the simultaneous measurement of positron life time. Due to its relative ease of implementation and its high defect sensitivity, this technique accounts for most of the condensed matter physics work carried out normally with slow positrons. Depth resolved Doppler broadening measurements can be employed to perform depth profiled defect analysis by varying the incident beam energy. More details about this technique can be found in any standard text book [13 - 14].

Measurements: Depth resolved Doppler broadening measurements were carried out on AlN/Si samples using the low energy positron beam. The positron beam energy (E_p) was varied from 250 eV to 21.5 keV in steps of 0.5 keV and a Doppler broadened 511 keV annihilation energy spectrum was obtained for each positron beam energy using HP-Ge detector having 30 % efficiency. From each annihilation spectrum, S-parameter (S) was deduced and plotted as a function of positron beam energy which are presented and discussed in detail in chapter 4.

2.4.7 Photoluminescence Spectroscopy:

Working Principle: Photoluminescence spectroscopy is a contactless, nondestructive method of probing the electronic structure of materials. Light is directed onto a sample, where it is absorbed and imparts excess energy into the

material in a process called photo-excitation. One way this excess energy can be dissipated by the sample is through the emission of light, or luminescence. In the case of photo-excitation, this luminescence is called photoluminescence [15].

The energy of the emitted light (photoluminescence) relates to the difference in energy levels between the two electron states involved in the transition between the excited state and the equilibrium state. The quantity of the emitted light is related to the relative contribution of the radiative process. By measuring the spectrum of this luminescence, valuable information about the energy levels in the semiconductor can be obtained [16]. A schematic diagram of a typical PL spectrometer is shown in figure 2.17.

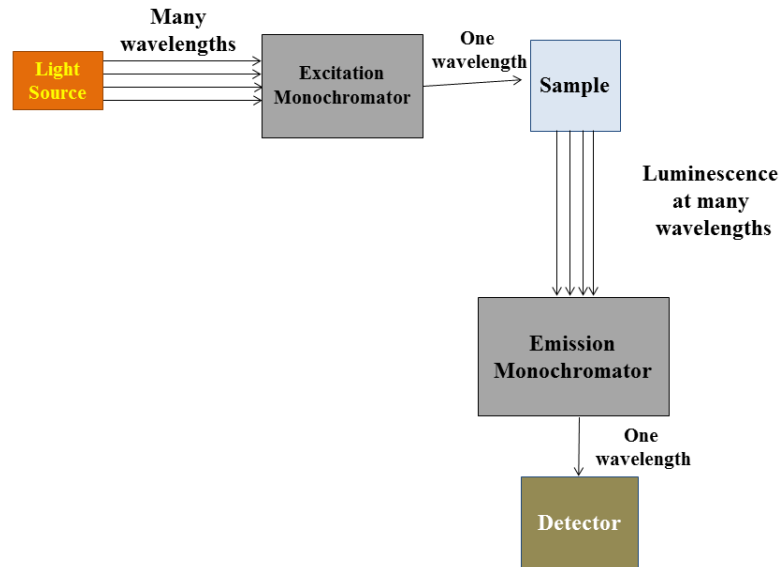


Figure 2.17 Schematic diagram of a photoluminescence (PL) spectrometer.

Measurements: Presence of charged point defects (V_{Al}^- and V_N^+) in AlN thin films grown by reactive assistive IBSD was confirmed by photoluminescence (PL) spectroscopy with 325 nm He-Cd laser excitation using a Raman microscope

(Renishaw plc, U.K., model inVia). These observations are discussed in more details in Chapter-6.

2.4.8 UV-VIS Spectrophotometer: Design and working principle:

A spectrophotometer is used for the quantitative measurement of the reflected and transmitted light as a function of its wavelength when it is incident on the sample object. The branch of spectroscopy which employs spectrophotometer to characterize the reflection and transmission properties of a material is known as spectrophotometry. The main constituents of a spectrophotometer are shown in figure 2.18 which can be briefly explained as following:

- (I). The source of light radiation of appropriate wavelengths
- (II). A means of isolating light of a single wavelength and getting it to the sample compartment - Monochromator and optical geometry.
- (III). A means of introducing the test sample into the light beam - Sample handling compartment.
- (IV). A means of detecting and measuring the light intensity.

A spectrophotometer could be single beam or double beam type. A double beam spectrophotometer compares the light intensity between two light paths. One path containing a reference sample. In the case of thin films, this reference sample is taken same as the substrate. The light from the source falls onto a monochromator to produce monochromatic radiation which is then scanned through the sample under investigation and the reference sample simultaneously. A fraction of the incident wavelengths is transmitted through, or reflected from, the sample under investigation and the reference sample. The resultant light strikes the detector

which compares the relative intensity of the two beams. At this last stage, the relative currents are converted into reflectance and/or transmittance values which are further analysed to extract the optical band-gap, energy tails, refractive index and extinction coefficients of the samples.

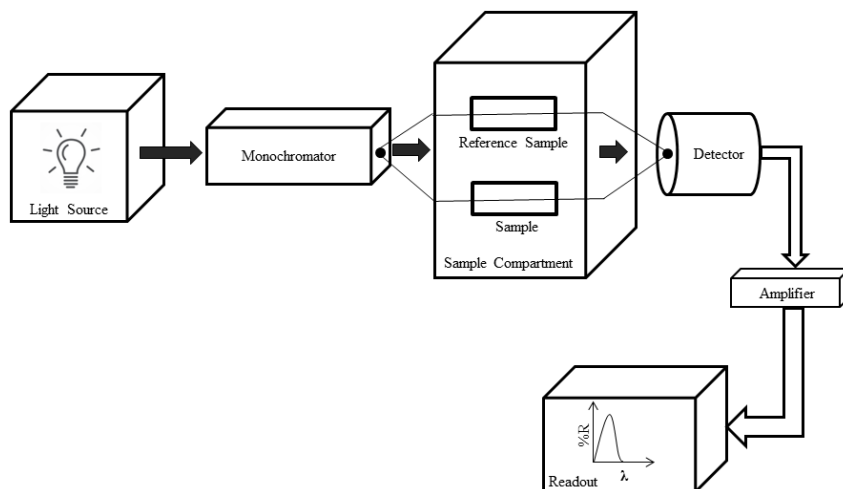


Figure 2.18 Basic block diagram of a spectrophotometer showing constituent components.

References

- [1] K. Wasa, I. Kanno, H. Kotera, Handbook of Sputter Deposition Technology: Fundamentals and Applications for Functional Thin Films, Nano-materials and MEMS, William Andrew, 2012.
- [2] N. Bohr, The Penetration of Atomic Particles Through Matter, Kgl. Danske Vidensk. Selsk., mat .. fysiske Medd., 8 (1948) 18.
- [3] G.H. Kinchin, R.S. Pease, The Displacement of Atoms in Solids by Radiation, Reports on Progress in Physics, 18 (1955) 1.
- [4] O. Almén, G. Bruce, Sputtering experiments in the high energy region, Nuclear Instruments and Methods, 11 (1961) 279-289.

- [5] G. Binnig, C.F. Quate, C. Gerber, Atomic Force Microscope, *Physical Review Letters*, 56 (1986) 930-933.
- [6] V. Sharapov, *Piezoceramic Sensors*, Springer Berlin Heidelberg, 2011.
- [7] D.B. Holt, D.C. Joy, *SEM Microcharacterization of Semiconductors*, Elsevier Science, 2013.
- [8] B.D. Cullity, *Elements of X Ray Diffraction*, Pearson India Education Services Pvt. Ltd., 2014.
- [9] C. Suryanarayana, M.G. Norton, *X-Ray Diffraction: A Practical Approach*, Springer US, 2013.
- [10] H. Lüth, *Solid Surfaces, Interfaces and Thin Films*, Springer International Publishing, 2014.
- [11] R. Egerton, *Physical Principles of Electron Microscopy: An Introduction to TEM, SEM, and AEM*, Springer US, 2011.
- [12] J. F. Watts, J. Wolstenholme, *An Introduction to Surface Analysis by XPS and AES*, Wiley, 2003.
- [13] R. Krause-Rehberg, H.S. Leipner, *Positron Annihilation in Semiconductors: Defect Studies*, Springer, 1999.
- [14] A. Dupasquier, A.P. Mills, S.i.d. fisica, *Positron Spectroscopy of Solids*, IOS Press, 1995.
- [15] H. Kuzmany, *Solid-State Spectroscopy: An Introduction*, Springer Berlin Heidelberg, 2009.
- [16] C.S.S.R. Kumar, *UV-VIS and Photoluminescence Spectroscopy for Nanomaterials Characterization*, Springer Berlin Heidelberg, 2013.

Chapter 3

Growth Kinetics of Ion Beam Sputtered AlN Thin Films

This chapter presents the growth kinetics of Al- and AlN-thin films in the frame work of Dynamic Scaling Theory (DST) to delineate the effect of reactive assistance of N^+/N_2^+ ions. Both the films, Al and AlN were grown on Si(100) substrates for 3, 5, 8 and 15 minutes. Their surface morphologies were recorded using AFM and analysed to determine the growth governing phenomenon that manifests at each deposition time. A theoretical background of DST is presented. A quantitative representation on the height variation and lateral correlation is provided by the 'autocovariance function $G(r)$ '. The 'power spectral density (PSD) function $g(q)$ ' is obtained to identify the growth governing phenomenological events among plastic flow, evaporation-recondensation, bulk and surface diffusion.

Most materials used in modern technological applications are composites, i.e., they have a near-surface region with properties differing from those of the bulk. This is caused by the requirement that material should exhibit a combination of various desirable properties. For example, a particular semiconductor device component may need to exhibit piezoelectricity only on the surface. This can be achieved by engineering a composite material system with piezoelectric surface and a core of device grade semiconductor. Such near-surface region can be produced by depositing a thin film onto it. Different mechanisms of depositing thin films and their properties are studied in the branch of material science, called 'thin film technology'. Today, thin films technology has been evolved as a

potential solid state material processing strategy in the field of applied physics as it caters to several stringent technological requirements [1].

3.1 Definition of Thin Film: A semantic problem

Although, there are many approaches of defining a thin film in literature, it can be defined in following ways:

(I). Physics based definition:

Thin film: Surface has a decisive influence on the internal physical properties when it meets the condition-

$$\text{Critical lengths} > \text{Deposited thickness}$$

Where, critical lengths can be taken specific to different phenomena. Thus, the same coating material of identical thickness can either be a thin film or a thick film depending upon their end-usage.

Thick film: Bulk properties of a material remain preserved when –

$$\text{Critical lengths} < \text{Deposited thickness}$$

(II). Application based definition:

Thin film: When material is deposited to exhibit surface properties, such as electron emission etc., it is called a thin film.

Thick film: When material is deposited to exhibit bulk properties, such as corrosion resistance etc., it is called a thick film.

(III). Practical definition:

Thin film: Deposited thickness $< 1\mu\text{m}$

Thick film: Deposited thickness $> 1\mu\text{m}$

3.2 Thin Film Growth Process

Generally, thin film growth process is a statistical process of nucleation, surface phenomenon (surface diffusion, evaporation-recondensation, bulk-diffusion, plastic flow) controlled growth of three dimensional nuclei, formation of a network structure and its subsequent filling to yield a continuous film. Depending on the thermodynamic parameters of thin film material and substrate surface, there are three primary modes of film growth on substrates which are shown in figure 3.1 and are described as following [2]:

(I). Volmer-Weber growth: This growth mode is also known as three-dimensional (3D) island growth. During 3D island or Volmer-Weber growth, small clusters are nucleated directly on the substrate surface. The clusters then grow into islands which in turn coalesce to form a continuous film as shown schematically in figure 3.1(A). This type of growth occurs when atoms constituting the film are strongly bound to each other rather than to the substrate. This is often the case for metal films grown on insulators or contaminated substrates.

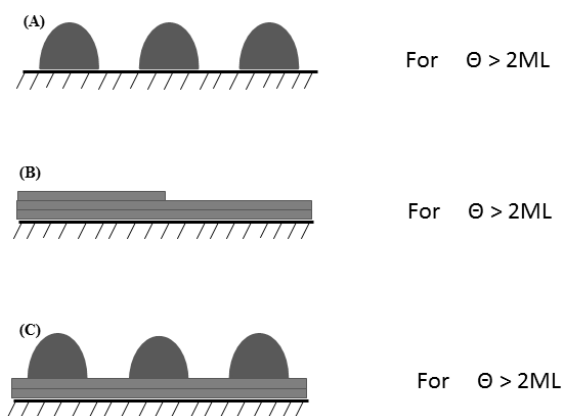


Figure 3.1 Schematic representation of three modes of thin film growth. Here Θ is the overlayer coverage in monolayer (ML).

(II). Frank-van der Merwe growth: This growth mode is also known as two-dimensional (2D) layer-by-layer growth. This mode of growth occurs when the binding between film atoms is equal to or less than that between the film atoms and the substrate which is schematically shown in figure 3.1(B). An obvious example of this type of growth is homoepitaxial growth on a clean substrate.

(III). Stranski-Krastanov growth: This growth mode is a combination of the first two growth modes already described above. In this case, after forming one or more monolayers, further layer growth becomes unfavorable and 3D islands form as shown in figure 3.1(C). The transition from 2D to 3D growth is not completely understood but can be driven in some cases by the release of elastic energy stored in the film due to film/substrate lattice mismatch. This growth mode occurs much more frequently in metal-metal and metal-semiconductor systems.

Each of the above growth modes results in topographically distinct surface. Thus, in order to grow device grade thin films with smooth surface, parameters specific to deposition technique need to be optimized carefully. It is possible from prior knowledge about kinetics of their growth specific to each deposition technique. These kinetic aspects need to be established to enable optimization of deposition process.

3.3 Growth Kinetics: Dynamic Scaling Theory (DST)

Several technological applications in the field of thin film devices require extremely smooth surfaces. In view of this, inherent roughness resulting from growth processes plays a major role. Thus, a qualitative understanding of how

growth mechanisms affect surface morphology is very useful to optimize grown structures and to predict the surface topography quantitatively.

The growth of solid surfaces via vapor phase processes can be viewed as proceeding in either of two directions: outward by physical or chemical deposition or inward by physical or chemical etching. Recent theoretical and experimental developments have shown that the fundamental molecular-scale phenomena that are involved in surface growth are common to all deposition and etching processes involving vapor-solid interactions and leave a definite signature in the morphology of the surface. Thus it becomes essential to study growth kinetics of thin films grown by physical as well as chemical vapor deposition techniques. One approach to understand the surface growth is based on concept of topographical scaling. The most familiar type of scaling is self-similarity, which itself is a restricted case of a more general class, self-affinity. Many real surfaces appear to be self-affine over a restricted range of length scales. The scaling of growing self-affine surfaces arises from the competition between the stochastic roughening and various smoothening mechanisms [3].

One way to analyze the scaling behavior for various models of growth is through the application of numerical simulations with Monte Carlo or molecular dynamics. Such analyses have yielded important insights [4-6]. However, the amount of computer time required to simulate the evolution of many features on a surface that are hundreds of atomic diameters high and thousands in width for a thin film system ($> 10^9$ atoms) is well beyond present computer technology. As such, sizes are common for actual surfaces, many investigators have developed

continuum models that represent the equation of motion of a growing surface and then analyzed the behavior of such spatially averaged equations to predict scaling exponents.

In 1985, Family and Vicsek [7] propounded DST to analyze the behavior of growing surfaces by assuming that these are self-affine. According to the conventional DST, the scaling behavior can be represented by the Family–Vicsek scaling relation [7].

$$\xi(L, t) = L^\alpha f(t/L^z) \quad (1)$$

Where

$$\xi(L, t) \sim t^\beta \quad \text{for } t/L^z \ll 1$$

and

$$\xi(L, t) \sim L^\alpha \quad \text{for } t/L^z \gg 1$$

Here, ' ξ ' is the interface width, ' L ' is the length scale over which the roughness is measured, ' t ' is the time of growth. ' α ' and ' β ' are static and dynamic scaling exponents, respectively. ' z ' equals α/β . Such a scaling behavior holds well for thin films synthesized by techniques like evaporation [8], sputtering [9], thermal chemical vapor deposition (CVD) [10] and plasma enhanced CVD (PECVD) [11].

However, the scaling behavior defined by equation (1) is not satisfied in other experimental systems [12, 13]. There is always an anomalous scaling present in every experimental system which generally causes the appearance of distinct values of the scaling exponents, α and β , which depend upon the scale of measurement [14].

3.3.1 Theoretical Background

Conventional DST considers development of self-affine surfaces to be associated with scaling relations among surface roughness (defined as root mean square (rms) of surface height $H(r)$ and denoted by ' δ '), deposition time (' t ') and scale of measurement (' L '). As mentioned earlier, DST proposes that the behavior of the interface width follows the trends propounded by Family–Vicsek relationship [7] given by equation (1). This exhibits two distinct asymptotic scaling behavior for the interface width ξ :

$$\xi(L, t) \sim t^\beta \quad \text{for } t \ll$$

$$\text{and } \xi(L, t) \sim L^\alpha \quad \text{for } t \gg$$

Therefore, during initial growth stages, the interface width increases with deposition time ' t ' at a rate of the growth exponent β until a saturation value of ' ξ_L ' is reached. After attaining this value, the interface width becomes a function of scale of measurement ' L ' through the growth exponent ' α '. At some critical length ' L_C ', the interface width saturates and becomes equal to rms value of roughness ' δ ' for all values of $L > L_C$.

A quantitative representation of the height variation and lateral correlation is provided by the “autocovariance function $G(|r|)$ ” [15]. $G(|r|)$ at different length scales provides a quantitative description of correlation among heights at different points on a surface as a function of their separation ' r '. The interface width as a function of length scale is related to this autocorrelation function in the following way [16, 17]:

$$\xi_L^2 = \left(\frac{1}{L^2}\right) \int_0^L [\delta^2 - G(|r|)] r dr \quad (2)$$

The autocorrelation function for a self-affine surface with spatial scaling exponent ' α ' can be approximated as:

$$G(|r|) \approx \begin{cases} \delta^2 \left[1 - \frac{\alpha+1}{2} \left(\frac{r}{L_c} \right)^2 \right], & \text{for } r \leq L_c \\ 0, & \text{for } r > L_c \end{cases} \quad (3)$$

The Fourier transform of the equation (3) yields power spectral density function (PSD), $g(|q|)$. This is a very useful function as several fundamental aspects of a rough surface can be formulated in terms of PSD. Mathematically PSD is linked to autocovariance function as mentioned below.

$$g(|q|) = \mathcal{F}[G(|r|)]$$

where \mathcal{F} is the two-dimensional Fourier transform operator. The

PSD assumes the forms:

$$g(|q|) \approx \begin{cases} \frac{\alpha}{\pi} \delta^2 L_c^2 & \text{for } |q| < 1/L_c \\ \frac{\alpha}{\pi} \frac{\delta^2}{L_c^{2\alpha}} q^{-2(\alpha+d)} & \text{for } |q| \geq 1/L_c \end{cases} \quad (4)$$

where d , in our case, represents line scan direction and equals to '1'.

Thin film growth via a surface-vapor interaction takes place by the stochastic addition or removal of adatoms with no lateral transport occurring on the surface. Scaling of the growing self-affine surface arises from the competition between roughening and smoothening mechanisms. By combining the smoothening mechanisms with the stochastic roughening, a kinetic rate expression can be written in reciprocal space to account for the surface growth [18]:

$$\frac{\partial h(|q|, t)}{\partial t} \propto -c_n |q|^n h(q, t) + \dot{h}(|q|, t) \quad (n = 1, 2, 3, 4) \quad (5)$$

Here $h(|q|, t)$ represents the radial average of the Fourier transformed surface height denoted by $H(|r|, t)$. First term on the right hand side represents the smoothening mechanism described by Herring et al. [19]. The second term is the stochastic noise term in reciprocal space that describes random arrival of the depositing species. The solution to equation (5) is obtained as radially averaged power spectral density [18]:

$$g(|q|, t) = \langle h(|q|, t)^2 \rangle = \Omega \frac{1 - \exp(-2c_n |q|^n t)}{c_n |q|^n} \quad (6)$$

In this equation ' Ω ' is proportional to flux, ' t ' is the deposition time, and ' c_n ' is a constant which characterizes the specific lateral mass transport mechanism indicated by ' n '.

We have used a fitting function similar to equation (6) to model our data in the manner similar to one used by William M. Tong et.al. [20]. This is expressed as:

$$g(|q|, t) \propto \Omega \frac{\exp(2\Sigma\chi_n |q|^n t) - 1}{\Sigma\chi_n |q|^n} \quad (7)$$

Where the q -coefficients χ_n are simply fitting parameters and n takes the values 1, 2, 3 & 4.

The q -coefficients are allowed to acquire either positive or negative values which will determine whether the process will be smoothening or roughening one. According to Herring [19], four smoothening mechanisms are plastic flow ($n = 1$), evaporation-recondensation ($n = 2$), bulk diffusion ($n = 3$) and surface diffusion ($n = 4$).

3.4 Growth Kinetics of Aluminum (Al) Thin Films by DST

To develop a general understanding of the fundamental processes controlling the growth of the Al-thin film by ion beam sputter deposition system (IBSD), its growth kinetics can be studied in the frame work of DST. Al-thin film is a promising candidate for microelectronic device fabrication due to its low resistivity and high compatibility with silicon. For this, we have determined the scaling exponents of Al-thin films deposited on Si(100) by IBSD. The purpose of this study is to understand the growth kinetics of IBSD grown Al-thin films as a function of deposition time and scale of measurement.

3.4.1 Aluminum (Al) - Thin Film Deposition

Thin films analyzed in this study were grown by IBSD on Si (100) substrates for different time durations. The deposition system and their working principle have already been explained in chapter-2. Prior to deposition, substrates were cleaned by RCA-1 process [21]. The base pressure better than 4×10^{-6} mbar has been routinely achieved in the deposition chamber. Deposition was carried out at room temperature at working pressure at 2×10^{-4} mbar. Thin films were grown for 3, 5, 8 and 15 minutes. During deposition, the metal atom flux was supplied by sputtering Al target with an inert ion beam of Ar⁺ ions having an energy of 500 eV.

The surface morphology was analyzed using an atomic force microscope (AFM) (Ntegra Prima of M/s NT-MDT, Russia) in semi-contact mode. A Si-tip with a radius of 35 nm was used to scan $1 \times 1 \mu\text{m}^2$ area over the film surface. Roughness of the film was calculated as root mean square of the surface heights acquired at different points on the surface. In order to improve the statistics and

representivity, images and roughness line profiles were acquired at several places on the specimen surface.

The static scaling exponent ' α ' was calculated by plotting the logarithm of interfacial width (ζ) against logarithm of scan length (L) for each Al- thin film. The dynamic scaling exponent ' β ' was obtained from the slope of the curve generated by a log-log plot of rms surface roughness (δ) vs. deposition time (t). Scaling properties of the films were further studied using an autocorrelation function ($G(|r|)$) and power spectral density PSD expressed as $g(q)$ to obtain information about different roughening and smoothening phenomena occurring on the film surface. $G(|r|)$ and $g(|q|)$ curves were obtained for different films grown for different deposition times using the procedure described earlier. Distinctly different trends were observed for films deposited over different deposition durations.

3.4.2 Observations and Discussion

In figure 3.2, the evolution of surface morphology is shown for the films grown over different deposition times of 3, 5, 8 and 15 minutes. It is inferred from the figure 3.2(A) that small nuclei are nucleated at the substrate surface after a deposition time of 3 minutes. This signals onset of thermal equilibrium between deposited species and substrate surface. As the deposition time increases, these tiny nuclei grow in number as well as in size forming bigger clusters as shown in figure 3.2(B). In the figure 3.2(C), a discontinuous morphology of the film is observed due to coalescence of the bigger clusters. Such cluster coalescence is a consequence of reduction in surface area which leads to full coverage of the

substrate surface that leaves behind very few uncovered channels. With further increase in deposition time, secondary nucleation takes place on uncovered channels eventually forming a continuous film as shown in figure 3.2(D).

This can also be appreciated well from the figure 3.3 where the representative line profiles along the respective images are presented. In these films, grown over different deposition times, there are two length scales: the first one is characterized by the height fluctuations among different nuclei, clusters or islands and the second one is defined by small aggregates of these nuclei and clusters. It is possible to observe initial stages of the development of surface topography from figure 3.3(A) in the form of tiny nuclei. These nuclei exhibit peaks constituted of small

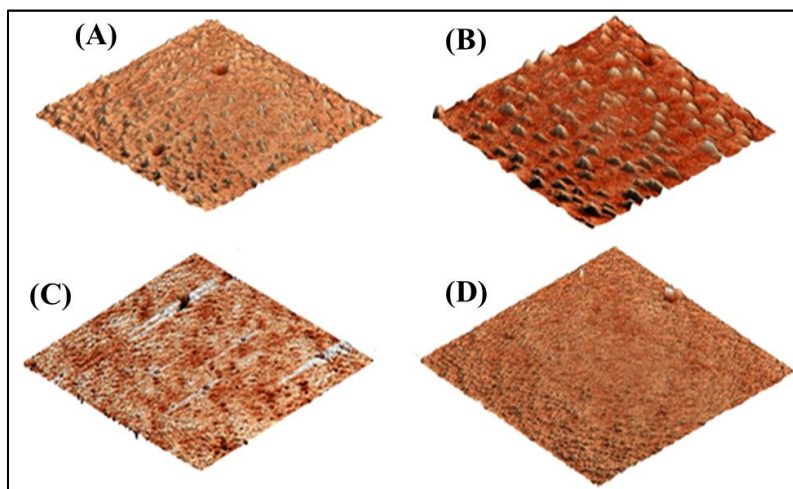


Figure 3.2 Representative 3D AFM images ($1 \times 1 \mu\text{m}^2$) of the evolution of surface morphology for the films grown for different deposition time as, (A) 3 minutes, (B) 5 minutes, (C) 8 minutes and (D) 15 minutes.

height amplitudes. As the deposition time is increased, the amplitude of height oscillations and corresponding spatial coverage increase as can be inferred from comparatively larger and broader peaks in the line profile of figure 3.3(B). Line profiles in figure 3.3(A) and 3.3(B) together support the fact that the small nuclei

nucleated at early deposition stages grow with time to form larger clusters. These clusters then agglomerate to form islands as is shown by line profile in figure 3.3(C). This figure shows large spatial coverages concomitant with large height oscillations. This phenomenon leads to deposition over larger area of substrate surface with few channels left out to be filled by secondary nucleation process.

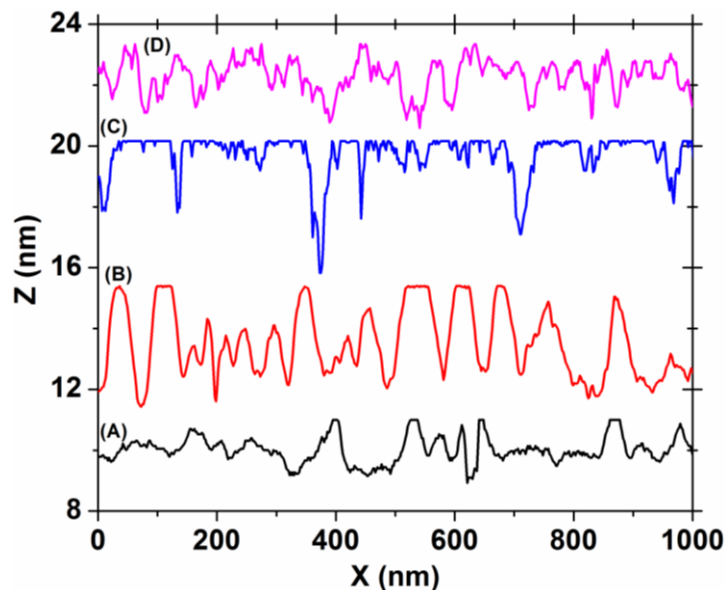


Figure 3.3 Representative line profiles across the sample surface for different deposition time: (A) 3 minutes, (B) 5 minutes, (C) 8 minutes, (D) 15 minutes.

Finally, in figure 3.3(D), the appearance of smaller and rarely equal height amplitudes are seen. The complete spatial coverage of substrate surface following above hierarchy of events is indicative of deposition of a smooth continuous film.

An important fact is observed while calculating the static scaling exponent or roughness exponent ' α '. According to dynamic scaling theory as introduced briefly in Sec. 3.3.1, the roughness exponent can be calculated by plotting $\log(\zeta)$ vs. $\log(L)$ as shown in figure 3.4. At small length scales, ζ increases with length scale and becomes saturated (ζ_L) after a certain critical length L_C . This saturated

value of ξ_L is equal to the rms roughness ' δ ' of the surface under investigation. Figure 3.4(A) shows that an $\alpha = 0.61$ governs the evolution of surface roughness until a saturated value of rms surface roughness, $\delta = 0.269$ nm, is achieved at a critical length $L_C = 631$ nm, for a 3 minutes deposition. As the deposition time increases, α -values begin to decrease with smaller critical lengths and ' δ ' increases to 0.550 nm for 8 minutes deposition until film achieves larger surface coverage on the substrate barring few uncovered channels. Once the film becomes continuous and smooth after a deposition of 15 minutes, α becomes lowest with a value of 0.38 concomitant with low ' δ ' value that equals 0.398 nm. This is shown in figure 3.4(B-D) respectively.

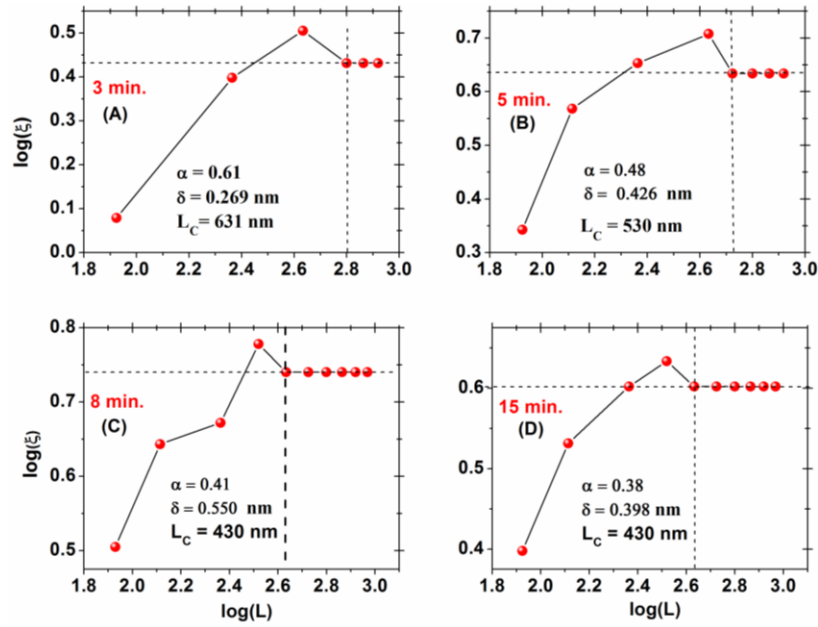


Figure 3.4 Plot of the interface width of the substrate surface as a function of length scale for several different deposition time varied as (A) 3 minutes (B) 5 minutes (C) 8 minutes and (D) 15 minutes.

Corresponding values of α , L_c , and δ are listed in table 3.1. These α -values, shown in figure 3.5, match with those obtained from the slope of the linear region of PSD plot depicted in figure 3.9.

Table 3.1 Comparison of α , L_c and δ for different deposition times of Al-thin films.

Deposition Time 't' (in min.)	α	L_c (nm)	δ (nm)
3	0.61	631	0.269
5	0.48	530	0.426
8	0.41	430	0.550
15	0.38	430	0.398

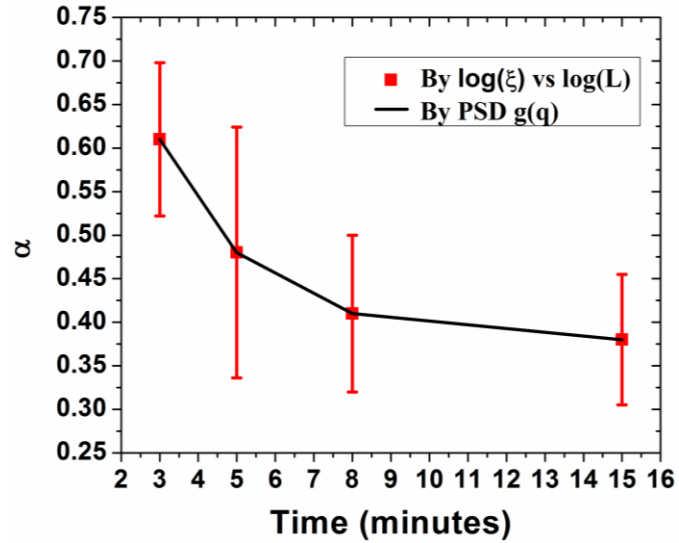


Figure 3.5 Comparison of α -exponents obtained from two different techniques for different deposition times.

The dynamic scaling exponent ' β ' acquires two different values as shown in figure 3.6. This behaviour of ' β ' suggests that the growth process spans over two

regimes. One before full coverage of the substrate surface governed by $\beta_1 = 0.73$ and other after full coverage of substrate which is governed by $\beta_2 = -0.52$.

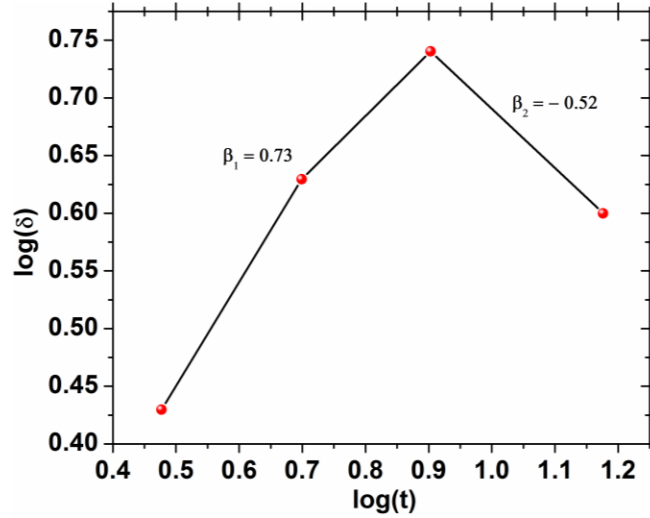


Figure 3.6 Dynamic scaling constant ' β ' governing the growth for different deposition times with different slopes.

Figure 3.7 presents further information about both height variation and lateral correlation predicted from autocovariance function $G(|r|)$ on all the films. It provides information on height correlation across lateral direction. Fourier transform of $G(|r|)$, given by equation(3), provides the function $g(|q|)$ or PSD which is shown in figure 3.8. When this $g(q)$ is fitted to equation (7), it identifies the growth governing phenomena from material related events like plastic flow, evaporation-condensation, bulk and surface diffusions. Either one or more than one phenomenon may dominate a particular film growth process under a given deposition condition.

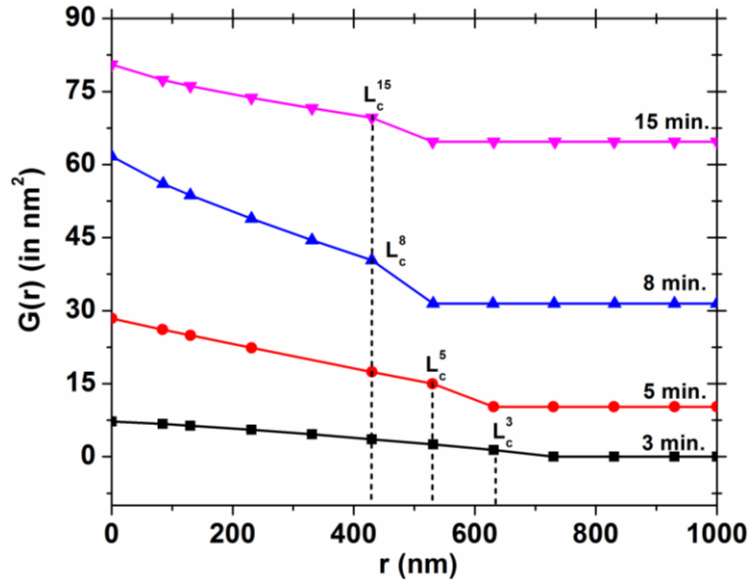


Figure 3.7 Autocovariance function for different deposition times depicting how heights are co-related at different points across lateral direction.

Generally during the course of thin film deposition, adsorbed species are not in thermal equilibrium with the substrate initially and interact among themselves as well as with the substrate surface to achieve equilibrium [22]. Few such common phenomena being investigated in this study are plastic flow, evaporation-recondensation, bulk and surface diffusions. Different extents of these processes act together during the growth of a thin film. These phenomena are represented by $n = 1, 2, 3, 4$ respectively in equation (7). Figure 3.8 shows the result of fitting of experimental $g(|q|)$ for different deposition times with equation (7). It can easily be seen that this fitting function captures many of the important features of the experimental $g(|q|)$ or PSD functions. The sign of the parameters ξ_n , shown in table 3.2, decides whether the corresponding smoothing or roughening mechanism will be dominant.

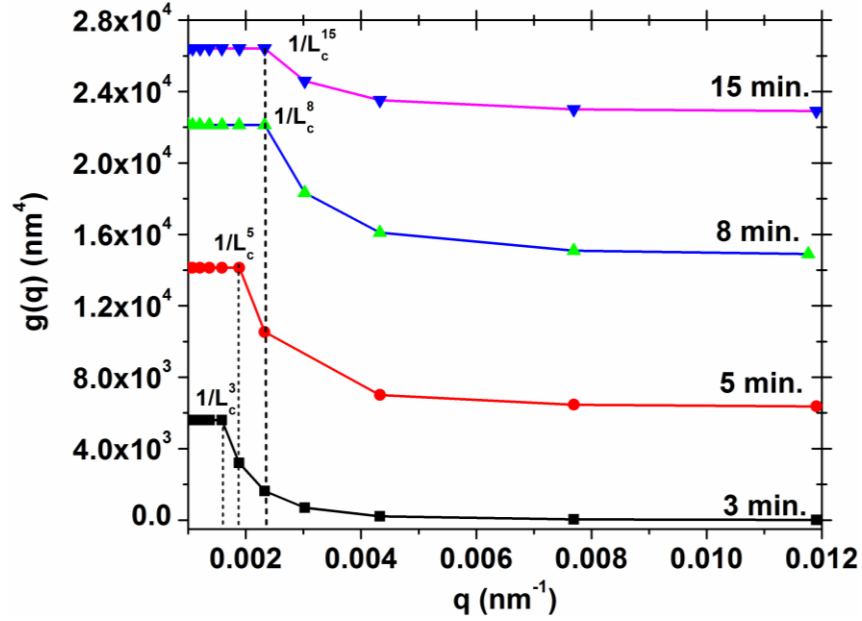


Figure 3.8 Spectral power density and critical lengths obtained corresponding to different deposition time.

Although, all the fits are not consistent but fits for $t = 8$ minutes and $t = 15$ minutes follow the same set of growth mechanisms. For films grown for 3 minutes, primary roughening process is related to $n = 2$ and $n = 4$ where surface diffusion ($n=4$) prevails as roughening phenomenon. In the case of smoothening phenomenon bulk diffusion corresponding to $n = 3$ plays a major role along with plastic flow of surface as shown in figure 3.9(A). Figure 3.9(B) shows that as the deposition time is increased to 5 minutes, bulk diffusion corresponding to $n = 3$ becomes the leading roughening mechanism while surface diffusion with $n = 4$ smoothenes the surface voluntarily.

Table 3.2 Comparison of fits of equation (7) for different deposition times.

Samples	Ω ($\times 10^3$)	t (min.)	ξ_1 ($\times 10^3$)	ξ_2 ($\times 10^6$)	ξ_3 (10^8)	ξ_4 ($\times 10^{10}$)
A	3.069	3	-2.171	2.552	-9.798	5.642
B	2.223	5	-0.188	-0.462	5.366	-14.802
C	2.172	8	-0.609	0.389	-0.684	-0.469
D	10.080	15	-0.608	4.121	-8.753	-0.518

Thus, the vapor atoms reaching on the surface diffuse over it and interact among themselves to form clusters (as shown in figure 3.2(B)). As the deposition time increases further to 8 minutes, surface coverage increases by plastic flow ($n=1$), bulk diffusion ($n=3$) and surface diffusion ($n=4$). While $n = 2$ corresponds to mechanism governed by evaporation and recondensation process to bring about roughening. Thus, the film covers a larger area on the substrate surface with few uncovered channels and holes being left out. This is indicated in figure 3.9(C). For a 15 minutes deposition schedule, shown in figure 3.9(D), the film becomes continuous with a lower surface roughness. In this case, bulk diffusion behaviour corresponding to $n = 3$ plays a dominant role in smoothening of the film surface

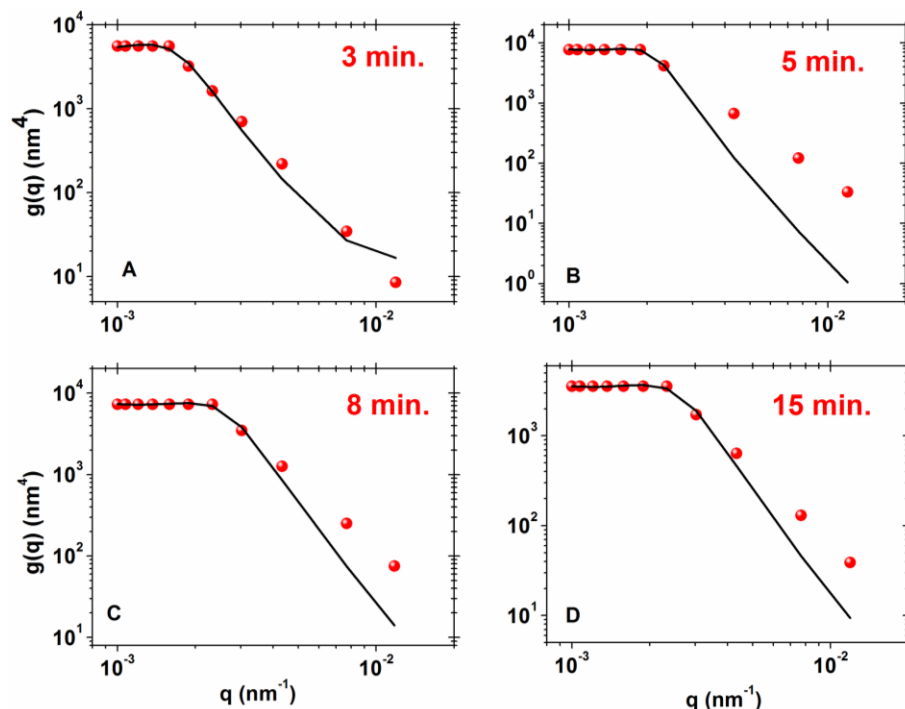


Figure 3.9 Fitting of experimentally obtained $g(q)$ with equation (7) for different deposition times indicating towards dominating roughening/smoothing phenomena. The data are presented as log–log plots where (A) 3 minutes, (B) 5 minutes, (C) 8 minutes and (D) 15 minutes.

by filling up of all the valleys and irregularities present on the surface. Here, both plastic flow and surface diffusion contribute very little. Once again evaporation and recondensation become major roughening mechanisms. Present investigations, however, do not rule out existence of additional mechanisms responsible for smoothing and roughening.

3.5 Growth Kinetics of Aluminum Nitride (AlN) Thin Films by DST

The changes in morphological features and prevalence of certain surface phenomena at different stages of AlN thin film growth aided by reactive assistance of N^+ and N_2^+ ions are deliberated in this section. Such a growth scenario often results in a process condition which is far from equilibrium. Growth governing static and dynamic scaling exponents were determined by

similar calculations already employed in case of Al thin film growth without ion assistance [11]. DST formalism has been used to unravel the governing phenomena behind ion assisted thin film growth.

3.5.1 AlN - Thin Film Deposition

AlN-thin films for present study were grown by IBSD in reactive assistive mode on Si (100) substrate. Prior to deposition, Si (100) substrates were cleaned using RCA-1 process [21]. Deposition of AlN-thin films was carried out after achieving a base pressure better than 4×10^{-6} mbar. Working pressure of the chamber was maintained at 2×10^{-4} mbar while substrate temperature was kept constant at 500°C . Films were grown for 3, 5, 8 and 15 minutes of time duration. During deposition, the metal atom flux was provided by sputtering Al target with Ar^{+} ion beam having an energy of 500 eV. Reactively assistive flux of N^{+} and N_2^{+} ions were supplied directly to the substrate surface from the end-Hall ion source operated at an energy of 100 eV.

Surface morphology of deposited films was analyzed using an Atomic Force Microscope (AFM) (NT-MDT, Russia). Topographic images were obtained in semi-contact mode using a commercial Si-tip cantilever with a tip radius of 35 nm. For better statistics, topographic images and corresponding line profiles were obtained from several $1 \times 1 \mu\text{m}^2$ scan areas at different spatial locations spread over the 10 mm x 10 mm film surface. Root mean square of surface heights at these different locations were considered as roughness value of the film.

3.5.2 Observations and Discussion

Figure 3.10 shows atomic force micrographs of AlN thin films grown for different time durations along with the representative line profiles acquired across the film surface. Height fluctuations and lateral aggregation among these cone shaped nuclei and clusters are two pragmatic parameters through which surface growth occurring over each deposition time is investigated. The distinct changes in the morphological features of these images clearly show the influence of low energy ion-surface interaction. The ions impinging on the surface modifies microstructure of the film surface at different growth stages. Figure 3.10(A) shows small and isolated cone shaped nucleation on the substrate surface for a deposition of 3 minutes. Onset of ion-induced densification is clearly observed by a pronounced increase in number density of nuclei in the course of reactive assistance by N^+ and N_2^+ ions as compared to the case in which no ion assistance was provided (Figure 3.2). Ion irradiation during nucleation removes over hanging atoms and creates defects in the substrate surface. These defects, which mostly include vacancies and voids, act as preferred adsorption sites. These adsorption sites trap or implant incident species in the near surface region and give rise to several tiny nuclei [23, 24]. These tiny nuclei appear with well separated peaks having small height amplitude and spatial coverage on the line profile across the substrate surface. With increase in deposition time to 5 minutes, it can be seen from figure 3.10(B) that the nuclei grew more rapidly in number than in size. Thus, a pronounced increase in peak number density appears as compared to their spatial coverage. Further, reactive ion impact with N^+/N_2^+ ions

sets up collision cascades on the substrate surface due to which adatom diffusion gets enhanced. Simultaneously, penetration of ions to a depth of few interatomic spacings causes near surface vacancies to be partially filled by the newly arriving adatoms. This mechanism provides a downward packing of the material resulting in the formation of a dense film [25]. This observation is also corroborated by a significant increase in height amplitude and spatial coverage of peaks along with the appearance of few infant peaks in its line profile. This is shown in figure 3.10(C) for a deposition time of 8 minutes.

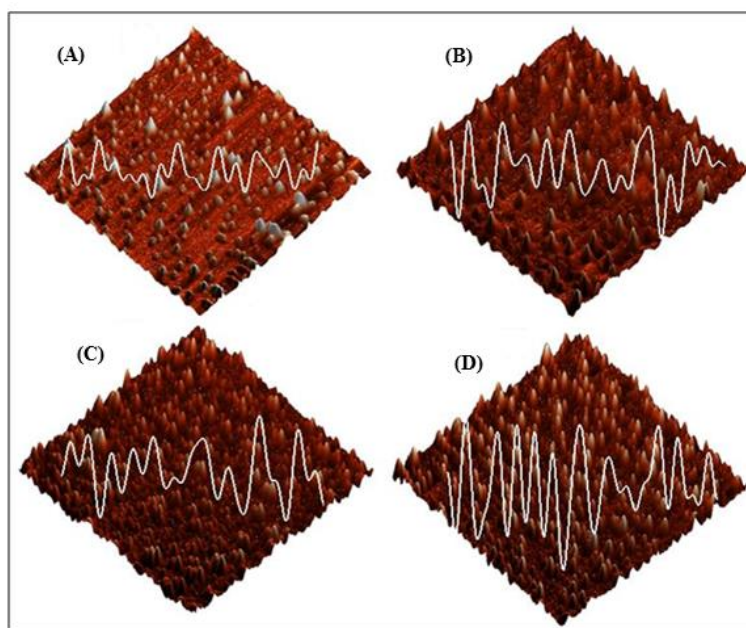


Figure 3.10 Representative 3D atomic force microscope images ($1 \times 1 \mu\text{m}^2$) along with line profiles across the sample surface displaying the evolution of surface morphology for the films grown for different deposition time as, (A) 3 minutes, (B) 5 minutes, (C) 8 minutes and (D) 15 minutes.

As the deposition time is increased to 15 minutes, ion-irradiation induced dissociation of small clusters takes place. As these small clusters are further reduced in size, they become more mobile on the surface and diffuse to coalesce with larger stable clusters. Moreover, clusters which reduce to subcritical size

become energetically unstable and spontaneously dissociate to form adatoms. Few of these adatoms desorb and remaining diffuse to larger clusters and/or to fill voids. As a consequence of occurrence of all aforementioned phenomena, ion-irradiation induced surface diffusion and collapse of vacancies/voids together form a densely packed AlN thin film with full substrate coverage [24]. The peaks appearing in the corresponding line profile are found to be ironed out as shown in figure 3.10(D). These observations on the changing surface morphology indicate that surface diffusion along with collapse of voids and occupation of near surface vacancies play a major role in the evolution of observed surface microstructure. These experimental observations were further analysed by DST to extract the growth exponents described in section 1 and to identify the corresponding growth governing phenomena.

The static scaling exponent (α) for AlN thin films is shown in figure 3.11 for each deposition time. It is observed from the graphs that ζ increases with increase in the length scale L and after a certain critical length L_C , ζ gets saturated. This saturated value ζ_L , represents the rms roughness ' δ ' of the surface under investigation. In the early stages of film growth, $\alpha = 0.62$ governs the evolution of surface roughness up to a critical length of $L_c = 600$ nm and after that a saturated value of rms surface roughness $\delta = 1.99$ nm is achieved. This is shown in figure 3.11(A) for a deposition duration of 3 minutes where nucleation is initiated. As the deposition time is increased to 5 minutes, α decreases to 0.46 and preserves the same L_C value. This can be attributed to the stochastic annihilation of near surface vacancies and collapse of voids with almost no lateral transport on the

surface. Consequently, ξ decreases with a diminutive increase in δ by 0.16 nm. This is shown in figure 3.11(B). Plot in figure 3.11(C) displays that for longer deposition time of 8 minutes, collision cascade induced enhanced surface diffusion and monolayer penetration of irradiated reactive assistive ions become responsible for further diminution of ξ with an associated reduction of α to a value of 0.36. At the same time, L_c also reduces to 550 nm indicating a faster surface coverage and value of δ becomes 3 nm with a modest increase of 0.85 nm.

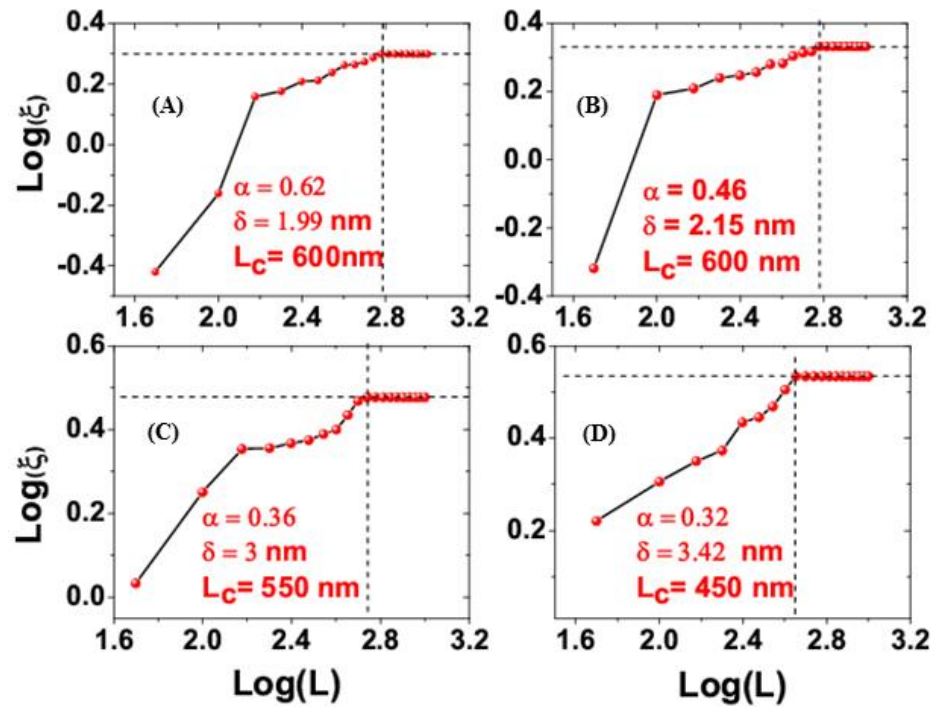


Figure 3.11 Log-Log plots of interface width (ξ) vs. length scale (L) for different growth time varied as (A) 3 minutes (B) 5 minutes (C) 8 minutes and (D) 15 minutes.

When deposition time is further increased to 15 minutes, still smaller value of $\alpha = 0.32$ manifests with a reduction of L_c value to 450 nm. This implies that ξ reduces further with a swift coverage of full substrate surface. In this case, highly mobile adatoms generated by ion-induced cluster dissociation diffuse to feed

larger stable clusters and contribute to roughen the surface. Concurrently, a fraction of them occupies near surface defects to smoothen it. The prevailing competition between these roughening and smoothening phenomena yields in a small rise of δ value to 3.42 nm. This is shown in figure 3.11(D). Table 3.3 lists the values of α , δ and L_c corresponding to each deposition time. Figure 3.12 shows that how static scaling exponent ' α ' decreases with increasing deposition time along with an inset displaying the dynamic scaling exponent (β). The value of $\beta = 0.36$ was calculated from the slope of $\log(\delta)$ vs. $\log(t)$ curve.

Table 3.3 Comparison of static scaling exponent (α), critical length (L_c) and rms roughness (δ) of AlN-thin films.

t (min.)	α	L_c (nm)	δ (nm)
3	0.62	600	1.99
5	0.46	600	2.15
8	0.36	550	3.0
15	0.32	450	3.42

This small value of ' β ' stipulates that although ' δ ' increases with increase in deposition time, the relative changes among these ' δ ' values are rather small. Thus, growth seems to be more organized and systematically contributed from different surface phenomena as propounded by DST.

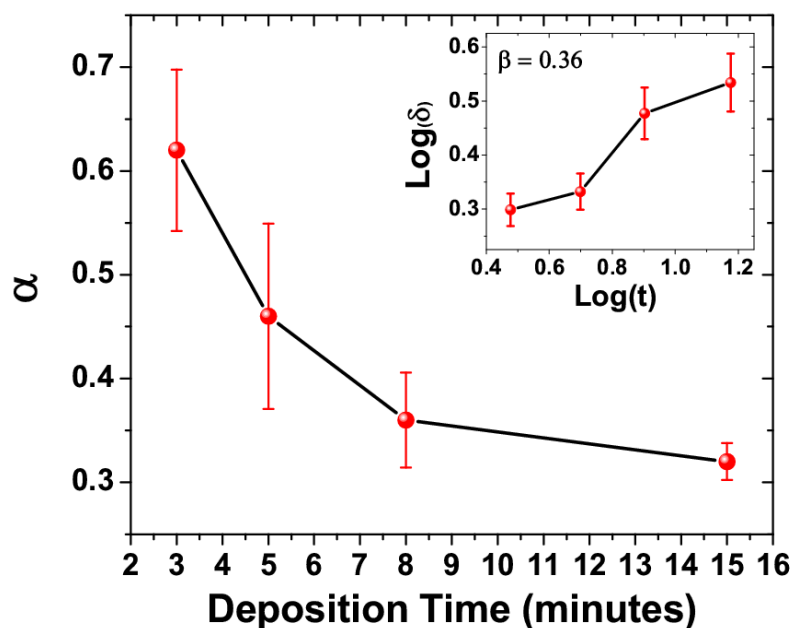


Figure 3.12 Variation of static scaling exponent ' α ' with deposition time. Dynamic scaling exponent ' β ' is extracted from the slope of $\text{Log}(\delta)$ vs. $\text{Log}(t)$ curve shown in the inset.

The autocovariance function $G(|r|) = \langle H(r)H(r'-r) \rangle$ was used to extract the information about how heights at different points on the surface are changing together as a function of $|r|$. This is illustrated in figure 3.13. Power spectral density (PSD) $g(q)$ of the surface as shown in figure 3.14. This was computed by taking Fourier transform of $G(|r|)$ as described in section 3.3.1. This provides a rather comprehensive description of the film roughness and allows us to calculate various statistical parameters characterizing the underlying growth process.

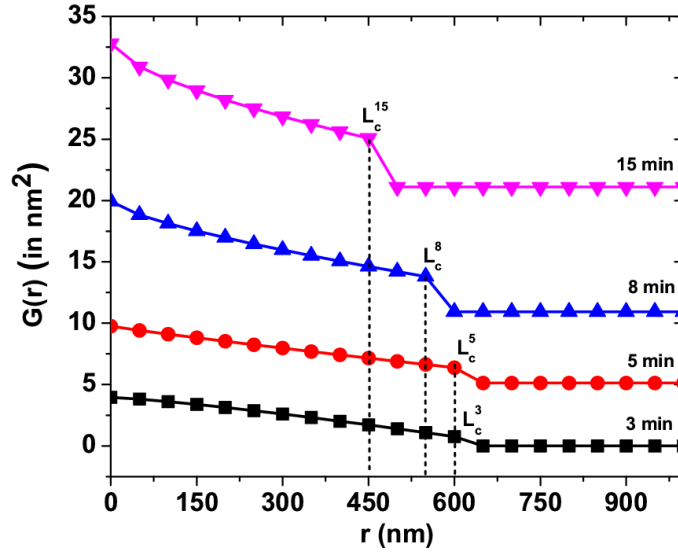


Figure 3.13 Autocovariance function for different deposition times depicting how heights are co-related at different points across lateral direction.

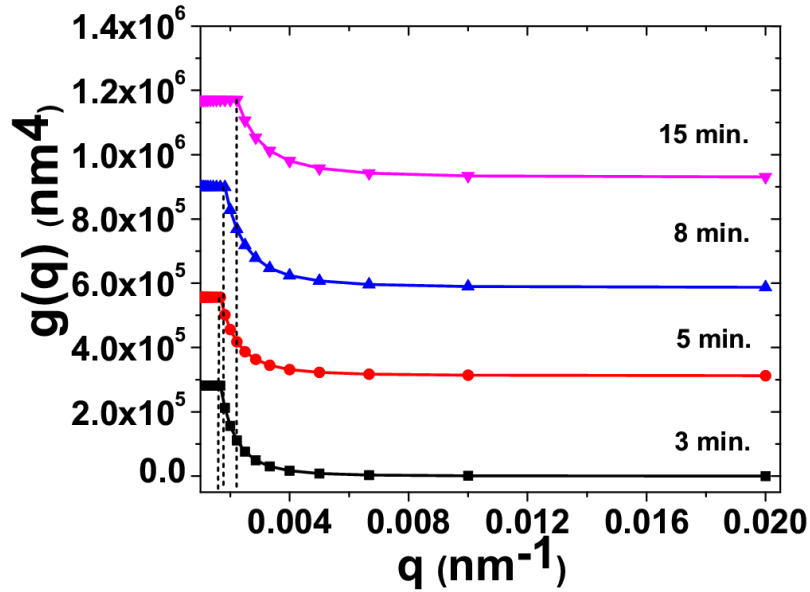


Figure 3.14 Power spectral density $g(q)$ obtained for thin films deposited for different deposition time.

Figure 3.15 shows the fitting of equation (7) with $g(q)$ obtained from experimental data in equation (4). Sign and magnitude of the parameters χ_n listed

in table 3.4, decide whether a phenomenon corresponding to a particular n-value will dominate as smoothening or a roughening one.

Table 3.4 Comparison of fitting parameters obtained by fitting power spectral density $g(q)$ with equation (4) for different deposition times.

t (min.)	Ω (X 10^5)	χ_1 (X 10^3)	χ_2 (X 10^6)	χ_3 (X 10^8)	χ_4 (X 10^{10})
3	1.6	-1.9	2.1	-7.6	3.1
5	1.5	-2.2	2.6	-10.3	9.2
8	2.1	-2.1	2.2	-8.1	7.0
15	1.8	-1.8	1.5	-4.6	3.3

The consistent fits for all four data sets in figure 3.15 indicate that the phenomena corresponding to $n = 2$ and 4 are primary roughening processes which represent evaporation-recondensation and surface diffusion, respectively.

Among these two roughening phenomena, surface diffusion which acquires more positive χ -value dominates to roughen the surface. As far as smoothening is concerned, $n = 1$ and 3 represent plastic flow and bulk diffusion, respectively, constituting the primary contributions. However, bulk diffusion of adatoms with more negative χ -value leads the smoothening of the surface by filling up near surface defects. In essence, all these aspects contribute to the evolution of surface morphology, with a varying weightage in their relative influence on growth phenomena.

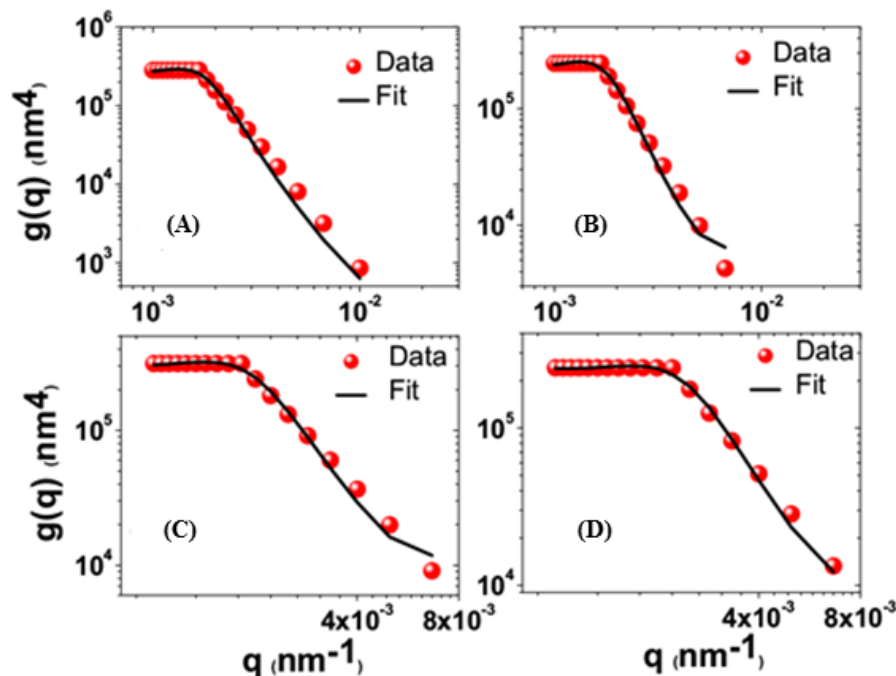


Figure 3.15 Fitting of experimentally obtained power spectral density $g(q)$ with equation (7) for different deposition time, (A) 3 minutes, (B) 5 minutes, (C) 8 minutes and (D) 15 minutes.

3.6 Conclusion

In principle, the entire spatial and temporal dependence of a surface can be summarized by the static and dynamic scaling exponents (α , β), the material-dependent surface rms height, and the critical length for scaling [$\delta(\tau)$, $L_c(\tau)$] measured at particular time (τ). For Al-thin films, the static scaling exponent ' α ' decreases as the deposition time increases. Consequently, the interfacial width becomes smaller which is associated with smaller critical lengths (L_c). ' δ ' increases with deposition time until film achieves maximum coverage on the substrate surface and once the film becomes continuous, ' δ ' achieves a lower value and film subsequently becomes smoother. The dynamic scaling exponent ' β ' does not achieve a universal value. In case of Al-thin films, the fundamental

mechanisms leading to the growth of surface morphologies are different for different deposition time. For a 3 minutes deposition, surface gets rougher by evaporation and recondensation of the vapor atoms reaching on the surface along with substantial diffusion across lateral directions resulting in the formation of small nuclei. After 5 minutes deposition under the same conditions, 3D-clusters of adatoms due to the dominance of surface diffusion are formed. Then for an 8 minutes deposition, bulk diffusion dominates to fill the valleys and other remnant irregularities on the surface and covers a larger area on the substrate surface. Both plastic flow and bulk diffusion act as principle smoothening phenomena. For longer deposition times of 15 minutes, same set of smoothening phenomena operates to achieve a continuous film with no uncovered channels.

In case of AlN thin films grown with reactive IBAD technique, growth is found to be more systematic. It is observed that dynamic scaling exponent $\beta = 0.36$ governs the growth of AlN thin films from small nuclei to a continuous one. Films grown for 3 minutes and 5 minutes exhibit sporadic nucleation and small cone shaped clusters, respectively, with same critical length L_C associated with a decrease in static scaling exponent ' α '. For the deposition of small nuclei of 1.99 nm and clusters of 2.15 nm rms height, $\alpha = 0.62$ and 0.46 respectively, should be maintained along with the same value of ' β '. A continuous film with full substrate coverage was obtained for $\alpha = 0.32$ with rms roughness value of 3.42 nm. As deposition time increases, the decrease in ' L_C ' suggests rapid surface coverage with a slight increase in their respective rms roughness (δ_s). Large positive value of χ_4 , obtained by DST, confirms surface diffusion as the major roughening

phenomena. At the same time, a considerable negative value of χ_3 indicates that bulk diffusion leads the smoothening of the film surface. These control parameters extracted from the DST analysis make it feasible to tune the deposition parameters to realize the growth of desired device quality thin films.

References

- [1] K. Seshan, Handbook of Thin Film Deposition Processes and Techniques, Elsevier Science, 2001.
- [2] K.L. Chopra, Thin film phenomena, McGraw-Hill, 1985.
- [3] J.C. Russ, Fractal Surfaces, Springer US, 2013.
- [4] D. Fritter, C.M. Knobler, D.A. Beysens, Experiments and simulation of the growth of droplets on a surface (breath figures), Physical Review A, 43 (1991) 2858-2869.
- [5] T. Vicsek, Fractal Growth Phenomena, World Scientific, 1992.
- [6] B.M. Forrest, L.-H. Tang, Surface roughening in a hypercube-stacking model, Physical Review Letters, 64 (1990) 1405-1408.
- [7] V. F. Family, T., Journal of Physics A 18 (1985) 75-79.
- [8] S.G. Mayr, Moske, M., Samwer, K. , Identification of key parameters by comparing experimental and simulated growth of vapor-deposited amorphous Zr₆₅Al_{17.5}Cu_{17.5} films, Physical Review B, 60 (1999) 16950.
- [9] F. Elsholz, E. Schöll, A. Rosenfeld, Control of surface roughness in amorphous thin-film growth, Applied Physics Letters, 84 (2004) 4167-4169.

- [10] F. Ojeda, R. Cuerno, R. Salvarezza, L. Vázquez, Dynamics of Rough Interfaces in Chemical Vapor Deposition: Experiments and a Model for Silica Films, *Physical Review Letters*, 84 (2000) 3125-3128.
- [11] G.T. Dalakos, J.P. Plawsky, P.D. Persans, Topographic evolution during deposition of plasma-deposited hydrogenated silicon on glass, *Physical Review B*, 72 (2005) 205305.
- [12] A.E. Lita, J.E. Sanchez, Jr., Effects of grain growth on dynamic surface scaling during the deposition of Al polycrystalline thin films, *Physical Review B*, 61 (2000) 7692-7699.
- [13] N.M. Hasan, J.J. Mallett, S.G. dos Santos Filho, A.A. Pasa, W. Schwarzacher, Dynamic scaling of the surface roughness of Cu deposited using a chemical bath, *Physical Review B*, 67 (2003) 081401.
- [14] J.M. López, M.A. Rodríguez, R. Cuerno, Superroughening versus intrinsic anomalous scaling of surfaces, *Physical Review E*, 56 (1997) 3993-3998.
- [15] E.A. Eklund, E.J. Snyder, R.S. Williams, Correlation from randomness: quantitative analysis of ion-etched graphite surfaces using the scanning tunneling microscope, *Surface Science*, 285 (1993) 157-180.
- [16] M.V. Berry, The Statistical Properties of Echoes Diffracted from Rough Surfaces, *Philosophical Transactions of the Royal Society of London. Series A, Mathematical and Physical Sciences*, 273 (1973) 611-654.
- [17] H. You, R.P. Chiarello, H.K. Kim, K.G. Vandervoort, X-ray reflectivity and scanning-tunneling-microscope study of kinetic roughening of sputter-

- deposited gold films during growth, *Physical Review Letters*, 70 (1993) 2900-2903.
- [18] S.F. Edwards, D.R. Wilkinson, The Surface Statistics of a Granular Aggregate, *Proceedings of the Royal Society of London. A. Mathematical and Physical Sciences*, 381 (1982) 17-31.
- [19] C. Herring, Effect of Change of Scale on Sintering Phenomena, *Journal of Applied Physics*, 21 (1950) 301-303.
- [20] W.M. Tong, R.S. Williams, Kinetics of Surface Growth: Phenomenology, Scaling, and Mechanisms of Smoothing and Roughening, *Annual Review of Physical Chemistry*, 45 (1994) 401-438.
- [21] W. Kern, The Evolution of Silicon Wafer Cleaning Technology, *Journal of The Electrochemical Society*, 137 (1990) 1887-1892.
- [22] Bunshah, *Deposition Technologies for Films and Coatings: Science, Technology and Applications*, Noyes publications, 1994.
- [23] S. Mohan, M.G. Krishna, A review of ion beam assisted deposition of optical thin films, *Vacuum*, 46 (1995) 645-659.
- [24] J.E. Greene, S.A. Barnett, Ion-surface interactions during vapor phase crystal growth by sputtering, MBE, and plasma-enhanced CVD: Applications to semiconductors, *Journal of Vacuum Science & Technology*, 21 (1982) 285-302.
- [25] K.H. Müller, R.P. Netterfield, P.J. Martin, Dynamics of zirconium oxide thin-film growth and ion-beam etching, *Physical Review B*, 35 (1987) 2934-2941.

Chapter 4

Growth Optimizations of AlN Thin Films

by Reactive Assistive IBSD

This chapter presents optimization studies on ion beam sputtered AlN thin films grown on Si(100) substrate. The experiments were aimed to optimize growth conditions as a function of different deposition parameters like, assisted ion energy, substrate temperature and deposition time. Surface morphology of AlN thin films was explored using atomic force microscopy (AFM) and scanning electron microscopy (SEM). An extensive investigation on microstructural variations, evolution of average crystallite size and AlN phase formation as a function of temperature was carried out using X-ray diffraction (XRD), transmission electron microscopy (TEM) and X-ray photoelectron spectroscopy (XPS). Positron annihilation spectroscopy is used to investigate the presence of defects in film microstructure.

Science and technology of AlN thin film has received tremendous attention in last few decades due to its numerous applications, especially, in the field of piezoelectricity based devices like sensors and actuators etc. In order to grow device grade AlN thin films, the first and most important step is the optimization of growth parameters specific to a deposition technique. The ease of operation, accurate control of the growth rate (thickness), excellent film adhesion and a high degree of reproducibility of the deposited films can be achieved by appropriately optimizing the deposition parameters. Herein, ion beam sputter deposition (IBSD) technique provides a method to deposit ultra-smooth thin films with high packing density and excellent adhesion with the substrate. IBSD has an added advantage

that ion beam energy and incident ion flux can be controlled independently. In view of this, growth of AlN thin films on Si(100) substrates was optimized for using IBSD in reactive assistive mode. Three distinct parameters were varied to achieve optimization. These are:

- I. Assisted ion energy
- II. Substrate temperature
- III. Deposition time

4.1 Optimization of Assisted Ion Energy

During reactive assistive IBSD, the metal atom flux was provided by sputtering aluminum (Al) target with argon ion (Ar^+) beam extracted from a 6 cm RF ion source. Simultaneously, reactively assistive flux of N^+/N_2^+ ions was supplied directly to the substrate surface by an end-Hall type ion source. To grow the wurtzite hexagonal phase of AlN thin films, a preliminary choice was made upon main ion beam energy at 500 eV and substrate temperature as 500°C , as reported in existing literature. The deposition time was kept constant at 20 minutes. Then, the assisted ion energy was varied from 60 eV, 90 eV and 120 eV. AlN thin films thus deposited were analysed using X-ray diffraction (XRD) for their crystallographic phase. Figure 4.1 displays the XRD patterns obtained at different assisted ion energies. It can easily be observed that at 60 eV, no significant signature of AlN formation is observed. As the assisted ion energy is increased to 90 eV, a feeble signature of cubic AlN (200) is observed. To enhance the formation of AlN phase, energy of reactive assistive flux is further increased to 120 eV. But no feature pertaining to AlN is observed. In view of these

observations from figure 4.1, the optimum energy of reactive assistive flux has been fixed at 90 eV for the growth of AlN thin films.

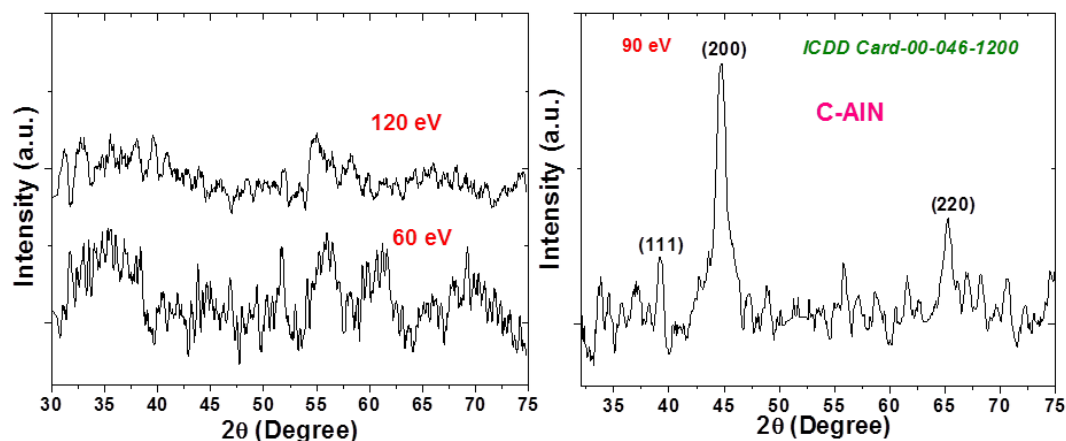


Figure 4.1 Plots of X-ray diffraction (XRD) measurements on AlN thin films deposited by reactive assistive IBSD at different assisted ion energy.

4.2 Optimization of Substrate Temperature

Substrate temperature plays a crucial role in film growth in reactive assistive IBSD. Increasing the substrate temperature above room temperature (RT) significantly suppresses the incorporation of water vapors (H_2O) and consequently the accompanying oxygen (O) content. Simultaneously, reactive gaseous ions become more mobile at higher substrate temperatures and hence favor efficient formation of AlN phase [1]. Thus, substrate temperature can be used as a decisive deposition parameter by varying which fractional composition of AlN can be improved while minimizing other inadvertently incorporated contaminants. In view of this, after optimizing the assisted ion beam energy, a systematic study was undertaken by varying the substrate temperature from room temperature (RT) to $500^{\circ}C$ in the steps of $100^{\circ}C$. Here, energy of main ion beam used to sputter the Al-target was kept fixed at 500 eV and films were grown for

20 minutes. The crystallographic information on deposited AlN thin films was obtained by X-ray diffraction (XRD). An extensive investigation was carried out on microstructural variations of deposited films using transmission electron microscopy (HR-TEM). Surface morphology was explored using atomic force microscopy (AFM) and scanning electron microscopy (SEM). AlN phase formation and evolution of average crystallite size as a function of temperature were investigated. In order to obtain the highest phase fraction of AlN on film surface, X-ray photoelectron spectroscopy (XPS) was employed to unravel the compositional variations of film surface for samples deposited at RT, 100°C and 500°C. Results of these investigations are described in the subsequent sections.

▪ *XRD investigations*

Figure 4.2 displays the results of XRD measurements AlN thin film samples deposited at different substrate temperatures. Grazing incidence XRD (GIXRD) patterns are shown in figure 4.2(A). The AlN thin films deposited for 20 minutes were found to be amorphous irrespective of substrate deposition temperature.

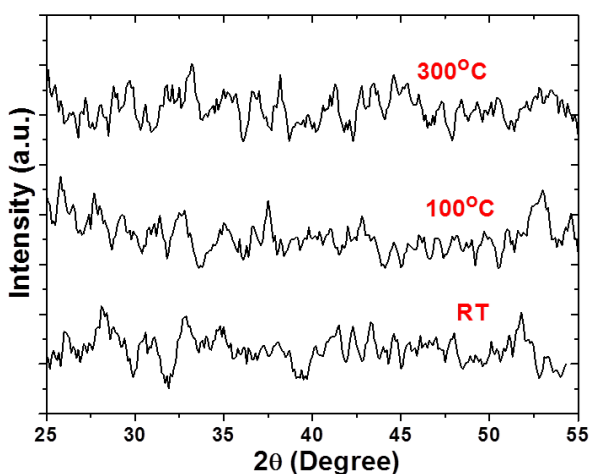


Figure 4.2 Grazing incidence X-ray diffraction (GIXRD) measurements on AlN thin films deposited at different substrate temperatures. The films were found to be amorphous in nature.

Hence, another set of AlN thin films were grown for longer deposition time of 30 minutes at different substrate temperatures from RT to 500°C in steps of 100°C. The observations from experimental investigations are presented and discussed in the subsequent sections.

▪ ***Surface morphology***

AFM (Ntegra Prima, NT-MDT, Russia) was used to investigate the morphological features of the films over 1 X 1 μm^2 and 5 X 5 μm^2 area at multiple locations on a 10 mm X 10 mm substrate. These are shown in figure 4.3. In all the films, surface morphology is found to be sensitive to the deposition temperature with the appearance of rapidly changing patterns and formation of cluster like structures. Distinct morphological features of film deposited at 500°C substrate temperature are highlighted with bright rings.

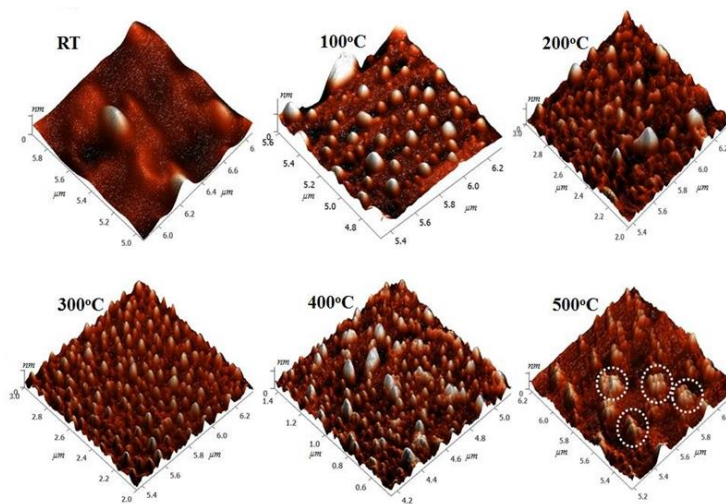


Figure 4.3 Surface morphology of AlN thin films deposited at different substrate temperatures acquired by atomic force microscopy (AFM). Some distinct morphological features are appeared at 500°C which are marked as dotted circles.

Average surface roughness (R_a) obtained at several locations of $5 \times 5 \mu\text{m}^2$ area was determined for samples deposited at each substrate temperature. The estimation indicates a net increase in R_a as the film microstructure changes from amorphous to nanocrystalline with the increase in substrate temperature. These values of R_a at each substrate temperature are listed in table 4.1.

The morphology of these films have also been analysed with scanning electron microscope (FE-SEM, Supra 55, Zeiss, Germany) at each deposition temperature, as shown in figure 4.4. Observations from these micrographs indicate that all the films are highly dense and pore free with reference to the surface coverage of the substrate. While films synthesized at RT and 100°C exhibit similar surface features and appear to be amorphous, those grown at 500°C exhibit cluster like features.

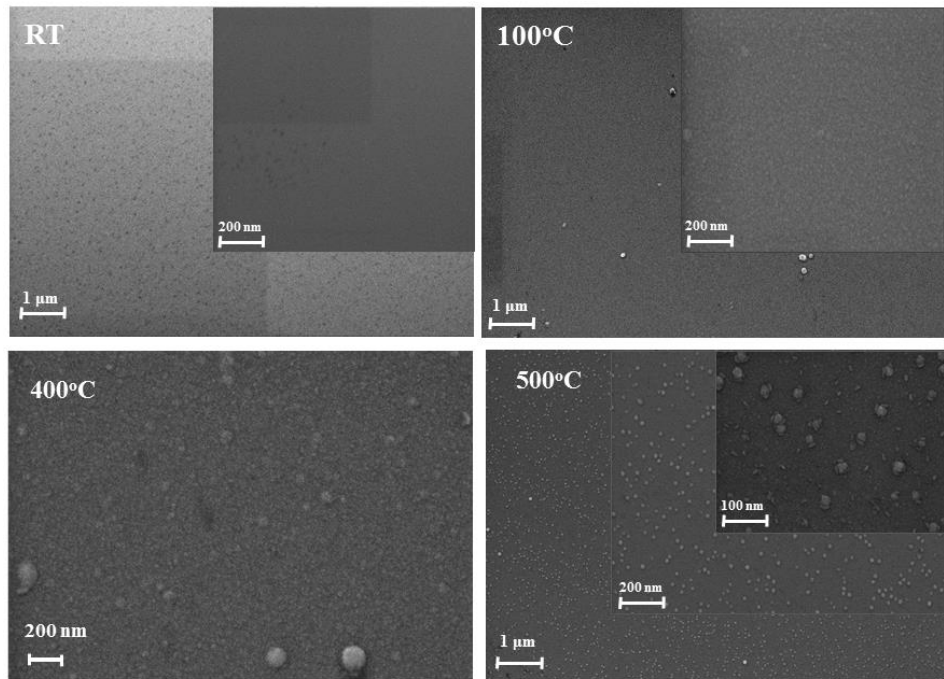


Figure 4.4 Morphology of the AlN thin films as seen by scanning electron microscope (SEM) when deposited at different substrate temperatures.

▪ *TEM measurements*

A systematic study on microstructural evolution of AlN thin films deposited at different substrate temperatures was carried out using high resolution TEM (Libra 200FE/HR-TEM). Selected area electron diffraction (SAED) patterns of these films have been analyzed to determine the evolution of the crystallographic phases and average crystallite size (d) at different substrate temperatures. Microstructural information of the films is depicted in figure 4.5(A) which displays dark field images acquired by TEM for samples deposited at different substrate temperature. A careful analysis of these dark field images reveal that the films deposited at RT to 200°C substrate temperature possess a random atomic network and lack in long range coordination in its microstructure.

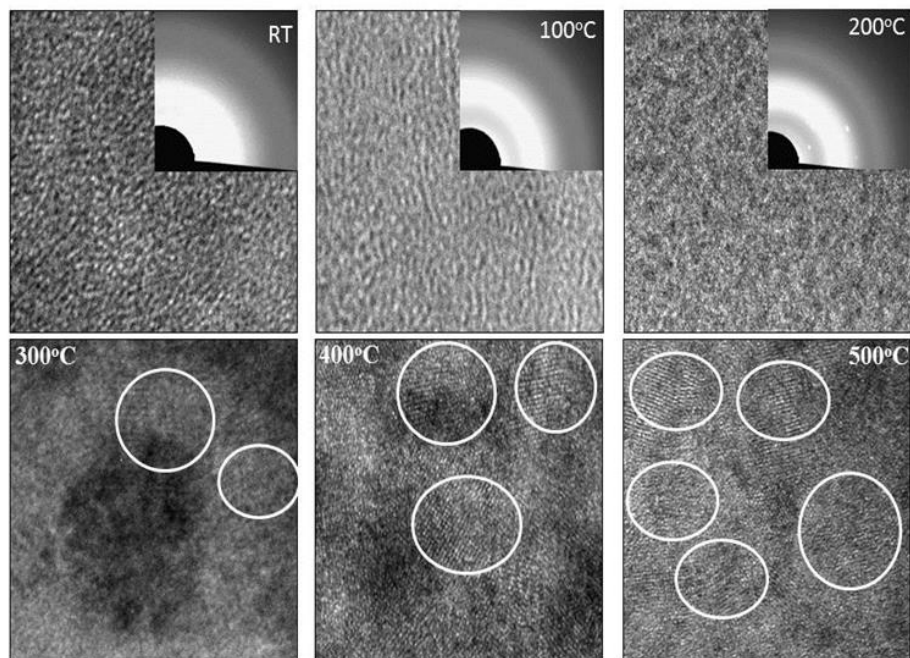


Figure 4.5(A) Dark field images acquired by TEM at each substrate temperature revealing structural transformations from room temperature (RT) to 500°C of AlN thin films. Selected area electron diffraction (SAED) patterns of the films prepared from RT to 200°C are shown in their in-set. While films deposited at 300°C to 500°C, crystalline region of interest are highlighted with bright rings.

This observation is further confirmed by the selected area electron diffraction (SAED) patterns shown in the inset of each image upto 200°C. However, for films deposited at 300°C substrate temperature, onset of crystallization is noticed which advances with further increase in substrate temperature and gradually evolves into a nanocrystalline microstructure at 400°C and 500°C. For clarity, few regions of interest (RoI) in these dark field images are shown by bright rings. Nanocrystalline microstructure of these films was further analysed by acquiring SAED patterns at each substrate temperature from 300°C to 500°C. These are shown in figure 4.5(B) along with an average crystallite size (d) distribution. The SAED pattern collected for the films deposited at 300°C substrate temperature show few weak Debye-Scherrer rings pertaining to the onset of crystallization in hexagonal phase of AlN with an average crystallite size (d) of 4.9 ± 0.3 nm. This process of crystallization continues at 400°C and SAED reveals the coexistence of both hexagonal and cubic phases of AlN having $d = 5.6 \pm 0.3$ nm with the appearance of several, relatively strong Debye-Scherrer rings. As the temperature of the substrate is further increased to 500°C, a number of strong Debye-Scherrer rings confirm the hexagonal phase of AlN to be the dominant constituent of film microstructure with $d = 9.7 \pm 0.2$ nm.

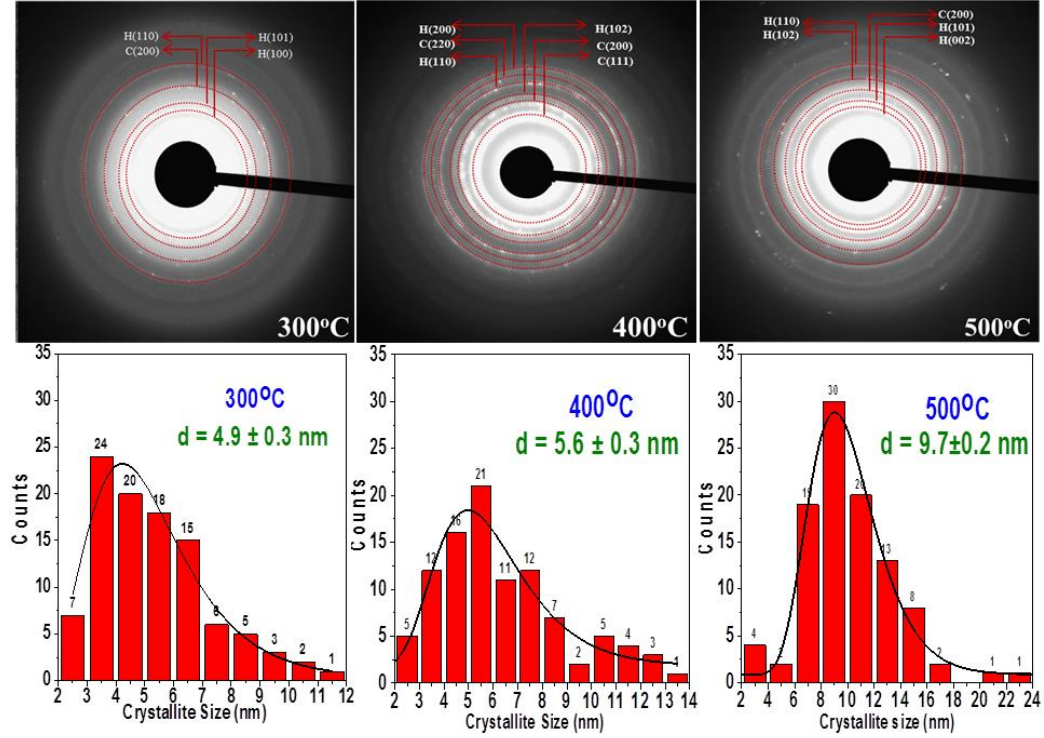


Figure 4.5(B) Selected area electron diffraction (SAED) patterns along with average crystallite size (d) distribution for the samples prepared at 300°C to 500°C substrate temperature.

All these observations clearly establish simultaneous existence of different phases of AlN with varying phase fractions indicating underlying structural transformations that strongly depend on substrate temperature during deposition.

Table 4.1 Microstructural details of the films extracted from TEM and AFM.

Substrate temperature (°C)	d (in nm)	R_a (in nm)
RT	Amorphous	1.3
100	Amorphous	2.4
200	Amorphous	1.0
300	4.9 ± 0.3	1.4
400	5.6 ± 0.3	1.8
500	9.7 ± 0.2	1.9

From RT to 200°C, films were predominantly found to be amorphous in nature, became nanocrystalline ($d < 5$ nm) at 300°C and evolved into microcrystalline ($5 \text{ nm} < d < 50 \text{ nm}$) aggregates at 400°C and 500°C temperatures. These observations on film microstructure are listed in table 4.1.

▪ ***Composition optimization by XPS***

Effect of substrate temperature on the compositional evolution of AlN thin films was also investigated to establish the phase fraction of AlN thin films formed during reactive assistive IBSD process. For this purpose, thin film samples were prepared at different substrate temperatures viz. RT, 100°C and 500°C. XPS (M/s Specs, Germany) analysis was carried out on these thin films to obtain the information about AlN phase formation and its subsequent quantification on the surface as well as 50 nm underneath the surface. In addition, entrainment of nitrogen and oxygen in their various chemical forms like Al-O and N-Al-O were also estimated by quantifying their respective phase fractions. For this, a monochromatic X-ray source of aluminum with $K_{\alpha} = 1486.6$ eV operated at 15 KV and 22 mA was employed. A concentric hemispherical analyzer of 150 mm diameter was used to analyze the photoelectrons with an electron takeoff angle of 90°. During measurement, base pressure of the spectrometer was kept constant at 2.3×10^{-10} mbar. The spectrometer is calibrated to the Ag-3d_{5/2} peak at 368.53 eV and C-1s peak at 284.6 eV. All the spectra were recorded with a resolution of 0.25 eV. For binding energy reference, C-1s peak was used. To estimate the composition of film beneath the surface, an argon (Ar) ion gun

(3KeV) was used to etch the film surface to a depth of 50 nm. The etch-rate was experimentally established at ~1.5 nm/minute.

Figure 4.6(A), 4.6(B) and 4.6(C) show the results of XPS survey scans for all the films deposited at various substrate temperatures. All these survey scans detected only aluminum (Al-2p and Al-2s), nitrogen (N-1s), oxygen (O-1s) and carbon (C-1s) at the surface of each thin film. Some amount of carbon, as indicated by the C-1s peak, is indicative of the mild surface contamination during sample handling. Prominent oxygen peak appears at RT as evident from figure 4.6(A) and its area reduces as the substrate temperature increases to 100°C and 500°C as shown in figure 4.6(B) & 4.6(C). In order to calculate the elemental atomic concentration (at. %) of all four elements, high-resolution scans were performed on the Al-2p, C-1s, N-1s and O-1s peaks to obtain surface core level spectra.

For this study, intensity vs. binding energy for a particular elemental scan was acquired as the peak. One or more components of a peak which were mathematically deconvoluted to represent distinct chemical states within the elemental peak have been designated as subpeaks. All the subpeaks were fitted using a linear combination of Gaussian and Lorentzian line shapes, commonly referred as pseudo-Voigt function [2]. Elemental atomic concentration was obtained after calculating the subpeak areas and applying relative sensitivity factors (RSFs) of 0.537, 1.000, 1.800 and 2.930 for Al-2p, C-1s, N-1s and O-1s, respectively. Deconvolution of each core-level elemental peak is shown in figure

4.7 and estimation of corresponding compositional variations at each substrate temperature are explained in the following sections.

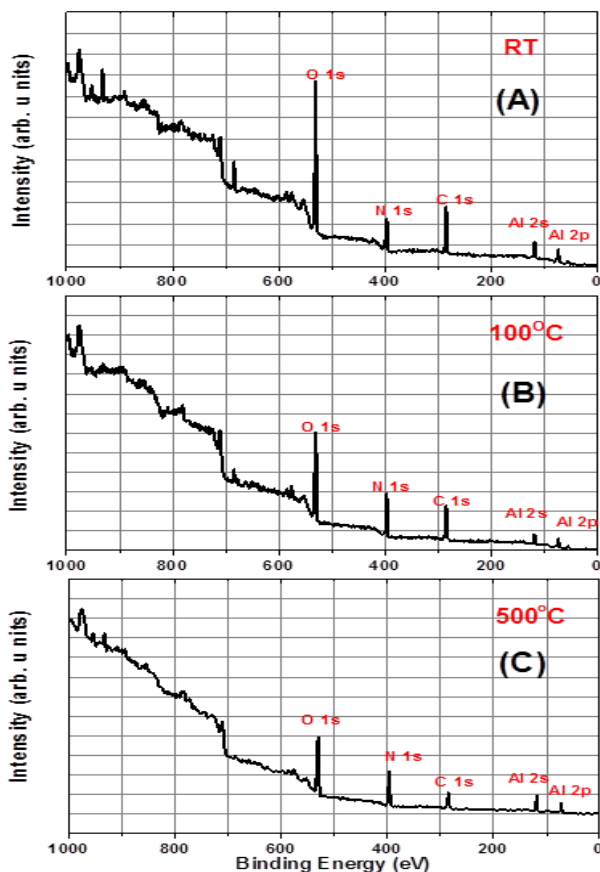


Figure 4.6 1000 eV wide survey scans of AlN thin films deposited at (A) RT, (B) 100°C and (C) 500°C substrate temperatures.

Al-2p peak

The core-level spectra of Al-2p peak acquired at different substrate temperatures are shown in figure 4.7A. The nature of different phases formed during deposition can be inferred from the deconvoluted components of these Al-2p peaks. For this, each individual Al-2p peak was deconvoluted using pseudo-Voigt function into a pair of $2p_{3/2}$ and $2p_{1/2}$ spin-orbit split subpeaks. Figure 4.7A(a) shows that at RT, the Al-2p peak splits into a higher intensity subpeak Al-

$2p_{3/2}$ at 74.0 eV binding energy and a lower intensity subpeak Al- $2p_{1/2}$ appearing at 74.9 eV binding energy. As the temperature of the substrate is raised to 100°C, Al- $2p_{3/2}$ appears at the same position with ~74.0 eV binding energy but Al- $2p_{1/2}$ peak occurs at 74.3 eV with a chemical shift of 0.6 eV on the lower binding energy side of the spectra as shown in figure 4.7A(b). But no further chemical shift is observed for the peak Al- $2p_{3/2}$ as well as for the peak Al- $2p_{1/2}$ whose position remains same when the substrate temperature was increased to 500°C (figure 4.7A(c)).

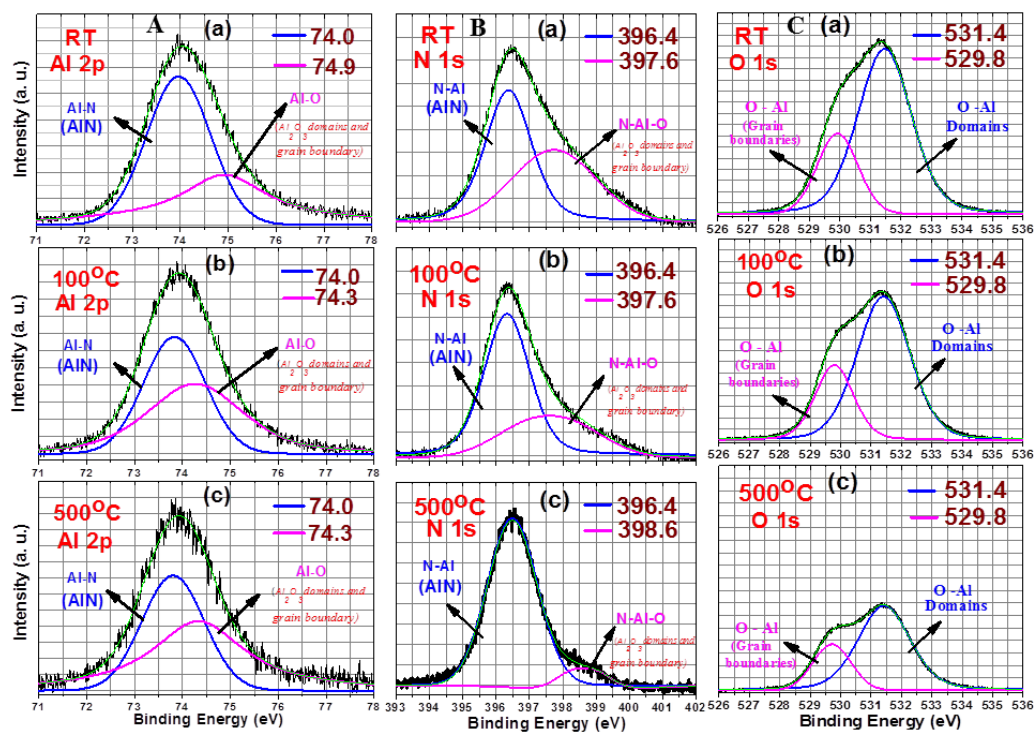


Figure 4.7 A series of plots deconvoluted into constituent subpeaks of, (A) Al-2p peak, (B) N-1s peak, (C) O-1s. These plots progress from top to bottom in cumulative substrate temperature as (a) RT, (b) 100°C and (c) 500°C.

These binding energy values are listed in table 4.2 at each substrate temperature. From these observations, it is clear that each core level Al-2p peak is composed of two distinctly different contributions arising from chemical

coordination. The Al-2p_{3/2} subpeak occurring at ~74.0 eV can be assigned to nitridic aluminum in the form of AlN that retains the original 2H polytypoid (P6₃mc) structure of AlN [3-7].

The other subpeak Al-2p_{1/2} with the binding energy lying in the range 74.3 – 74.9 eV can be attributed to the oxidic aluminum in alumina (Al₂O₃) frame work. But the noticeable fact here is that the subpeak Al-2p_{1/2} is associated with a chemical shift of 0.6 eV on the lower binding energy side as the temperature of the substrate is increased from RT to 100°C. This peak position remains same when the substrate temperature is further raised to 500°C. This chemical shift is a finger print of the valence electrons' bonding environment which in turn affects the overall electrostatic interaction in the atom. A qualitative explanation for this chemical shift effect lies in the oxidation state of aluminum in which it combines with highly electronegative oxygen species in Al–O type of interactions. As a consequence of combined effect of oxygen's high electron affinity and large difference in electronegativity between aluminum and oxygen, the aluminum electrons remain attracted towards the oxygen atom. Thus a chemical shift of Al-2p_{1/2} on the lower binding energy side indicates that aluminum acquires apparently lower oxidation states among Al⁺¹ and Al⁺² relative to Al⁺³ [8]. This scenario originates from a lesser contribution of aluminum electrons to the oxygen atom in the periphery of Al₂O₃ domains. Consequently, the Al-2p_{1/2} electrons become less attracted towards the aluminum nucleus and hence appear at lower binding energy in the core level spectra of Al-2p. Thus changes in the valence environment result in the change in the binding energy of all the inner

core electrons [9]. This chemical shift on the lower binding energy side at 500°C is consistent with amorphous character of Al–O kind of interactions and can also be taken as a signature of reduced co-operation of oxygen during deposition at higher substrate temperature [8].

N-1s peak

Successive plots of N-1s peak at different substrate temperatures and their respective deconvoluted subpeaks are shown in figure 4.7B. Two subpeaks are used in fitting each N-1s peak using pseudo-Voigt line shapes at each substrate temperature. Among them, subpeak with higher intensity is designated as N-1s^{#1} and that with lower intensity as N-1s^{#2}. Figure 4.7B(a) presents the N-1s peak observed from the AlN thin film grown at RT. The subpeak N-1s^{#1} has a binding energy of 396.4 eV while other subpeak N-1s^{#2} appears at 397.6 eV. As the temperature of the substrate is raised to 100°C, no change in the binding energies of subpeaks N-1s^{#1} and N-1s^{#2} are observed. This is shown in figure 4.7B(b). At 500°C substrate temperature, it can be observed from figure 4.7B(c) that the subpeak N-1s^{#1} appears at the same position. A significant change is found in the occurrence of the subpeak N-1s^{#2} which appears at 398.6 eV with a chemical shift of 1 eV on the higher binding energy side. Aforementioned observations establish that the subpeak N-1s^{#1} has its binding energy ~396.4 eV at all temperatures. This binding energy value is consistent with that nitrogen contribution towards N-1s peak which stems from its binding with aluminum in wurtzite hexagonal AlN (i.e. 2H polytypoid) framework. This can be understood by the hypothesis given by Costales et al. [10]. In reactive assistive IBSD, major fraction of the nitrogen flux

arriving at the growing AlN film surface is N^+/N_2^+ ions. These ions are incorporated into the growing film and progressively increase their coordination to aluminum species until a stable single bonded N–Al structure is established in wurtzite hexagonal phase of AlN. This enhanced appearance of N-1s^{#1} peak at higher substrate temperatures also strengthens the fact that N^+/N_2^+ ions arriving at the substrate surface through reactive assistance become more mobile and hence react more efficiently with aluminum to form AlN compound phase which becomes the dominant phase fraction in the thin film microstructure. At the same time, the subpeak N-1s^{#2} is observed in the binding energy range of 397.6 eV to 398.6 eV. These binding energy values match well with that contribution of N-1s which forms a ternary bonding system N–Al–O generally referred to as aluminum oxynitride. This normally occurs in spinel as well as in amorphous phases. According to L. Rosenberger et al. [3], N-1s^{#2} is a representative of that nitrogen which exists in an intermediate electron withdrawing environment where nitrogen is bound to an aluminum atom, which in turn is bound to an oxygen. Thus, in the light of the reports existing in literature on XPS studies of aluminum oxynitride, it can be inferred that emergence of N-1s^{#2} peak attributes to N^+/N_2^+ ion induced nitriding of Al_2O_3 present in the form of tiny domains as well as in the grain boundaries. This diminution in the N-1s^{#2} peak intensity along with a chemical shift on the higher binding energy side also implies reduced incorporation of oxygen as well as H_2O vapor at 500°C substrate temperature. At this temperature, the probability of nitrogen encountering aluminum preferably increases which further enhances the AlN phase fraction. It also supports the observation that a

major concentration of nitrogen binds to aluminum and only a small amount of oxygen is able to interact with aluminum forming amorphous and spinel N-Al-O at the grain boundaries. Although, it is found in very low concentrations as this type of N-Al-O interaction is not energetically favorable all the time. These binding energy values for all the subpeaks of N-1s are listed in table 4.2.

Table 4.2 Variation of binding energy of each subpeak with substrate temperature.

Substrate temperature (°C)	Subpeaks (Binding Energy, eV)					
	Al-2p _{3/2}	Al-2p _{1/2}	N-1s ^{#1}	N-1s ^{#2}	O-1s ^{#1}	O-1s ^{#2}
RT	74.0	74.9	396.4	397.6	531.4	529.8
100	74.0	74.3	396.4	397.6	531.4	529.8
500	74.0	74.3	396.4	398.6	531.4	529.8
50 nm beneath the Surface	74.0	76.0	396.2	397.8	531.3	530.5

Above observations are further bolstered from the calculation of AlN phase fraction formed at each substrate temperature. Generally in XPS, the phase fraction of a compound AB can be calculated using following equation [9]:

$$\frac{n_A}{n_B} = \frac{I_A}{I_B} * \frac{(RSF)_B}{(RSF)_A} \quad (1)$$

Where n_A and n_B are the at. % concentration of element A and B, respectively. I_A and I_B represent their respective area under the XPS peak. To estimate the phase fraction in at. % of AlN in the film at each substrate temperature, following assumptions were made:

- It was considered that AlN_x as AlN is the only stable compound in the binary phase diagram of Al and N.

- ii. While calculating n_{Al}/n_N in AlN_x , n_{Al} was taken as 1 which confirms the presence of Al atoms on the substrate as Al target was separately sputtered by a beam of 500 eV Ar^+ ions.
- iii. In view of above two assumptions, the value of 'x' will denote the amount of nitrogen (N) accessible for AlN formation.

Thus, Al-2p_{3/2} and N-1s^{#1} subpeaks were analyzed together. Herin, it is kept in mind that while calculating the phase fraction of AlN, the ratio of area under the Al-subpeaks i.e. Al-2p_{3/2}: Al-2p_{1/2} should be equal to 2:1. The present calculations suggest that at RT, 46.0 at. % AlN is formed. At 100°C substrate temperature, interaction of aluminum with nitrogen gets enhanced as compared to RT and 58.0 at. % of AlN is observed. With further increase in substrate temperature to 500°C, N⁺/N₂⁺ ion flux interacts more efficiently to increase its coordination with aluminum to form AlN and this phase becomes dominant over other possible elemental interactions. Hence 74.0 at. % AlN is formed on the surface which is substantially higher phase fraction synthesized by reactive assistive IBSD as compared to other PVD techniques [7-8]. Thus, as a consequence of the increase in substrate temperature, aluminum-nitrogen (Al-N) interaction becomes dominant, forming higher phase fraction of AlN. Therefore, it is clearly understood that higher phase fraction of AlN can be grown by reactive assistive IBSD at a substrate temperature of 500°C during deposition. As explained earlier, the subpeaks Al-2p_{1/2} and N-1s^{#2} indicate their respective interaction with oxygen. Therefore, to address this aspect, high resolution spectrum of O-1s is analysed in

the next section to delineate the role of oxygen during the growth of AlN thin films by reactive assistive IBSD.

O-1s peak

Successive O-1s spectra from AlN thin films grown at successive substrate temperatures are shown in figure 4.7C. The O-1s peak was fitted to two subpeaks using pseudo-Voigt line shapes. The subpeak with higher intensity is designated as O-1s^{#1} while other one with lower intensity is designated as O-1s^{#2} for all the spectra. One noticeable feature of figure 4.7C is that, as the temperature of the substrate increases, intensity of O-1s peak decreases indicating reduced incorporation of oxygen at higher substrate temperatures. The subpeak O-1s^{#1} is found to possess ~531.4 eV binding energy at all substrate temperatures as shown in figures 4.7C(a), 4.7C(b) and 4.7C(c). As suggested by Harris et al. [11], this subpeak can be assigned to oxygen bound to aluminum with high coordination number forming tiny domains of α -Al₂O₃. Thus, the subpeak O-1s^{#1} together with Al-2p_{1/2} was analysed to calculate the fraction of Al₂O₃ domains using equation (1). At RT, 31.0 at. % Al₂O₃ is found to occur in the form of tiny domains. This fractional contribution decreases to 25.3 at. % as the temperature of the substrate is raised to 100°C. Finally, at 500°C substrate temperature, the observed fraction of Al₂O₃ domains assumes a minimum value of 23.7 at. %.

It is a well-recognized fact that AlN exhibits immense affinity towards oxygen. In fact, aluminum binds with oxygen more readily than nitrogen due to the larger difference in their electronegativities. On the nature of oxygen accommodation in AlN structure, Mccauley et al. constructed a binary phase

diagram of AlN-Al₂O₃ [12]. According to Mccauley et al., at high concentrations, oxygen interacts with aluminum and incorporates itself into distinct crystallographic phases in AlN structure. In the present case, this crystallographic phase is represented by the binding energy at which O-1s^{#1} appears corresponding to Al₂O₃ present in the form of tiny domains. This is possible in two ways; (1) by the replacement of nitrogen with oxygen from the regular lattice site; (2) preferred bonding of oxygen with dangling aluminum on the surface. Both of these phenomena can contribute equally towards formation of Al₂O₃ domains or as grain boundary inclusions on the surface as this oxygen is atmospheric, not a part of deposition process.

The subpeak O-1s^{#2} is obtained with 529.8 eV binding energy at all substrate temperatures without changing its position as presented in figures 4.7C(a), 4.7C(b) and 4.7C(c). This subpeak can be attributed to the following three types of contributions. (i). Oxygen bound to aluminum with reduced coordination in the grain boundaries like N-Al(OH)₂. (ii). Oxidized aluminum at the grain boundaries of AlN crystals and (iii). O-Al interaction resulting from the reaction of molecular oxygen or water with aluminum at film surface and vacuum interface but with significant contribution from crystal-grain interface [3, 7]. To calculate the percentage fraction of these O-Al interaction at grain boundaries, O-1s^{#2} together with Al-2p_{1/2} are analysed using equation (1). Total contribution of 10.6 at. % is observed at RT which is reduced to 9.8 at % and 8.3 at. % at the substrate temperatures 100°C and 500°C, respectively. These values of elemental concentrations are listed in table 4.3. At these low concentrations, oxygen present

as substitutional point defect combines with aluminum vacancy forming isolated AlO octahedra in the grain boundaries. If circumstances permit, these octahedral defects may organize themselves into interspaced planes dispersed in the grain boundary on the surface, as suggested by Mccauley et al. [12].

Table 4.3 Atomic concentration at different substrate temperatures.

Substrate Temperature (°C)	Chemical Composition (at. %)		
	AlN	Al ₂ O ₃ as tiny domains	Al-O in Grain boundaries
RT	46.0	31.0	10.6
100	58.0	25.3	9.8
500	74.0	23.7	8.3
50 nm beneath the Surface	89.0	0.0	≤ 11.0

The findings from Al-2p, N-1s and O-1s peaks establish together that at 500°C, maximum phase fraction of film microstructure is constituted by wurtzite hexagonal phase of AlN with least interference from oxygen. Thus, it becomes equally important to see the composition of AlN thin film well below the surface. To reveal bulk composition, the AlN grown at 500°C was etched upto 50 nm beneath the surface. The survey spectrum at this depth representing the actual composition of the film is shown in figure 4.8(A). On comparing figure 4.8(A) with figure 4.6(C), three main differences are clearly revealed: (1) O-1s peak shows a prominent drop in its intensity; (2) Al-2p, Al-2s and N-1s show a significant rise in their intensity; (3) C-1s peak intensity declines drastically.

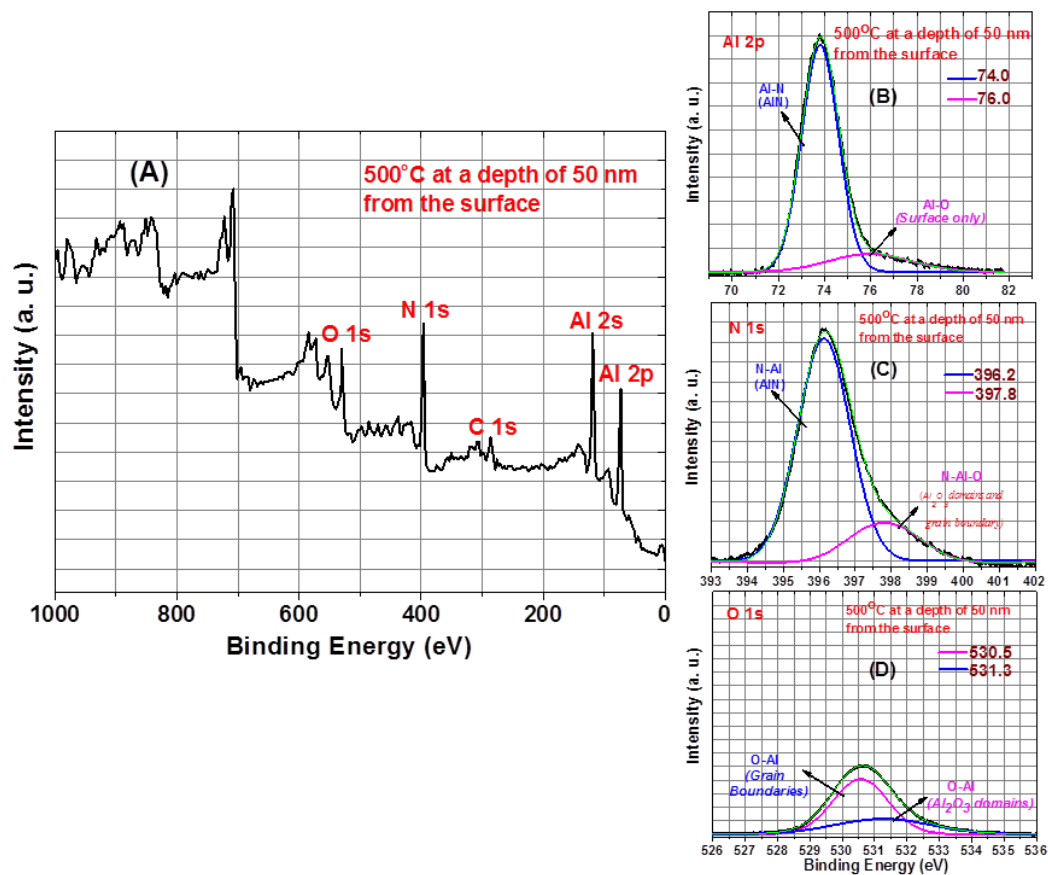


Figure 4.8 X-ray photoelectron spectroscopy (XPS) of AlN thin films, deposited at 500°C, at a depth of 50 nm from the surface; (A) Survey scan; (B) Al-2p core level spectrum; (C) N-1s core level spectrum and (D) O-1s core level spectrum.

Corresponding core-level spectra of Al-2p, N-1s and O-1s are shown in figures 4.8(B), 4.8(C) and 4.8(D), respectively. In figure 4.8(B), the Al-2p_{3/2} peak prevailed as the major peak at the same binding energy position of 74.0 eV as it appeared at the surface shown in figure 4.7A(c). Thus, it can easily be concluded from figure 4.8(B) that in the bulk of the film, the actual composition is predominantly constituted by that aluminum which is exclusively bound to nitrogen forming wurtzite hexagonal phase of AlN. At the same time, the subpeak Al-2p_{1/2} which appeared at 74.3 eV binding energy in figure 4.7A(c) does not appear in figure 4.8(B) and a tiny peak Al-2p^{#2} appears at 76.0 eV. This Al-2p^{#2}

peak represents the Al-O kind of interaction which takes place only at the surface. Therefore, no significant incorporation of oxygen appears in this case and actual composition in the bulk of the film is mainly attributed to AlN phase only. This observation is also corroborated by the presence of N-1s^{#1} peak as the major peak in figure 4.8(C) that occurs almost at the same position at which it appeared in figure 4.7B(c), representing the nitrogen bound to aluminum only. Both the subpeaks in O-1s core-level spectrum shown in figure 4.8(D) remain at the same position when compared to that in figure 4.7C(c). At 50 nm beneath the surface, rise of the peak pertaining to O-Al interaction in the grain boundary as the major peak and suppression of the peak at 531.3 indicate only a feeble intervention from oxygen in film microstructure. Following the procedure described earlier in this section, the phase fraction of AlN thin film grown at 500°C was calculated and found to be 89.0 at. % at a depth of 50 nm beneath the surface. This high fraction of AlN in wurtzite hexagonal structure is phenomenal when compared to other existing reports on this subject [7-8, 10, 13]. None the less, a negligible contribution from N-Al-O type of interaction may persist. Hence, at this point, above observations together establish that AlN thin films with high phase fraction of AlN on surface as well as well beneath the surface can be grown by reactive assistive IBSD by maintaining the substrate temperature at 500°C during deposition. These results are consolidated in figure 4.9 displaying substrate temperature dependent compositional variations of these phases on the surface and at a depth of 50 nm underneath the surface.

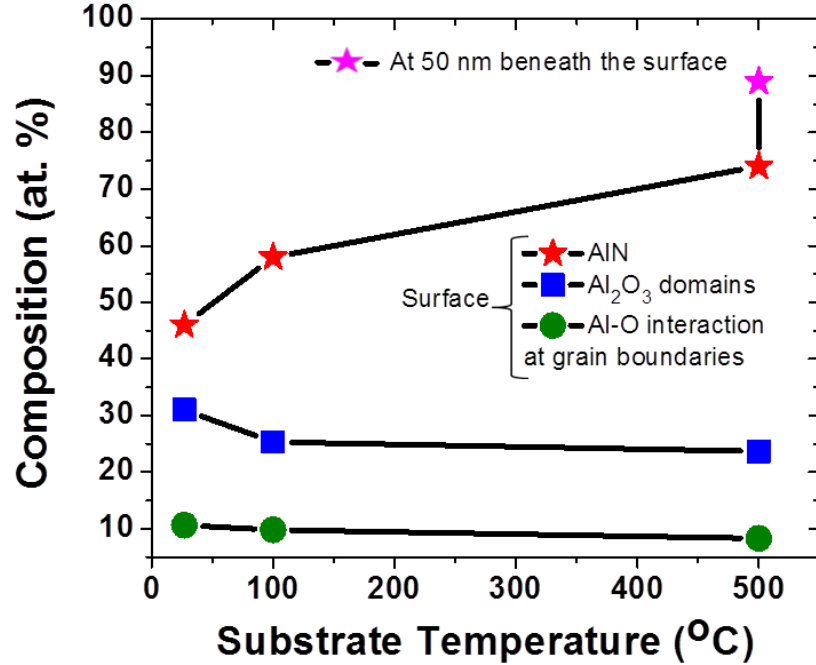


Figure 4.9 Compositional variation of AlN along with Al₂O₃ domains and Al-O interaction at the grain boundaries with substrate temperature. A distinct increase in AlN phase fraction is observed at 500°C substrate temperature.

▪ *Depth resolved Doppler broadening measurements*

Depth resolved Doppler broadening measurements were carried out on reactive assistive IBSD grown AlN thin films on Si(100) substrate using the low energy positron beam. The positron beam energy (E_p) was varied from 250 eV to 21.5 keV in steps of 0.5 keV and Doppler broadened 511 keV annihilation energy spectrum was obtained for each positron beam energy using an HPGe detector having 30 % efficiency. From each annihilation spectrum, S-parameter (S) was deduced and plotted as a function of positron beam energy. Figure 4.10 shows the variation of S-parameter as a function of positron beam energy on AlN thin films grown at different substrate temperatures. The mean implantation depth of the positron beam in the sample is shown on the top axis.

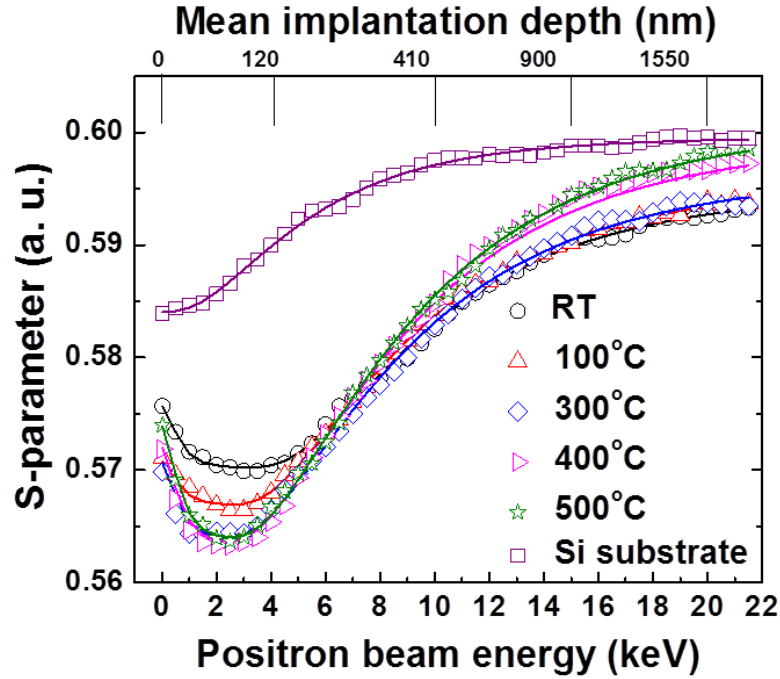


Figure 4.10 Variation of S-parameter (S) with positron beam energy (E_p) for different substrate temperatures. For reference, S vs E_p curve of Si(100) substrate is also plotted.

For the Si(100) substrate, the S-parameter increases with positron beam energy and beyond 8 keV, the S-parameter saturates corresponding to positron annihilation in bulk Si. For AlN thin films on Si(100) substrate, the S-parameter is initially high but decreases afterwards reaching a minimum at 2 keV. This minimum at 2 keV is attributed to positron annihilation in the AlN thin film. Beyond ~4 keV, the S-parameter slowly increases and saturates beyond 14 keV corresponding to annihilation in the Si(100) substrate. The low S_{AlN} when compared to S_{Si} is consistent with the literature which reports a value of 157 ps for AlN [14] and 215 ps for Si [15]. VEPFIT analyses were carried out on the experimental S vs E_p curves [16] and S-parameter corresponding to the surface, thin film and the substrate were obtained. Two layers, comprising of the overlayer and the substrate with an internal electric field were chosen to give a perfect fit.

The solid lines in figure 4.10 were obtained from VEPFIT analyses. Figure 4.11 shows the VEPFIT deduced S_{AlN} obtained as a function of substrate temperature. It is seen that the S-parameter is high for the room temperature deposition and decreases as the substrate temperature is increased. It saturates for substrate temperature beyond 300°C. The high S_{AlN} for the room temperature deposited AlN/Si may be due to the fact that the deposited film is amorphous (as coming from SAED results) and contains open volume defects rendering the S-parameter high.

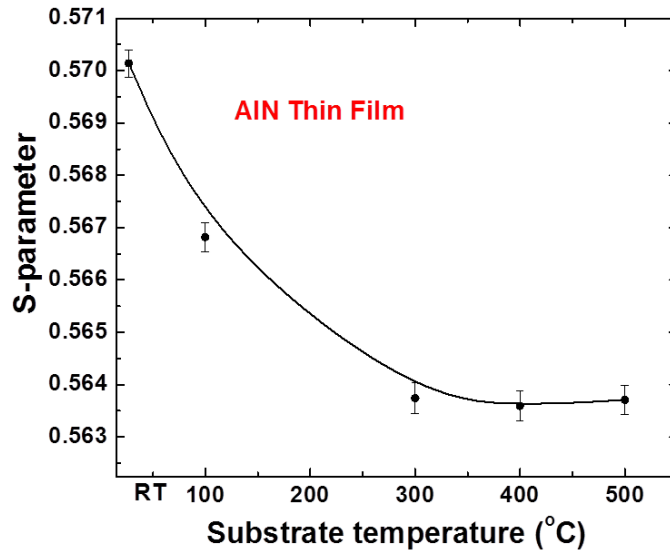


Figure 4.11 VEPFIT deduced S_{AlN} vs. substrate temperature.

As the substrate temperature is increased, the crystallinity of overlayer increases (as seen from SAED pattern in figure 4.5(B)) thereby making it less defected. Therefore, the S_{AlN} decreases with increasing substrate temperatures. But the saturation behavior of S-parameter beyond 300°C needs further analysis.

For all the deposition conditions, the positron diffusion length turns out to be very short (typically 6 nm). Therefore, short diffusion length would imply

presence of defect traps for the positrons. The short positron diffusion length even for the 500°C sample would imply presence of defect trapping sites in the over layer. Therefore, it is necessary to understand the various positron defect trapping sites in AlN. Uedono et al. [17] have shown that V_{Al} , V_N , $V_{Al}V_N$ and $V_{Al}(O)N$ complexes are the dominant defects in AlN. It is reported in the paper that S-parameter increases in the order defect free $< V_N < V_{Al}(O)N < V_{Al} < V_{Al}V_N$. Based on the changes in S of the defects with respect to that obtained for defect free AlN reported by Uedono et al. [17], it may be implied that the trapping sites in the over layer at 500°C may be Nitrogen vacancies (V_N) and or Aluminum vacancies with Oxygen complexes ($V_{Al}(O)N$). Even at high substrate temperatures which improves crystallinity, defects were still present in the AlN over layer.

4.3 Optimization of Deposition Time

By virtue of above observations, assisted ion energy was optimized at 90 eV with main ion beam energy of 500 eV used for sputtering. As specific features appeared on the film surface at 500°C and similar phase fraction of AlN is formed at 400°C and 500°C, substrate temperature was optimized at 400°C for further optimization of deposition time to obtain wurtzite hexagonal AlN in thin film form. For this, deposition time was varied as 3, 5, 8, 15, 30, 45 and 60 minutes. Formation of AlN was confirmed by XRD measurements which are shown in figure 4.12.

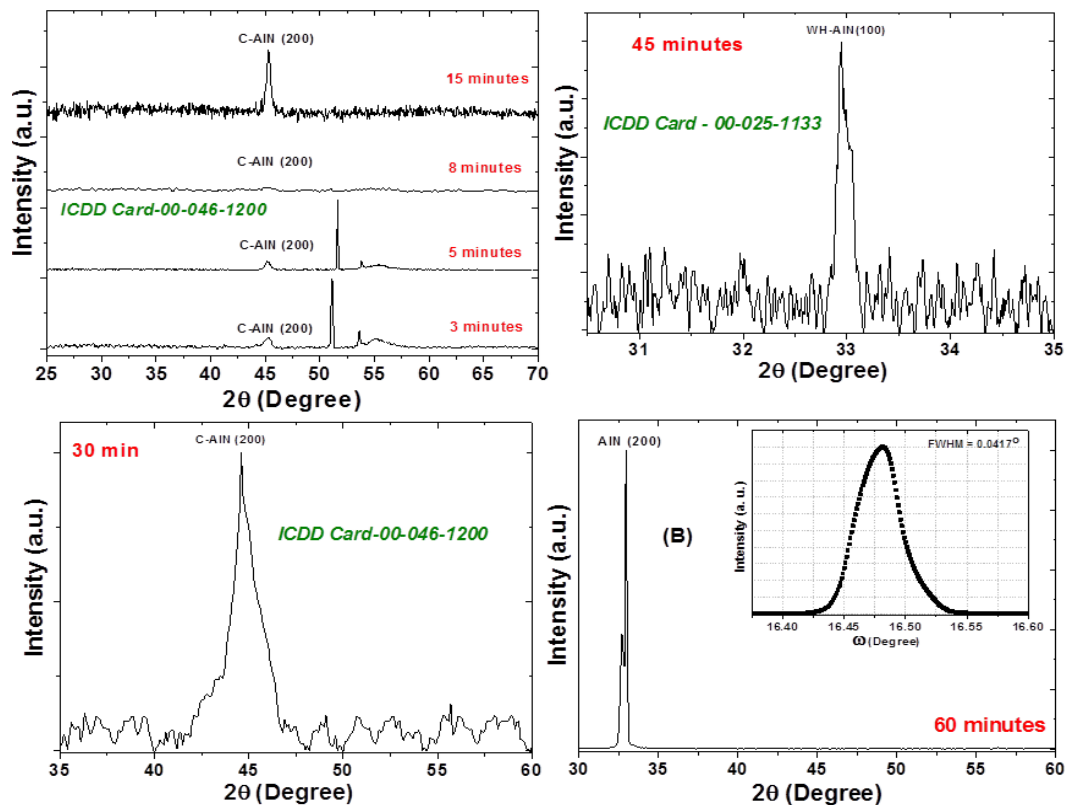


Figure 4.12 Growth of AlN thin films for different deposition time. Formation of wurtzite hexagonal (WH) phase of AlN takes place for 45 minutes of deposition.

It is found that for short deposition times from 3 to 15 minutes, cubic phase of AlN is formed. For films deposited for 3 and 5 minutes, full coverage of substrate surface could not take place. Thus a peak pertaining to Si miscut plane (311) also appears along with a sharp peak which is considered to occur due to some anomalous scattering as reported in literature. This cubic phase of AlN persists when the deposition time is increased to 30 minutes. With further increase in deposition time to 45 minutes, AlN could stabilize in wurtzite hexagonal phase. To enhance the formation of this WH-AlN, deposition time was further increased to 60 minutes. In GIXRD, no peak pertaining to AlN could be found. Thus symmetric θ -2 θ scan was performed to verify the growth of textured AlN thin

films. A preferred orientation along a-axis was revealed from appearance of a single (100) peak at 32.95° for films grown for 60 minutes which is displayed in figure 4.12. It shows that AlN crystals were oriented so as to have their family of planes (100) parallel to the substrate's family of planes (100). Subsequently, rocking curve measurements (ω -scan) were carried out to determine the degree of orientation which is displayed in the inset of corresponding symmetric scan for 60 minutes. The full width at half maximum (FWHM) of the rocking curve provides a direct estimation of relative disorientation of the grains. In figure 4.12, the FWHM of the rocking curve is found to be 0.0417° which indicates that the crystals were slightly disoriented with respect to each other. Thus, AlN thin films grown on Si(100) substrates for 60 minutes at 500°C were found to exhibit high degree of texture along a-axis.

4.4 Conclusion

To deposit AlN thin films with minimum contamination, deposition parameters were systematically varied. Microstructural investigation was carried out to confirm the formation of AlN phase. Surface composition analysis was used to pin-point undesirable constituents and arrives upon a set of parameters that leads to the deposition of high quality AlN thin film. Simultaneously, the findings of sections 4.1, 4.2 and 4.3 together indicate that cubic and wurtzite hexagonal phase of AlN can be grown by reactive assistive IBSD at optimized deposition parameters which are listed in table 4.4.

Table 4.4 Optimized deposition parameters for cubic and hexagonal AlN thin films using reactive assistive IBSD.

Crystallographic Phase of AlN	Main Ion beam energy	Assistive ion beam energy	Substrate temperature	Deposition time
Cubic	500 eV	90 eV	400°C	30 minutes
Wurtzite Hexagonal	500 eV	90 eV	400°C	45 minutes
a-axis textured Wurtzite hexagonal	500 eV	90 eV	400°C	60 minutes

Also, it can be clearly observed from table 4.4 that the two different phases of AlN can be stabilized just by controlling the deposition time.

References

- [1] O. Auciello, A. Gras-Martí, J.A. Valles-Abarca, D.L. Flamm, Plasma-Surface Interactions and Processing of Materials, Springer Netherlands, 2012.
- [2] G.K. Wertheim, M.A. Butler, K.W. West, D.N.E. Buchanan, Determination of the Gaussian and Lorentzian content of experimental line shapes, Review of Scientific Instruments, 45 (1974) 1369-1371.
- [3] L. Rosenberger, R. Baird, E. McCullen, G. Auner, G. Shreve, XPS analysis of aluminum nitride films deposited by plasma source molecular beam epitaxy, Surface and Interface Analysis, 40 (2008) 1254-1261.
- [4] J.D. Andrade, Surface and Interfacial Aspects of Biomedical Polymers: Volume 1 Surface Chemistry and Physics, Springer US, 2012.
- [5] D. Manova, V. Dimitrova, W. Fukarek, D. Karpuzov, Investigation of d.c.-reactive magnetron-sputtered AlN thin films by electron microprobe analysis,

- X-ray photoelectron spectroscopy and polarised infra-red reflection, *Surface and Coatings Technology*, 106 (1998) 205-208.
- [6] N. Duez, B. Mutel, O. Dessaux, P. Goudmand, J. Grimblot, AlN formation by direct nitrogen implantation using a DECR plasma, *Surface and Coatings Technology*, 125 (2000) 79-83.
- [7] P. Motamedi, K. Cadien, XPS analysis of AlN thin films deposited by plasma enhanced atomic layer deposition, *Applied Surface Science*, 315 (2014) 104-109.
- [8] N. Laidani, L. Vanzetti, M. Anderle, A. Basillais, C. Boulmer-Leborgne, J. Perriere, Chemical structure of films grown by AlN laser ablation: an X-ray photoelectron spectroscopy study, *Surface and Coatings Technology*, 122 (1999) 242-246.
- [9] J.D. Andrade, *Surface and Interfacial Aspects of Biomedical Polymers: Volume 1 Surface Chemistry and Physics*, Springer US, 2012.
- [10] A. Costales, M.A. Blanco, Á. Martín Pendás, A.K. Kandalam, R. Pandey, Chemical Bonding in Group III Nitrides, *Journal of the American Chemical Society*, 124 (2002) 4116-4123.
- [11] J.H. Harris, R.A. Youngman, R.G. Teller, On the nature of the oxygen-related defect in aluminum nitride, *Journal of Materials Research*, 5 (1990) 1763-1773.
- [12] K.M.K. J.W. Mccauley, R.S. Rai, G. Thomas(Eds.), *Anion-controlled microstructures in the AlN-Al₂O₃ system*, Plenum Publishing Corporation, 1988.

- [13] S. Schoser, G. Bräuchle, J. Forget, K. Kohlhof, T. Weber, J. Voigt, B. Rauschenbach, XPS investigation of AlN formation in aluminum alloys using plasma source ion implantation, *Surface and Coatings Technology*, 103–104 (1998) 222-226.
- [14] F. Tuomisto, J.M. Mäki, T.Y. Chemekova, Y.N. Makarov, O.V. Avdeev, E.N. Mokhov, A.S. Segal, M.G. Ramm, S. Davis, G. Huminic, H. Helava, M. Bickermann, B.M. Epelbaum, Characterization of bulk AlN crystals with positron annihilation spectroscopy, *Journal of Crystal Growth*, 310 (2008) 3998-4001.
- [15] R. Krause-Rehberg, H.S. Leipner, *Positron Annihilation in Semiconductors: Defect Studies*, Springer, 1999.
- [16] A.V. Veen, H. Schut, J.d. Vries, R.A. Hakvoort, M.R. Ijpma, Analysis of positron profiling data by means of “VEPFIT”, *AIP Conference Proceedings*, 218 (1991) 171-198.
- [17] A. Uedono, S. Ishibashi, S. Keller, C. Moe, P. Cantu, T.M. Katona, D.S. Kamber, Y. Wu, E. Letts, S.A. Newman, S. Nakamura, J.S. Speck, U.K. Mishra, S.P. DenBaars, T. Onuma, S.F. Chichibu, Vacancy-oxygen complexes and their optical properties in AlN epitaxial films studied by positron annihilation, *Journal of Applied Physics*, 105 (2009) 054501.

Chapter 5

Spectrophotometry of Reactive Assistive IBSD Grown AlN Thin Films

Investigations on optical band-gap (E_g) and associated energy tails of reactive assistive IBSD grown AlN thin films on Si(100) are reported in this chapter. The absorption spectra were collected in near normal incidence geometry in diffuse reflectance mode. Variation of absorption coefficient (α) with photon energy ($h\nu$) is presented as a function of growth temperature. Important features of α vs. $h\nu$ are described by classifying it into three categories. E_g , Urbach energy tails (E_u) and weak absorption energy tails (E_t) are determined from respective regions of α vs. $h\nu$ plot. An analytical approach used to determine the refractive index (n) and extinction coefficient (k) of AlN thin films grown on Si(100) at different substrate temperatures is presented.

The electrical characterization of AlN has been difficult due to low intrinsic carrier concentration, presence of deep native defects and impurity energy levels in its microstructure. In view of this, optical band-gap energy (E_g) of as grown AlN thin films having different microstructures were investigated using an UV-VIS spectrophotometer (Jasco V650, Japan). Bare Si(100) substrate was used as reference for correcting the base line of all reflectance spectra collected in a wavelength (λ) range of 200 nm to 900 nm. Important optical parameters are calculated by analyzing the diffuse reflectance spectra obtained at near normal incidence geometry. The underlying dependence of microstructure on substrate

temperature and the evolution of E_g were addressed by assessing Urbach energy tail (E_u) and associated weak absorption tail energy (E_t). Difference between specular and diffused reflectance, Kubelka-Munk (K-M) theory and its applicability in the case of thin films are also discussed subsequently.

5.1 Reflection and Its Analysis

In practice, no specimen can be infinitely thin. Thus it becomes necessary to collect the reflection spectrum to determine optical properties of a film by analyzing the reflected light. There are two limiting cases as shown in figure 5.1:

(I). Specular Reflection: “*Mirror-type*” surfaces (surface roughness $< 2\text{\AA}$) show ideal regular reflection (also known as, mirror reflection and surface reflection) according to the laws of geometric optics. Such a behavior is described by the *law of reflection*, which states that the direction of incoming light (the incident ray) and the direction of outgoing reflected light (the reflected ray) subtends the same angle with the surface normal, thus the angle of incidence equals the angle of reflection ($\theta_i = \theta_r$) as shown in figure 5.1(A). Here, the incident, normal, and reflected directions are co-planar. Regularly reflected light is thus most intense in forward directions as light from a single incoming direction is reflected into a single outgoing direction. The reflecting power is called ‘*reflectivity*’. The reflectivity is high in the spectral range where absorption is high.

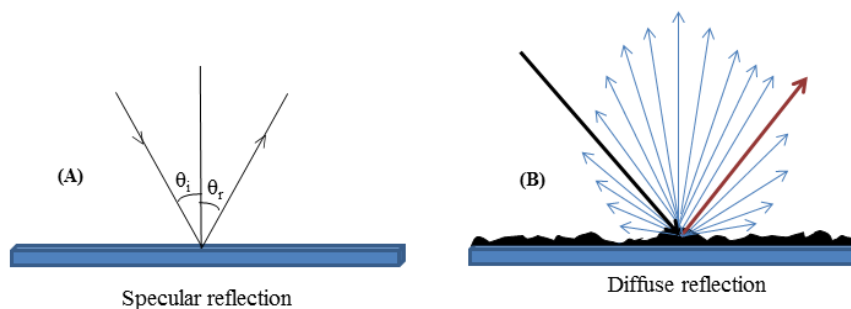


Figure 5.1 Reflection from a surface; (A) specular reflection, (B) Diffuse reflection.

(II). Diffuse reflectance: ‘*Mat*’ surfaces (surface roughness $> 2\text{\AA}$) reflect the light diffusely. Ideal diffuse reflection is defined by an angular distribution of the reflected radiation that is independent of the angle of incidence as shown in figure 5.1(B). This distribution of reflected light is a result of multiple scattering. The causes of the redirection of the light are regular reflection, refraction, and diffraction ‘inside’ the sample. Under the conditions of ideal diffuse reflection, these phenomena are not separable. In this case, the reflecting power is called *reflectance*. Generally, reflectance is low in the spectral range where absorption is high.

In the context of thin films, literature reports following two conditions for delineating the specular or diffuse reflectance and treat the reflectance data suitably [3, 4].

- (i). The reflectance (R) should lie in the range $0.2 < R < 0.7$.
- (ii). Particle size on the surface (or surface roughness, r) and wavelength (λ) of incident light should follow the condition $2\pi r \ll \lambda$.

Thus in diffuse reflectance, reflected light is analysed and attempts have been made to relate the reflectance to the absorption coefficient of the specimen under

investigation. In the case of thin films thicker than 1000 Å and having surface roughness $> 2\text{Å}$, besides absorption by the sample, scattering needs to be considered. Scattering theories such as Rayleigh or Mie theory describe the cases requiring wavelength of light to be long as compared to the size of the scattering center or particles to be spherical. Most models treat the samples as parallel sheets of homogeneous layers (continuum theories); while some statistical models address the specimen in terms of an assembly of particulates [5]. In this context, Schuster-Kubelka-Munk (K-M) theory happens to be the most widely used formalism [6]. Initiated in 1931, the K-M formalism addresses the optical properties of coatings and paints. The K-M function in diffuse reflectance spectroscopy is analogous to absorbance function in transmission spectroscopy [6]. There are treatments on finite and infinite thickness coatings where either scattering (no absorption, white paint) or mere absorption (no scattering, glossy coatings) is discussed. The deliberations indicate that reflectance depends solely on the ratio of absorption (K) and scattering (S) coefficients as following:

$$\frac{K}{S} = \frac{(1-R)^2}{2R} = F(R) \quad (1)$$

The function $F(R)$ is called K-M or remission function and by analogy with absorbance, it is dimensionless. It gives the correct values in certain limiting cases: For a nonabsorbing film where $K \rightarrow 0$, there is a complete reflection and $R \rightarrow 1$. For a nonscattering film $S \rightarrow 0$, there is no reflection and $R \rightarrow 0$ [4].

▪ *Applicability of K-M Function*

The motivation for transforming reflectance data into K-M function is to obtain a representation of absorption spectrum of the film. Although, it is

sometimes debated as to whether the transformation should be performed. As long as $0 < R < 1$, the conversion of reflectance into K-M function can be performed, just as absorbance can be calculated from transmittance for $0 < T < 1$. Thus the K-M function is a limiting case for the range of weak absorption. Unfortunately, most of the reports in literature are vague in specifying ‘*weak*’ or ‘*strong*’ absorption. Thus in view of these reports existing in the literature, the range $0.2 < R < 0.7$ is considered acceptable for the application of K-M formalism [6, 7].

5.2 Deposition of AlN Thin Films

AlN thin films were deposited on 10 mm X 10 mm Si (100) substrates by reactive IBSD. The base pressure of the chamber was 4×10^{-7} mbar while working pressure was maintained at 4×10^{-4} mbar during deposition. Films were grown at different substrate temperatures varying from RT to 500°C in steps of 100°C. During deposition, the required metal atom flux was provided by sputtering an Al-target (99.999% pure) with an Ar^+ ion beam extracted from a 6 cm RF ion source with an energy of 500 eV. Concomitantly, an End-Hall type ion source was used to deliver an assistive reactive flux consisting of N^+/N_2^+ ions at 90 eV directly to the substrate surface. The thickness of the films was measured ex-situ using a surface profilometer (Veeco, USA) and estimated to be ~114 nm for all the samples.

5.3 Calculation of Optical Band Gap Energy (E_g)

The fundamental absorption in a material takes place either by excitonic process or by band-to-band transition during interaction of photon with matter [7]. Herein, two types of transitions are possible at this fundamental edge: direct and indirect. Both these transitions involve interaction of photon with an electron in

the valence band which subsequently gets excited into the conduction band across the fundamental band gap [8, 9]. However, in the case of an indirect transition, simultaneous interaction with lattice vibration also takes place. The appearance of optical band-gap in thin films is greatly affected by its microstructural constituents like short-range co-ordination, crystallite size and type of defects present in the system etc.

The optical system under investigation is constituted of a thin and homogeneous film of AlN deposited on opaque Si (100) substrate. Thickness of the substrate was several orders of magnitude higher than that of the film. Electromagnetic waves were incident from the spectrophotometer on to the film surface in near normal incidence geometry. Diffused reflectance spectra thus collected were analyzed using K-M formalism. Herein, K-M function $F(R)$ at any wave length is given by equation (1) [6, 10]. $F(R)$ values thus obtained were further converted into linear absorption coefficient (α) by the following relation [11]:

$$\alpha = \frac{F(R)}{t} \quad (2)$$

Where 't' is the thickness of the film which is ~114 nm for all the samples.

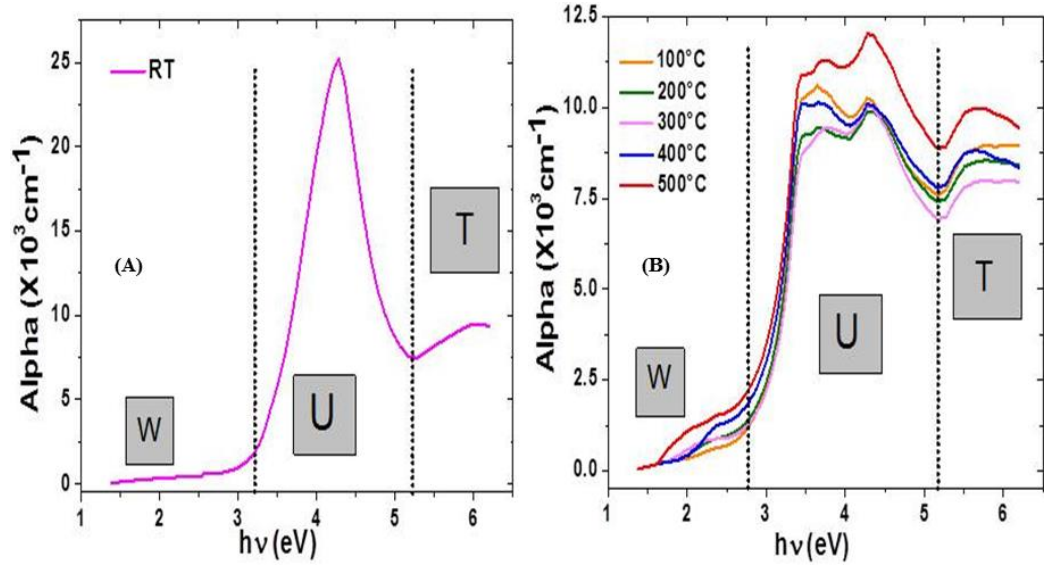


Figure 5.2 Absorption coefficient (α) as a function of photon energy ($h\nu$), (A) at RT, (B) 100°C to 500°C substrate temperatures. These plots are classified into three regions. In each region, α depends upon $h\nu$ differently.

The α vs $h\nu$ behaviour of AlN thin films is shown in figure 5.2. In figure 5.2(A), variation of α with $h\nu$ for the samples deposited at RT is displayed. This is found to be quite different from those deposited at higher substrate temperatures as shown in figure 5.2(B). Here, it should be noticed that reactive assistive IBSD has inherent ion induced effects on the microstructure of grown films. In addition, AlN being an ionic/covalent solid becomes vulnerable to incorporate defects during deposition. These native defects in film microstructure form their localized tail states between valence and conduction band which give rise to a phenomenon called band-tailing. Here, band-tailing means that the edges of valence and conduction band are no longer sharp having well-defined cut-off energy and their electronic state density falls sharply with energy away from the band edges [2]. Thus the plot α vs $h\nu$ should be analysed carefully to account for these band tails in III-nitride semiconductors. Keeping the above discussion in mind, figures

5.2(A) and 5.2(B) can be classified into three types of absorptions [2, 12]. First is the region of weak absorption tails (WAT) which is attributed to the small optical absorption (α) governed by the optical transitions from one tail state to another tail state. These localized tail states in amorphous semiconductors arise from defects generated disorder. Second is the region-U where α is controlled by the transitions from the localized tail states above the valence band to the extended states in the conduction band and/or from the extended states in the valence band to the localized states below the conduction band [2, 12]. In this region, the spectral dependence of α follows the Urbach rule. Third is the region-T which represents the range of α governed by the optical transitions from one extended state to another extended state. Most of the amorphous and nanocrystalline semiconductors follow Tauc's relation in this region. Thus E_g is calculated by Tauc's plot in this region-T.

In the view of above discussion, the general form of the absorption coefficient α in the region-T of figure 5.2(A) and 5.2(B) can be described by the Tauc's relation:

$$(\alpha h\nu)^{1/m} \sim A(h\nu - E_g) \quad (3)$$

Where, E_g is the optical band gap energy. A refers to a proportionality constant and m takes different values which correspond to different transitions [9]. Since AlN is known to be a direct band-gap material, value of m is taken to be $\frac{1}{2}$ for this direct allowed transition. Thus, E_g was determined by plotting ' $(\alpha h\nu)^2$ ' as a function of photon energy ' $h\nu$ ' and extrapolating the linear region of these plots to the x-axis as shown in figure 5.3.

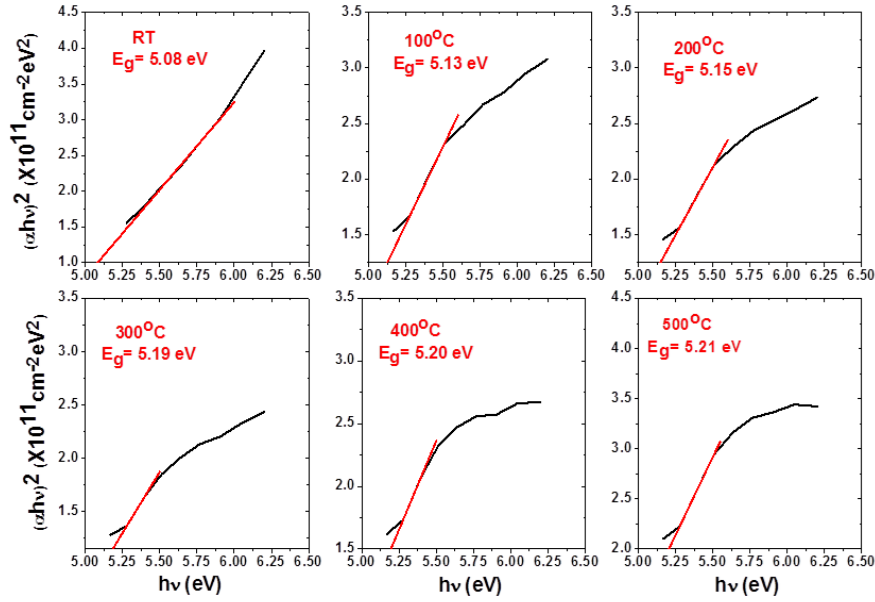


Figure 5.3 Tauc's plots to estimate the optical band gap energy at each substrate temperature. At RT, E_g is found to be 5.08 eV. As the temperature of the substrate is increased to 100°C, E_g increases subsequently to 5.13 eV. Maintaining this rising trend with further increase in substrate temperature E_g becomes 5.19 eV, 5.20 eV and 5.21 eV, respectively, for 300°C, 400°C and 500°C.

It is observed from the graphs that at RT, E_g is found to be 5.08 eV. As the temperature of the substrate is increased to 100°C, E_g increases subsequently to 5.13 eV. Maintaining this rising trend with further increase in substrate temperature E_g becomes 5.19 eV, 5.20 eV and 5.21 eV, respectively, for 300°C, 400°C and 500°C. Although, the variation in E_g is very small and can be approximated to the first decimal place i.e. 5.1 eV for samples grown from RT to 200°C and 5.2 eV for samples grown from 300°C to 500°C. But to understand the ~meV contribution from region-U and region-WAT, as calculated values were used. Keeping this in mind, it is observed that E_g experiences an increase in its values as the temperature of the substrate increases from RT to 500°C during deposition resulting in simultaneous increase in crystalline fraction of AlN. This reduction in E_g to ~5.2 eV of reactive IBSD grown AlN thin films from the ideal

value of 6.2 eV for single crystal AlN, can be elucidated by resorting to the concept of Urbach tails [13].

5.4 Determination of Urbach (E_u) and Weak Absorption Tail Energy (E_t)

Generally, in optical absorption, near band edges, an electron from the top of the valence band gets excited into the bottom of the conduction band across the band gap [13]. During this transition process, if these electrons encounter disorder in the form of defects induced localized tail states, the density of electronic states in valence and conduction bands $\rho(h\nu)$, where $h\nu$ is the photon energy, tails into the energy gap. This tail of $\rho(h\nu)$ extending into the energy band gap is termed as Urbach tail. Consequently, absorption coefficient $\alpha(h\nu)$ also tails off in an exponential manner and the energy associated with this tail is referred to as Urbach energy and can be calculated by the following equation:

$$\alpha(h\nu) = \alpha_0 \exp\left(\frac{h\nu}{E_u}\right) \quad (4)$$

Where α_0 is a constant, ' $h\nu$ ' is the photon energy and E_u is the Urbach energy [14, 15]. In figure 5.2(A) and 5.2(B), the region-U is the representative of this phenomenon and corresponding range of α follows equation (4). The Urbach energy is estimated by plotting $\ln(\alpha)$ vs. $h\nu$ and fitting the linear portion of the curve with a straight line. The reciprocal of the slope of this linear region yields the value of E_u . The films deposited at RT are amorphous as these films have defects produced during reactive IBSD where thermal activation is insufficient to induce crystallization and E_u is estimated to be 310 meV. As the substrate temperature is raised to 100°C and 200°C, E_u reduces to 303 meV and 300 meV, respectively. This indicates that the perpetual shuffling motion of atoms in

randomly stacked polyhedra in an amorphous matrix becomes restricted with increase in substrate temperature. Such limited motion results in reduced number of vibrational energy levels for a given electronic state which diminishes the multiplicity in transition probability and contracts the Urbach tailing resulting in lower E_u . As the substrate temperature was increased to 300°C, a structural transition from amorphous to nanocrystalline state occurs. In this case, spatial variation with respect to bonding and local coordination, which is typical of short range order, takes place. This ensuing disorder density inherent to nanocrystalline state results in a net value of $E_u = 293$ meV. At 400°C, the structure of the film becomes microcrystalline which persists when substrate temperature further increased to 500°C. At these substrate temperatures, E_u values are found to be nearly same, 290 meV and 289 meV, respectively. This behaviour of E_u with increasing substrate temperature falls in-line with that of E_g calculated in section 5.6. As the temperature of the substrate increases, film becomes more crystalline with increased band gap and reduced Urbach tail. These values of E_g and E_u are listed in table 5.1 at each substrate temperature and can be explained as following.

Table 5.1 Comparison of optical band gap energy (E_g), Urbach energy (E_u) and WAT energy (E_t) at different substrate temperatures.

Substrate Temperature (°C)	E_g (in eV)	E_u (in meV)	E_t (in meV)
RT	5.08	310	551
100	5.13	303	524
200	5.15	300	521
300	5.19	293	490
400	5.20	290	485
500	5.21	289	477

It is a well-known fact that ion beam assisted deposition generates near surface defects during deposition process. When an assistive ion with few tens of eV energy impinges on the surface of a thin film, a shallow penetration of the surface takes place and during the course of interaction with film-surface atoms, it transfers its energy to produce more number of knock-ons. Thus collision cascade propagates in the near surface region [16]. When the transferred energy is not sufficient to initiate a knock on, it gets absorbed in the form of lattice vibration and creates sub-surface defects such as vacancies, vacancy-interstitial pairs and antisites. Hence ion bombardment induced defects at the surface and sub-surface constitutes a source of disorder in the film [17]. It is generally a well-recognized fact that AlN possess four residual point defects in its microstructure which are aluminum vacancy (V_{Al}), nitrogen vacancy (V_N), aluminum-antisites (Al_N) and nitrogen-antisites (N_{Al}) [18]. These defects introduce their own electronic states in the band gap and significantly alter the optical response of AlN. In figure 5.2(B), a much lower absorption peak at 2.8 eV to 3 eV is noticed which is not present in figure 5.2(A). This peak is likely owing to formation of V_N as proposed by Cox et al and Yim et al [19, 20]. These V_N forms a donor triplet just below the conduction band at 200 meV, 500 meV and 900 meV [19]. This feature indicates that for the films deposited at temperatures in the range 100°C to 500°C, V_N plays a significant role in deciding E_g but not for the films deposited at RT. Another point worth noticing here is that aluminum has very high affinity towards oxygen as compared to nitrogen. This becomes the genesis of oxygen related defects and defect complexes which are important intrinsic defects in AlN [21]. This oxygen

in AlN matrix not only substitutes easily into nitrogen-sites but also forms $V_{Al} - nO_N$ (where $n = 1, 2$) type complexes and forms deep donor levels due to wide band gap of AlN. In α vs. $h\nu$ curve shown in figure 5.2(A) and 5.2(B), a peak is noticed lying between 3.5 eV to 5 eV. This peak is assigned to oxygen absorption region as originally reported by Pastrnak and Roskovcova [22]. Thus it can be concluded that for the films grown at RT, only oxygen related defects and defect complexes dominate. While for the films grown at higher temperatures from 100°C to 500°C, V_N , O_N and $V_N - nO_N$ (where $n = 1, 2$) are the most probable and dominating defects.

In addition to above explained behaviour of α with $h\nu$, there exists a region-WAT in figure 5.2(A) and 5.2(B). Variation of α in this region is attributed to tail-to-tail state transitions as explained in section 5.3 and is governed by the following equation:

$$\alpha(h\nu) = \alpha_o \exp\left(\frac{h\nu}{E_t}\right) \quad (5)$$

Where E_t characterizes the equivalent band tail contribution arising from weak absorption tails [12]. Calculated values of E_t are listed in table 5.1 and it is found that $E_t > E_u$ at each substrate temperature. As a matter of fact, with regard to the manifestation of optical properties of material, all kinds of disorders, irrespective of their origin, exhibit cumulatively additive property [22]. Thus to estimate the net contribution of structural and thermal disorder in film microstructure to account for the reduction in optical band gap of reactive IBSD grown AlN thin film, E_u and E_t can be added. If we plot E_g vs. $E_u + E_t$, it is found to be linear as is shown in figure 5.4. When fitted with a straight line, its intercept gives the

maximum possible value of $E_g = 6.24$ eV which can be considered to represent that value of E_g when there is no disorder in thin film microstructure.

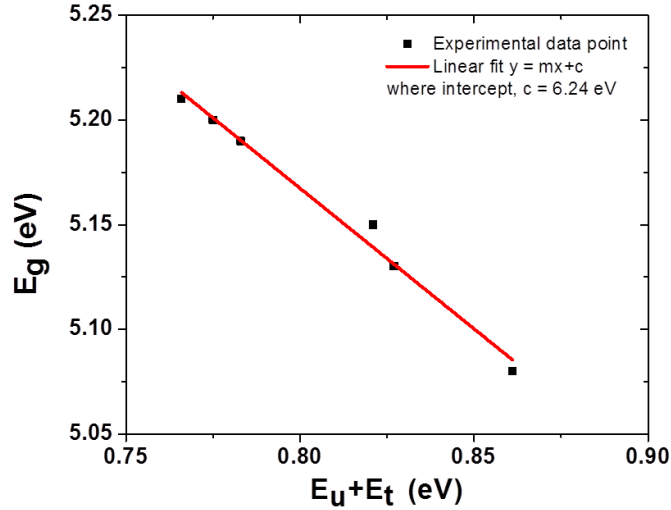


Figure 5.4 Comparative variation of E_g with net $E_u + E_t$. When fitted with a straight line, intercept of the linear fit (~ 6.24 eV) represents the optical band gap energy of the films when there is no disorder in their microstructure.

5.5 Refractive Index and Extinction Coefficient

One of the most important optical constants of a material is its refractive index (n), which in general depends on the wavelength of the light i.e. the electromagnetic wave. In materials where an electromagnetic wave can lose its energy during its propagation, n becomes complex. The real part is usually n , and the imaginary part is called the *extinction coefficient*, k . The refractive index of an optical or dielectric medium, n , is the ratio of the velocity of light c in vacuum to its velocity v in the medium; $n = c/v$. Using this and Maxwell's equations, one obtains the well known Maxwell's formula for the refractive index of a substance as $n = \sqrt{\epsilon_r \mu_r}$, where ϵ_r is the static dielectric constant or relative permittivity and μ_r the relative permeability. As $\mu = 1$ for nonmagnetic substances, one gets $n = \sqrt{\epsilon_r}$, which is very useful in relating the dielectric properties to optical properties

of materials at any particular frequency of interest. If the materials were absorbing, the refractive index (n) would have to be replaced by the complex refractive index ($n-ik$).

There are a variety of approaches that have been used to determine n and k of a thin film system eventually arriving at the same results. In the present study, conventions of Heaven et al. are followed to calculate n and k of the thin film system [23]. It is shown in figure 5.5.

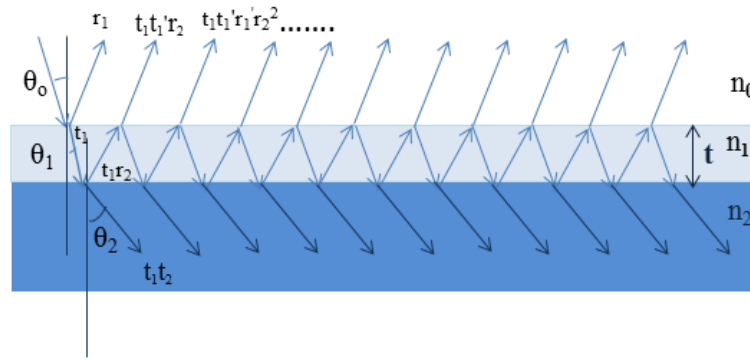


Figure 5.5 Reflection and transmission events of light traveling through a medium of refractive index n_1 deposited on the substrate of refractive index n_2 in a surrounding medium of refractive index n_0 .

Let us consider light incident on a material surface with refractive index n_1 (see figure 5.5). Some of the light will be reflected at the surface and some of the light will be transmitted into the material. The Fresnel coefficients for the amplitudes of the reflected and transmitted light traveling from n_0 (the surrounding medium) to n_1 are given in equations 6 and 7 and for light traveling from n_1 to n_0 are given by equations 8 and 9.

$$r_1 = \frac{n_0 - n_1}{n_0 + n_1} \quad (6)$$

$$t_1 = \frac{2n_0}{n_0 + n_1} \quad (7)$$

$$r_1' = \frac{n_1 - n_0}{n_1 + n_0} \quad (8)$$

$$t_1' = \frac{2n_1}{n_1 + n_0} \quad (9)$$

Above relationships are valid for light incident at normal incidences. But in case of near normal incidence also, they give a reasonably good agreement. The reflectance can then be written as:

$$R = \frac{(n_1^2 - n_2^2)^2}{(n_1^2 + n_2^2)^2} \quad (10)$$

which is readily solved for n_1 :

$$n_1 = \left[n_2 \left(\frac{1 + \sqrt{R}}{1 - \sqrt{R}} \right) \right]^{0.5} \quad (11)$$

This equation (11) is a relatively simple expression that is used to calculate n of any single layer film and is used in the present study to determine the refractive index of AlN thin films. Also, to determine that how rapidly the intensity decreases as the light passes through the material, extinction coefficient (k) was calculated from the following relation:

$$k = \alpha \frac{\lambda}{4\pi} \quad (12)$$

where α is the absorption coefficient given by equation (2).

Average values of refractive index (n_a) and extinction coefficient (k_a) obtained at each substrate temperature using equations (11) and (12) are shown in figure 5.6.

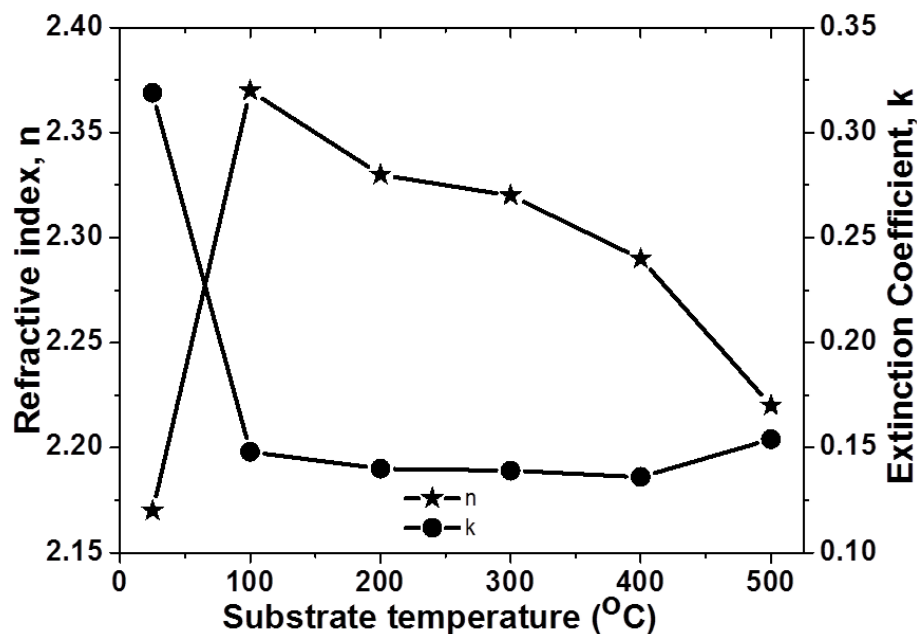


Figure 5.6 Variation of average refractive index (n_a) and extinction coefficient (k_a) of AlN thin films on Si(100) substrate with temperature.

It is observed that n possesses lowest value at RT. This implies that the film microstructure has less number of free electrons contributing to its optical response. This is possible when film microstructure has considerable amount of defects mentioned in sec. 5.6. As the temperature of the substrate was increased to 100°C, a drastic rise in n is noticed. With further increase in substrate temperature till 500°C, overall values of n are larger than that at RT. This observation indicates that the microstructure of AlN thin films deposited at higher substrate temperatures is sufficiently abundant with free electrons which can contribute to its optical activity. This also indicates that the defect density in film microstructure reduces improving their crystallographic quality. These observations fall exactly in line with corresponding behaviour of E_g , E_u and E_t which are listed in table 5.1. Larger n values at higher substrate temperatures are indicative of a lower defect density which ultimately results in higher E_g and

smaller E_u & E_t . If only n values from 100°C to 500°C are noticed, a fall is observed. This can be attributed to the increased surface roughness of these films at higher substrate temperature (Chapter 4, figure 4.3).

This behaviour of n is also corroborated by the observed values of k which correspond to the absorbing characteristics of AlN thin film's microstructure. At RT, comparatively larger defect population in film microstructure absorbs considerable amount of incident intensity and results in higher k . As the substrate temperature is increased from 100°C to 500°C, reduction in defect population results into a fall in k strengthening the observations from the variation of n with substrate temperature which are described earlier in this section.

5.6 Conclusion

AlN thin films grown by reactive IBSD on Si(100) at different substrate temperatures are studied. The changes in substrate temperature during deposition has its corresponding impact on the optical band gap as revealed by the spectrophotometric studies. The origins of variations in optical band gap were found to stem from changes in microstructure at different substrate temperatures and give rise to significant band tailing into the band gap. The sub-surface defects such as V_N , O_N and $V_{Al} - nO_N$, (where $n = 1, 2$) created by the assisted ion flux and preferable interaction of aluminum and oxygen during deposition of thin films, manifest as Urbach energy tail in the band-gap. The extent of increase in Urbach energy along with WAT energy can be used as a measure of disorder in the films. These observations indicate that a fine control over energy band-gap in combination with the temperature induced microstructure of the film can

favorably be utilized to modify the refractive index (n) and extinction coefficient (k) of AlN films to harness it in optical applications.

References

- [1] D. Malacara, Handbook of Optical Engineering, CRC Press, 2001.
- [2] J. Singh, Optical Properties of Condensed Matter and Applications, Wiley, 2006.
- [3] O.S. Heavens, Optical Properties of Thin Solid Films, Dover Publications, 1991.
- [4] B.C. Gates, H. Knoezinger, F.C. Jentoft, Advances in Catalysis, Elsevier Science, 2009.
- [5] N.T. Melamed, Optical Properties of Powders. Part I. Optical Absorption Coefficients and the Absolute Value of the Diffuse Reflectance. Part II. Properties of Luminescent Powders, Journal of Applied Physics, 34 (1963) 560-570.
- [6] P.a.M. Kubelka, F, Ein Beitrag zur Optik der Farbanstriche, Z. Tech. Phys. (Leipzig), 12 (1931) 593-601.
- [7] J.I. Pankove, Optical Processes in Semiconductors, Prentice-Hall, Eglewood Cliffs, NJ, 1971.
- [8] K.S. Kim, Y.C. Jang, H.J. Kim, Y.C. Quan, J. Choi, D. Jung, N.E. Lee, The interface formation and adhesion of metals (Cu, Ta, and Ti) and low dielectric constant polymer-like organic thin films deposited by plasma-enhanced

- chemical vapor deposition using para-xylene precursor, *Thin Solid Films*, 377–378 (2000) 122-128.
- [9] N.F.M.a.E.A. Davis, *Electronic Processes in Nanocrystalline Materials*, Clarendon press, oxford, 1979.
- [10] V. Senthilkumar, P. Vickraman, R. Ravikumar, Synthesis of fluorine doped tin oxide nanoparticles by sol–gel technique and their characterization, *Journal of Sol-Gel Science and Technology*, 53 (2010) 316-321.
- [11] C. Aydın, M.S. Abd El-sadek, K. Zheng, I.S. Yahia, F. Yakuphanoglu, Synthesis, diffused reflectance and electrical properties of nanocrystalline Fe-doped ZnO via sol–gel calcination technique, *Optics & Laser Technology*, 48 (2013) 447-452.
- [12] S. Adachi, *Optical Properties of Crystalline and Amorphous Semiconductors: Materials and Fundamental Principles*, Springer US, 2012.
- [13] K. Boubaker, A physical explanation to the controversial Urbach tailing universality, *The European Physical Journal Plus*, 126 (2011) 1-4.
- [14] B. Choudhury, B. Borah, A. Choudhury, Extending Photocatalytic Activity of TiO₂ Nanoparticles to Visible Region of Illumination by Doping of Cerium, *Photochemistry and Photobiology*, 88 (2012) 257-264.
- [15] P. Sigmund, Theory of Sputtering. I. Sputtering Yield of Amorphous and Polycrystalline Targets, *Physical Review*, 184 (1969) 383-416.
- [16] K.H. Müller, Model for ion-assisted thin-film densification, *Journal of Applied Physics*, 59 (1986) 2803-2807.

- [17] T.L. Tansley, R.J. Egan, Point-defect energies in the nitrides of aluminum, gallium, and indium, *Physical Review B*, 45 (1992) 10942-10950.
- [18] G.A. Cox, D.O. Cummins, K. Kawabe, R.H. Tredgold, On the preparation, optical properties and electrical behaviour of aluminium nitride, *Journal of Physics and Chemistry of Solids*, 28 (1967) 543-548.
- [19] W.M. Yim, R.J. Paff, Thermal expansion of AlN, sapphire, and silicon, *Journal of Applied Physics*, 45 (1974) 1456-1457.
- [20] M. Kazan, B. Rufflé, C. Zgheib, P. Masri, Oxygen behavior in aluminum nitride, *Journal of Applied Physics*, 98 (2005) 103529.
- [21] H. Morkoç, *Handbook of Nitride Semiconductors and Devices, Materials Properties, Physics and Growth*, Wiley, 2009.
- [22] J.Pasternak and Z. Roskovcova, Optical absorption end of AlN single crystals, *Phys. Status Solidi*, 26 (1968) 591.
- [23] O.S. Heavens, *Optical Properties of Thin Solid Films*, Dover Publications, 1991.

Chapter 6

Piezoelectric Properties of Reactive Assistive IBSD Grown AlN Thin Films

Piezoelectric properties of a-axis oriented AlN thin films measured using three different techniques, namely, piezo force microscopy (PFM), X-ray diffraction (XRD) and capacitance-voltage (C-V), are presented. Different variants of AlN/Ti/Si(100) and Ti/AlN/Ti/Si(100) heterostructures were fabricated by varying thickness of AlN thin film. Analytical procedures used to extract longitudinal piezoelectric coefficient $d_{(33\text{eff})}$ are discussed. In PFM, phase and amplitude data is used to generate piezo response loops. XRD measurements allowed calculations of piezoelectric strains from the FWHM of rocking curves obtained at each applied DC voltage. A methodology used to calculate the $d_{(33\text{eff})}$ from C-V measurements is presented. A physical model to account for enhanced piezoelectric response of reactive assistive IBSD grown a-axis oriented AlN thin films is also proposed.

Piezoelectricity is a linear interaction between mechanical and electrical responses of crystal systems which do not possess a center of inversion. It strongly depends on the symmetry of the crystal. A crystal having sufficiently low symmetry produces electric polarization under the influence of external force. This class of materials deform when placed in an electric field. Such materials exhibiting this electromechanical coupling are classified to be *electroelastic*. Electroelastic materials have been used for a long time to fabricate several electromechanical devices. Examples include transducers for converting electrical

energy into mechanical energy or vice versa, resonators and filters for frequency control and selection for telecommunication, precise timing and synchronization, and acoustic wave sensors.

6.1 The Piezoelectric Effect

The word *Piezoelectricity* originates from the Greek language meaning ‘*electricity by pressure*’. This name was proposed by Hankel in 1881 to name the phenomenon discovered a year before by the Pierre and Jacques Curie brothers. In general, piezoelectricity can be defined as, ‘*the ability of a material to generate an electric charge in response to an applied mechanical stress*’. All the dielectric materials that belong to the class of noncentrosymmetric crystals are classified as *piezoelectric materials*. The piezoelectric effect can be classified into direct and converse piezoelectric effects as following [1]:

(I). Direct Piezoelectric Effect: Generation of electricity on the application of an external mechanical stress. It is shown in figure 6.1(A).

(II). Converse Piezoelectric Effect: Production of stress and/or strain when an electric field is applied. It is also known as indirect or reverse piezoelectric effect as shown in figure 6.1(B).

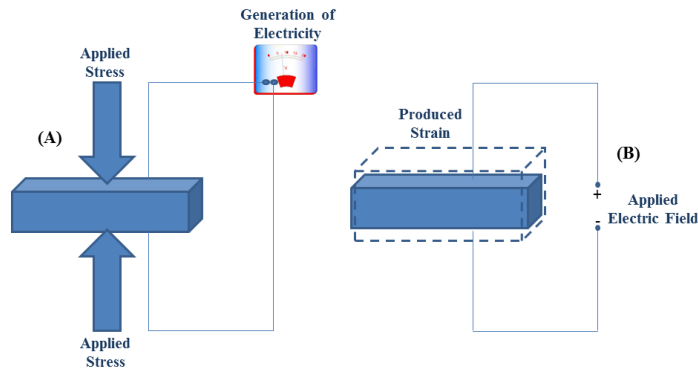


Figure 6.1 (A) Direct piezoelectric field, (B) Converse piezoelectric field.

Direct and converse piezoelectric effects have many applications as the effects involve conversion of mechanical energy into electrical energy and vice versa. Applications include generation and detection of ultrasonic waves, pressure sensors, and actuators in engineering and medical fields. Figure 6.2 schematically displays manifestation of piezoelectric effect in non-centrosymmetric crystals [2].

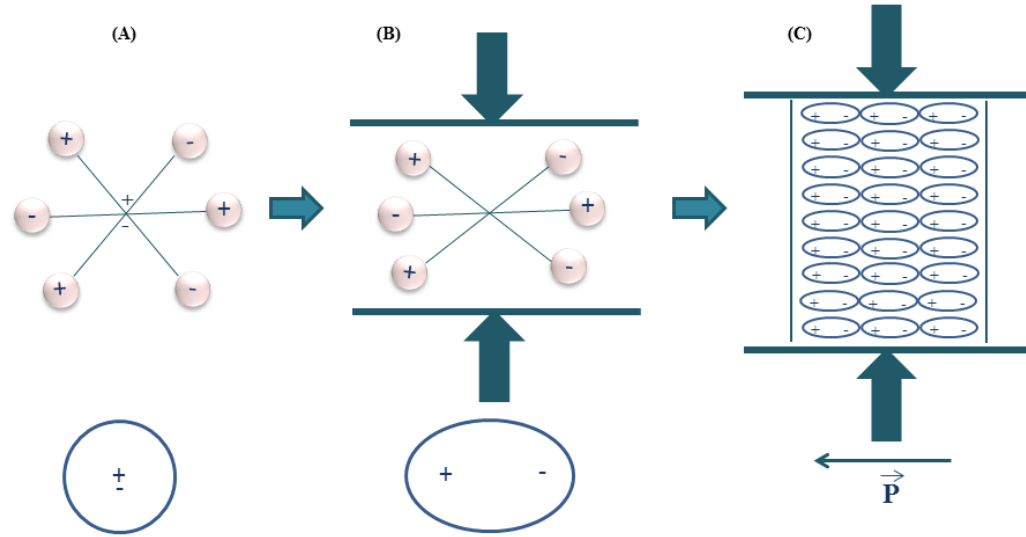


Figure 6.2 Molecular model of piezoelectricity, (A) center of gravity of all negative and positive charges of each molecule coincides, (B) generation of little dipoles due to separation of gravity centers of negative and positive charges, (C) generation of linked charges and hence the polarization on the surface.

6.2 Mathematical Formulation of Piezoelectricity: *The Piezoelectric Coefficients*

Generally, sensitivity of a piezoelectric material is expressed in terms of *piezoelectric coefficients*. These piezoelectric coefficients relate the input and corresponding output parameters of a material exhibiting piezoelectricity [3].

In direct piezoelectric effect, input is mechanical energy and output is electrical energy. This mechanical input can be in the form of external stress (X) or strain (x). At the same time, consequent electrical output can be in the form of

surface charge density (D or P), electric field (E), or voltage (V). This is shown in figure 6.3 [4].

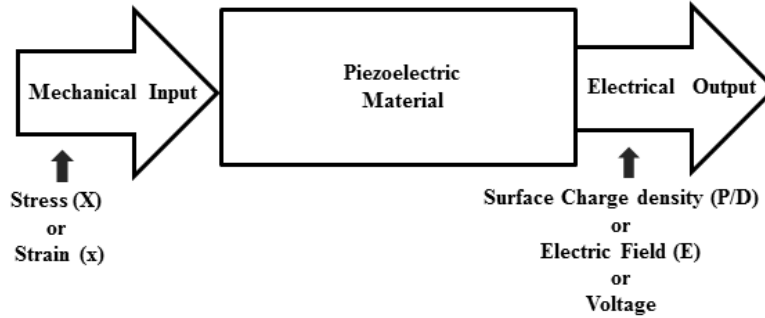


Figure 6.3 Input and output scheme of direct piezoelectric effect.

The equations which relate the mechanical input strain ' x ' to the electrical output (D/E), in direct piezoelectric effect, are:

$$D = ex \quad (1)$$

or

$$E = hx \quad (2)$$

and the equations that relate the mechanical input stress ' X ' to the electrical output (D/E) are:

$$D = dX \quad (3)$$

or

$$E = gX \quad (4)$$

e , h , d and g are the piezoelectric coefficients which describe the direct piezoelectric effect.

Similarly, in converse piezoelectric effect, input is electrical energy and output is mechanical energy. The electrical input can be in the form of surface charge density (P/D) or electric field (E) or voltage (V), and the mechanical

output can be in the form of strain (x) or stress (X) on a material which is shown in figure 6.4 [4].

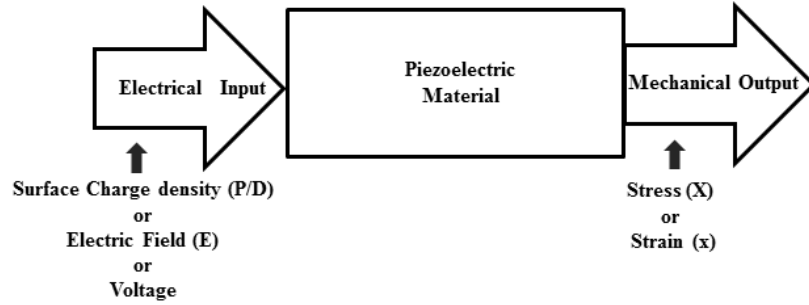


Figure 6.4 Input and output scheme of converse piezoelectric effect.

Piezoelectric coefficients which describe the converse piezoelectric effect are denoted by e^* , d^* , h^* , and g^* . They are defined by the relations:

$$X = e^*E \quad (5)$$

$$x = d^*E \quad (6)$$

$$X = h^*D \quad (7)$$

$$x = g^*D \quad (8)$$

As $D = \epsilon E \quad (9)$

The piezoelectric coefficients are related with each-other as following:

$$h = e/\epsilon; h^* = e^*/\epsilon \quad (10)$$

and

$$g = d/\epsilon; g^* = d^*/\epsilon \quad (11)$$

Thermodynamically it can be shown that,

$$d = d^*, g = g^*, e = e^* \text{ and } h = h^* \quad (12)$$

Due to ease of measurement, piezoelectric coefficient ' d ' is the most popular to describe the piezoelectric sensitivity of a material [4].

6.3 Tensor Form of Piezoelectric Coefficient ‘ d ’

All the piezoelectric coefficients explained in the above sections are tensors as they relate vectors and tensors. In order to represent them as tensors, figure 6.5 shows a right-handed co-ordinate system. Directions 1, 2 and 3 represent the X, Y and Z axes respectively, whereas 4, 5 and 6 represent the anticlockwise rotations about the three X, Y and Z axes respectively [4, 5].

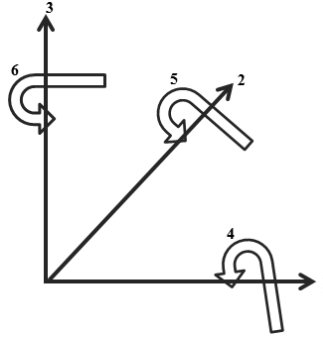


Figure 6.5 Right-handed Cartesian co-ordinate system used in tensor representation of piezoelectric coefficients.

In direct piezoelectric effect, polarization D is related to applied stress X by equation (3) as following:

$$D = dX$$

Where the piezoelectric coefficient ‘ d ’ can be expressed as a tensor of third rank as following:

$$\begin{pmatrix} D_1 \\ D_2 \\ D_3 \end{pmatrix} = \begin{pmatrix} d_{11} & d_{12} & d_{13} & d_{14} & d_{15} & d_{16} \\ d_{21} & d_{22} & d_{23} & d_{24} & d_{25} & d_{26} \\ d_{31} & d_{32} & d_{33} & d_{34} & d_{35} & d_{36} \end{pmatrix} \begin{pmatrix} X_1 \\ X_2 \\ X_3 \\ X_4 \\ X_5 \\ X_6 \end{pmatrix} \quad (13)$$

Thus, the piezoelectric coefficient d is represented as a 3×6 matrix. More detailed mathematical description of above expression can be found in any

standard text book on piezoelectricity [1-4]. The subscript d_{ij} implies that the electric field is applied or charge is collected in the i direction for a displacement or force in the j direction. Similarly, other coefficient matrices $[e]$, $[g]$, and $[h]$ can be obtained.

Depending on the symmetry of the piezoelectric system, all the components of the tensors defined earlier are not independent. So, the number of components in each of these tensors can be reduced. Most of the piezoelectric materials used in sensor and actuator applications are either polycrystalline or noncrystalline which are isotropic. But as they are poled in a specific direction, isotropy in their microstructure often disappears. Generally, poling direction is taken as the z -direction (direction 3). In case of piezoelectric thin films, preferred direction of texture can be considered as z -direction (direction 3). In crystallographic notation, the symmetry of such systems oriented in one unique direction is described as ∞mm . This implies that the system has ∞ fold symmetry axis along the poled or texture direction and an infinite set of reflection planes parallel to it. In this situation, the system is called as orthotropic or cylindrically symmetric. Thus, the number of independent components of piezoelectric coefficient matrices reduces enormously. The piezoelectric coefficient matrices $[d]$, $[e]$, $[h]$ and $[g]$ have only three independent components. The reduced matrices of piezoelectric coefficient ' d ' can be written as following [4, 5]:

$$[d] = \begin{bmatrix} 0 & 0 & 0 & 0 & d_{15} & 0 \\ 0 & 0 & 0 & d_{15} & 0 & 0 \\ d_{31} & d_{31} & d_{33} & 0 & 0 & 0 \end{bmatrix} \quad (14)$$

Thus, there are only three independent piezoelectric coefficients d_{15} , d_{31} and d_{33} .

6.4 Physical Significance of Piezoelectric Coefficients d_{33} , d_{31} and d_{15}

d_{33} : It is also known as *longitudinal piezoelectric coefficient*. It relates D and X by the relation:

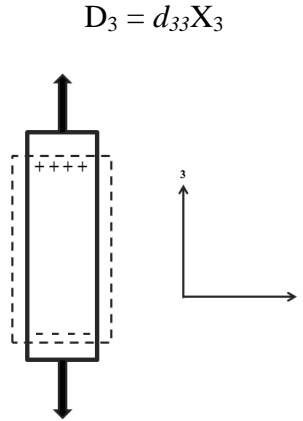


Figure 6.6 Schematic representation of longitudinal piezoelectric coefficient d_{33} .

This equation represents the direct piezoelectric effect in which the external stimulus is in the form of either tensile or compressive stress X_{33} acting along the direction 3 and the response is observed in the form of charge density D_3 developed in the same direction as illustrated in figure 6.6. This is called the *longitudinal mode* [4, 5].

d_{31} : It is also known as *transverse piezoelectric coefficient*. This coefficient relates D and X as shown in following schematic and indicated by the equation given below:

$$D_3 = d_{31}X_1$$

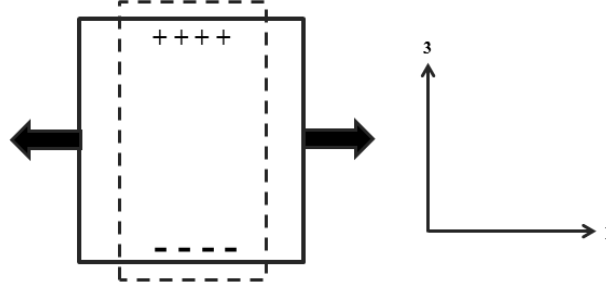


Figure 6.7 Schematic representation of transverse piezoelectric coefficient d_{31} .

This equation represents the direct piezoelectric effect in which the external stimulus is either tensile or compressive stress X_{11} along direction 1 and the response is observed in the form of charge density D_3 developed in direction 3 as illustrated in figure 6.7. This is called the *transverse mode* [4, 5].

d_{15} : It is also known as *shear piezoelectric coefficient*. It relates D and X by the following relation:

$$D_1 = d_{15}X_5$$

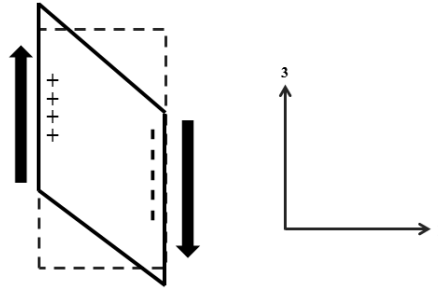


Figure 6.8 Schematic representation of shear piezoelectric coefficient d_{15} .

This equation represents the direct piezoelectric effect in which the external stimulus is the shear stress X_{13} parallel to the direction 3 and the response is observed in the form of charge density D_1 developed in direction 1 as illustrated in figure 6.8. This is called the *shear mode* [4, 5].

◆ *In the present study, longitudinal piezoelectric coefficient ' d_{33} ' of reactive assistive IBSD grown AlN thin films is determined by three different techniques which are piezo force microscopy (PFM), X-ray diffraction (XRD) and capacitance-voltage (C-V) measurements. Results and discussion pertaining to above measurements are deliberated in the following sections.*

6.5 Why Piezoelectric Aluminum Nitride (AlN) Thin Films?

Piezoelectric ultrasonic transducers (PUT) have currently found a growing interest for future innovations in non-destructive testing and proximity detection [6]. The sensitivity, response and detection limit of these transducers are largely based on material properties of thin films possessing piezoelectric characteristics. Among the host of piezoelectric materials, aluminum nitride (AlN) is emerging as a promising candidate for piezoelectric applications in its thin film form [7]. AlN is a CMOS compatible group III - nitride semiconductor with wide band-gap (6.2 eV), high coupling constant (0.25) and high Curie temperature ($T_C > 1000^\circ\text{C}$) [8]. This unique combination of properties makes AlN thin films a competitive alternate to ZnO and PZT thin film based piezoelectric transducers [9]. Most of the $d_{33(\text{eff})}$ values reported as piezoelectric coefficients of AlN thin films with c-axis orientation are comparatively smaller than those of ZnO and PZT thin films [10, 11]. In view of this, piezoelectric response of a-axis oriented AlN thin films, which so far remained unexplored, needs detailed investigation along with due considerations paid towards role of defects in their microstructure.

Wurtzite AlN is a polar material which exhibits spontaneous polarization without the presence of an external electric field [12]. Genesis of this spontaneous

polarization lies in the fact that nitrogen (N) is the smallest and most electronegative element among all V-group elements with s^2p^3 configuration and aluminum (Al) is a metal in III-group with three valence electrons having s^2p^1 configuration. Thus they form sp^3 hybridized Al^+-N^- covalent bonds in wurtzite crystal geometry which have a greater degree of ionicity than other III-V covalent bonds. Since the wurtzite AlN does not have an inversion symmetry along the c-axis, the strong ionicity of Al^+-N^- bonds result in a large macroscopic polarization in its microstructure [13]. There exists a great scientific and technical interest in this material because of its native defects prevailing in its microstructure in charged states. These intrinsic defects offer their unique characteristic properties contributing largely to the electrical and optical activities in AlN thin films. Earlier works on this subject have shown that under optimal deposition conditions, four charged native defects are likely to persist in AlN thin film microstructure. These are Al^+ -vacancy (V_{Al}^-), N^- -vacancy (V_N^+), N^- -anion on an Al^+ -cation site forming N_{Al} antisite and Al^+ -cation on an N^- -anion site forming Al_N antisite [13, 14]. Occurrence of these defects in AlN thin film microstructure strongly depends on the deposition technique. It has already been established in the previous chapters that ion beam sputter deposition (IBSD) is considered to be one of the best techniques to deposit device grade thin films [15]. In reactive assistive IBSD, metal-atom flux is provided by sputtering metal target with inert ions of higher energy and reactive assistive flux is supplied directly to the substrate surface in the form of reactive ions of mild energy. In this

process, growing film's surface is vulnerable to incorporation of defects in its microstructure due to continuous exposure to energetic reactive ions [14, 16].

Scope of this chapter is to fill some of the gaps in understanding the effect of charged native defects on piezoelectric response of a-axis oriented AlN thin films by proposing a model for charged vacancy induced enhanced polarization observed in film microstructure.

6.6 Specimen Preparation

AlN thin films were grown on Si(100) substrate with a titanium (Ti)-under layer forming AlN/Ti/Si(100) and Ti/AlN/Ti/Si(100) heterostructures by reactive assistive IBSD. For this, the chamber was pumped down to a base pressure of 3×10^{-7} mbar and films were grown at 3×10^{-4} mbar in ion assisted mode.

6.6.1 For PFM Studies: As a first step, bottom layer of Ti-electrode was grown on Si(100) substrate by sputtering a Ti-target (100mm diameter, 99.999% pure) with an Ar^+ ion beam of 500 eV. Deposition was carried out for 45 minutes and its thickness was found to be 44 nm using a surface profilometer (Dektak, Bruker, Germany). Subsequently, specimen was heated up to 400°C before depositing AlN thin film by masking with a suitable template. Aluminum (Al)-metal flux was provided by sputtering an Al-target (100 mm diameter, 99.999% pure) with an Ar^+ ion beam of 500 eV and simultaneously reactive assistive flux of 90 eV- N^+/N_2^+ ions was supplied directly to the substrate surface. Two variants of these layered structures were fabricated by varying the deposition time for AlN layer as 60 and 75 minutes. These two specimens are designated as S-60 and S-75 for

further reference. Figure 6.9 displays the layer geometry of specimens S-60 and S-75. Thickness of AlN layers in S-60 and S-75 was measured to be 235 nm and 294 nm respectively.

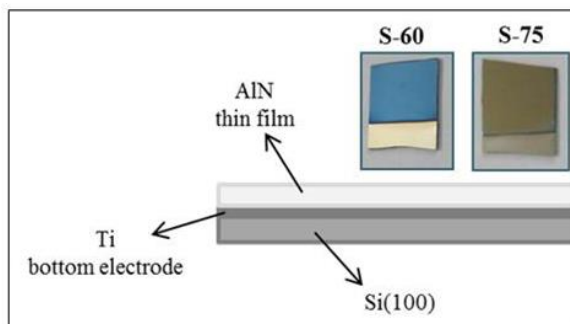


Figure 6.9 Layer geometry of AlN/Ti/Si(100) heterostructures. Inset shows the photographs of specimens S-60 and S-75.

6.6.2 For XRD and C-V Measurements: Keeping the bottom electrode of Ti and thickness of AlN thin film same, top electrode of Ti was also deposited in following two geometries:

(I). Several circular top electrodes were deposited with diameter 0.6 mm for the same deposition time of 45 minutes. Measured thickness of these electrodes was ~ 45 nm. Figure 6.10 displays the image of these Ti/AlN/Ti heterostructures deposited on Si(100) substrate.

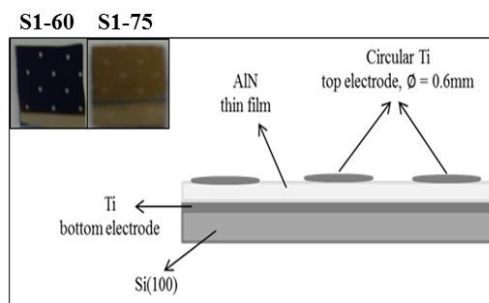


Figure 6.10 Layer geometry of Ti/AlN/Ti/Si(100) heterostructures with circular top electrodes. Inset shows the photographs of specimens S1-60 and S1-75.

(II). A square top electrode of Ti with dimensions 5 mm X 5 mm was deposited by keeping the deposition time same as 45 minutes forming the Ti/AlN/Ti heterostructures on Si(100) substrate. This is shown in figure 6.11.

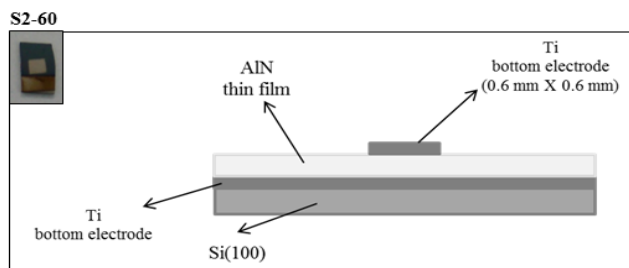


Figure 6.11 Layer geometry of Ti/AlN/Ti/Si(100) heterostructures with square top electrode. **Inset** shows the photographs of specimens S2-60.

6.7 Crystallographic Investigations on AlN Thin Films

HR-XRD patterns of the specimens S-60 and S-75 is shown in figure 6.12. Absence of peaks in the XRD pattern obtained in grazing incidence geometry (GIXRD) shows that the films were highly oriented. To confirm this, symmetric Θ - 2Θ scans were performed to detect diffraction signals arising from the lattice planes parallel to the specimen surface. These are shown in the figure 6.12(A) and 6.12(B). A single peak of wurtzite AlN (100) appears at 33.0° and 33.07° for S-60 and S-75 specimens, respectively. This indicates that both the specimens are grown with a preferred orientation along a-axis. Their degree of orientation was determined from rocking-curves which are shown in the inset of figure 6.12(A) and 6.12(B). For rocking curves, measurements were performed on AlN (100) peak at 33.0° for S-60 and 33.07° for S-75, to determine the tilt in the mosaic spreading over the film microstructure. For this, angular resolution of the X-ray optics was estimated to be of the order of 0.0003° with a standard single crystal

Si(111) reference. The full width at half maxima (FWHM) of the rocking curve is a direct measure of the relative disorientation of grains.

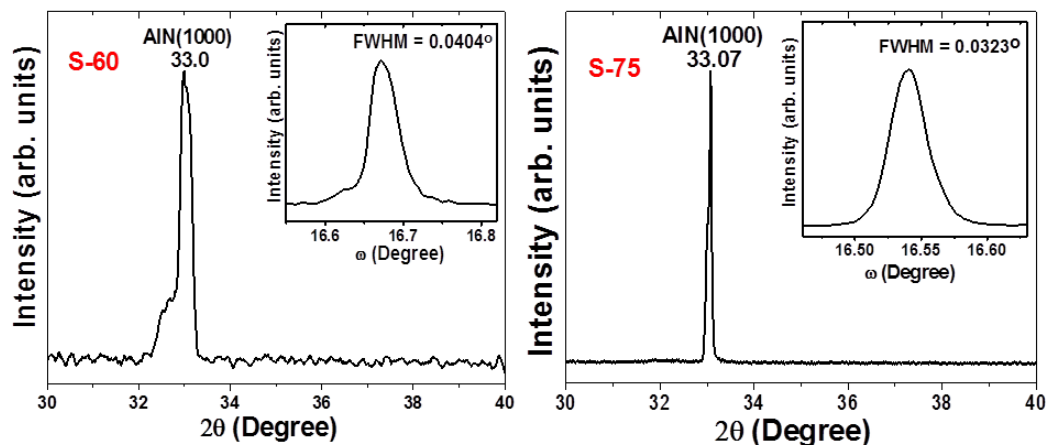


Figure 6.12 High resolution X-ray diffraction (HR-XRD) analyses of (A) S-60, and (B) S-75. **Inset** shows the rocking curve for each respective specimen.

In figure 6.12(A), FWHM of the rocking curve for S-60 is found to be 0.0404° which indicates that films are textured with very low degree of disorientation. For S-75, figure 6.12(B) shows the occurrence of compressive stress in film microstructure shifting 2θ towards higher side. Further, a decrease in mosaicity of its microstructure is evident from the appreciable reduction in FWHM of rocking curve to 0.0323° . These XRD observations clearly establish that AlN thin film becomes more crystalline and textured with increase in deposition time and hence with film thickness.

6.8 Piezo Force Microscopy (PFM) on AlN Thin Films

Piezoelectric response of S-60 and S-75 was studied using PFM which is an atomic force microscope (AFM, Dimension Edge-Bruker, USA) based technique. For this, a platinum-iridium coated conductive AFM tip (SCM-PIT) with radius of

curvature 20 nm was brought into contact with the AlN film surface and it was used as the top-electrode. A preset DC voltage from -10V to +10V was applied to the AFM tip while bottom electrode was kept grounded to establish a homogeneous external electric field within the specimen. Figure 6.13 shows a schematic view of the PFM measurement scheme. A small AC modulation voltage was superimposed to the preset DC voltage to excite and enable the piezoelectric response to result at the same frequency of oscillations as that of the applied AC voltage. Due to inverse piezoelectric effect, the surface would expand or contract and was followed by the tip in contact. Such oscillations are directly reflected in the amplitude and phase signal of the AFM probe. A lock-in amplifier was used to record these oscillations. A schematic of PFM measurements is shown in figure 6.13.

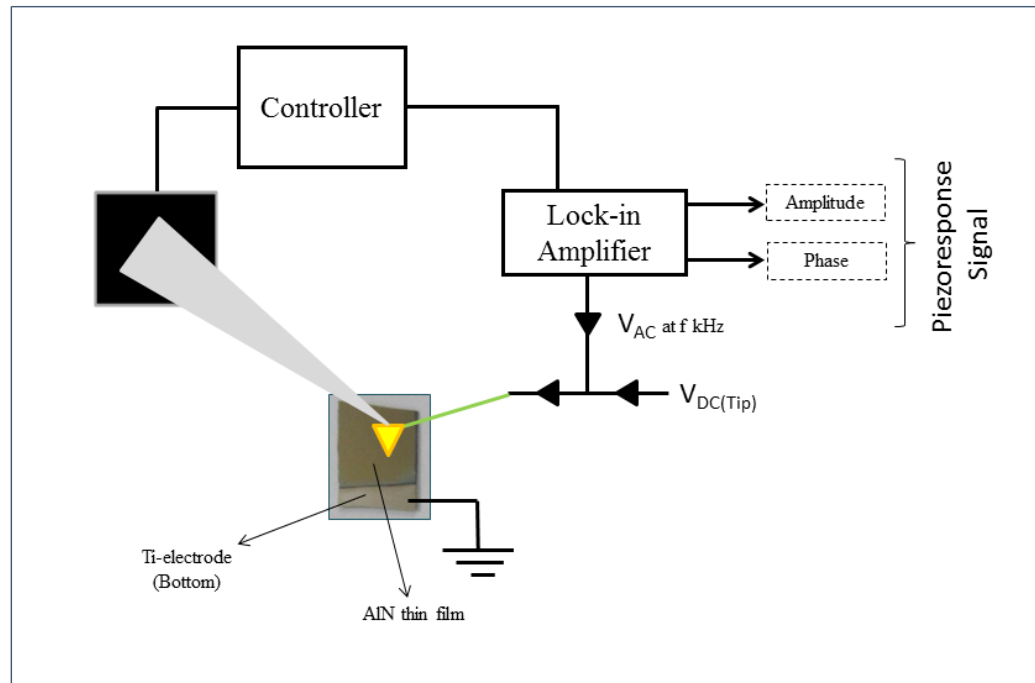


Figure 6.13 Schematic view of piezo force microscopy (PFM) measurement system.

The piezo response of specimen S-60 and S-75 could be observed from height, phase and amplitude scans shown in figures 6.14 and figure 6.15, respectively. Height scan of specimen S-60 (figure 6.14(A)) yielded a root mean square (rms) surface roughness value of 1.9 nm.

Since wurtzite AlN is a piezo as well as pyroelectric material under thermodynamic equilibrium conditions, any divergence in the spontaneous polarization induces a polarization bound surface charge segregation. The sign of this polarization induced charge is related to the orientation of the polarization and therefore to the polarity of the crystal. Thus for an epitaxial AlN thin film with Al-face polarity, the bound surface charge is negative whereas for N-face polarity, positive bound charge develops on the surface [17]. The polarity of film

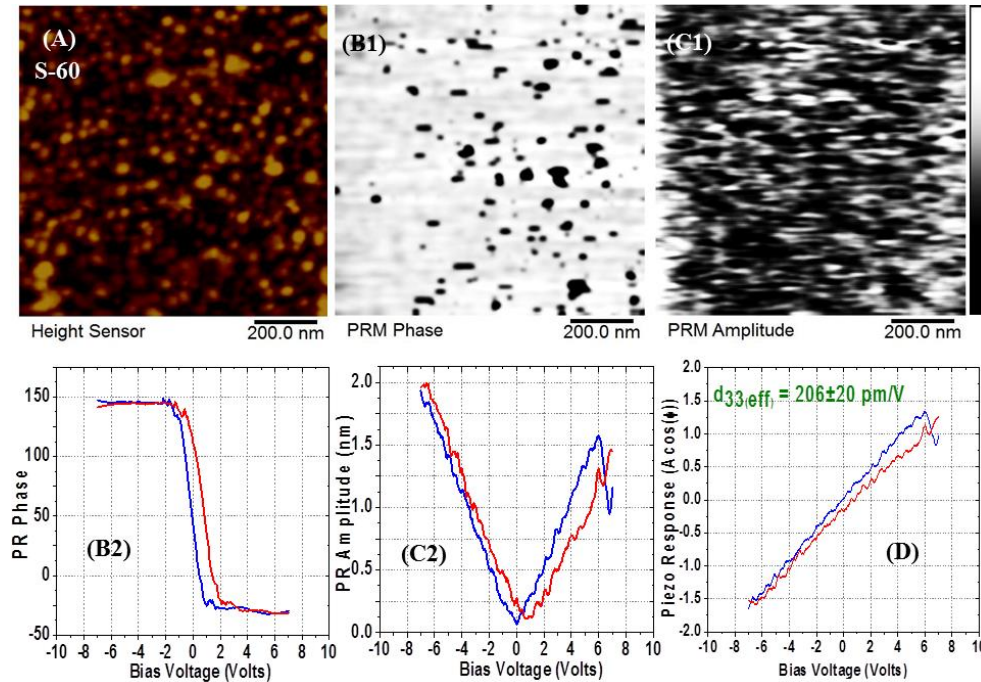


Figure 6.14 Piezo force microscopy (PFM) of sample S-60, (A) Height scan, (B1), piezo response phase image, (C1), piezo response amplitude image, (B2) electrical hysteresis, (C2) mechanical hysteresis (butterfly loop), (D) piezo response loop.

surface can then be determined by the phase of piezoelectric oscillations with modulation voltage. If piezoelectric oscillations are in-phase with modulation voltage, film surface is Al-polar. Whereas when they are out-of phase, surface of the film is N-polar. Therefore, in a PFM phase image, Al-face and N-face polarities will exhibit a phase difference of 180° and show up with opposite contrast. Thus, in phase image of S-60 (figure 6.14(B1)), the brighter regions indicate Al-polar and darker regions represent N-polar AlN.

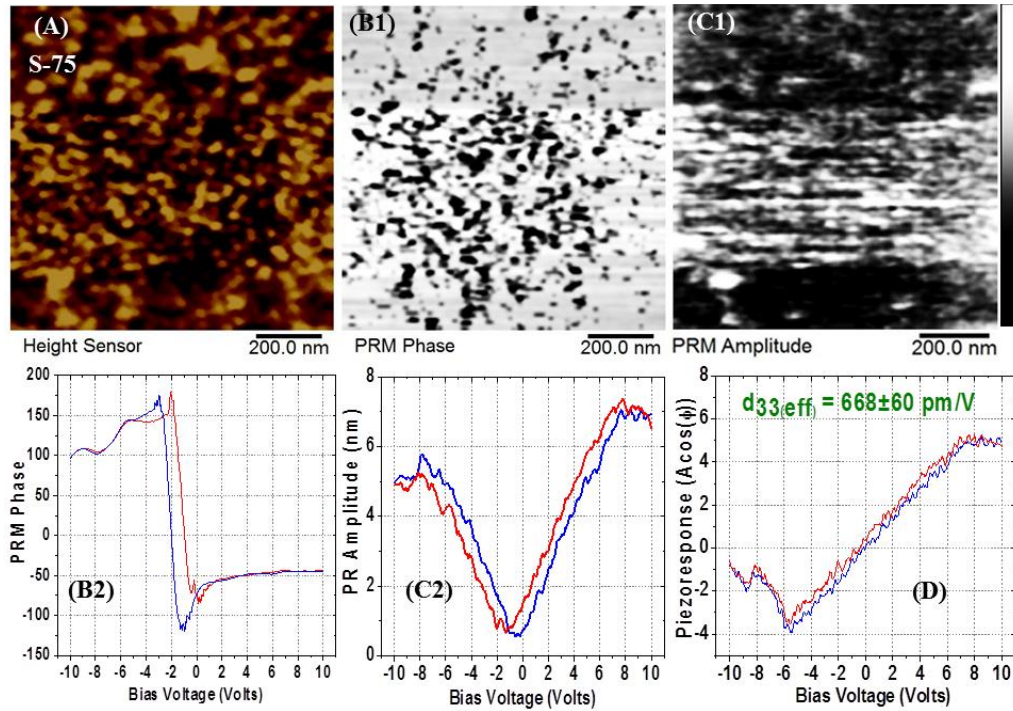


Figure 6.15 Piezo force microscopy (PFM) results of S-75, (A) Height scan, (B1), piezo response phase image, (C1), piezoresponse amplitude image, (B2) electrical hysteresis, (C2) mechanical hysteresis (butterfly loop), (D) piezoresponse loop.

Corresponding phase difference of 180° is shown in figure 6.14(B2). Piezo response amplitude image in figure 6.14(C1) infers that N-polar domains exhibit a higher magnitude of piezo response which could be possible due to larger magnitude of bound surface charge as suggested by B.J. Rodrigues et al. [17]. An

equivalent mechanical hysteresis (butterfly-loop) of S-60 is shown in Figure 6.14(C2). This piezoelectric amplitude (A) and phase (ϕ) were used further to obtain the piezo response loop for S-60 by plotting $A\cos(\phi)$ vs. V_{dc} , slope of which yielded the effective longitudinal piezoelectric coefficient ($d_{33(\text{eff})}$). Thus from the piezo response loop of S-60 shown in figure 6.14(D), $d_{33(\text{eff})}$ was determined to be 206 ± 20 pm/V. In a similar way, S-75 with an rms surface roughness of 3.5 nm was also found to be N-polar with a larger piezo amplitude (figures 6.15(B2) and 6.15(C2)). At the same time, piezo response loop of S-75 (figure 6.15(D)) exhibited higher value of $d_{33(\text{eff})} = 668 \pm 50$ pm/V. Thus S-60 and S-75 together show a much larger piezoelectric response as compared to other reported values on AlN in literature [7, 18]. Herein, it is important to note that any change in the microstructural attributes of the film eventually manifests as a change in the piezoelectric response. The earlier reports on $d_{33(\text{eff})}$ were mostly obtained from specimen synthesized by techniques other than reactive assistive IBSD. Therefore, it can be conclusively stated that $d_{33(\text{eff})}$ values correspond to the microstructural features pertaining to a specific deposition technique.

6.9 Measurement of Longitudinal Piezoelectric Coefficient Using XRD

In order to obtain the piezoelectric response of Ti/AlN/Ti hetrostructure using XRD, first, a symmetric scan was carried out without applying any voltage between the electrodes. The diffraction pattern thus obtained shows only a single peak of wurtzite hexagonal AlN (100) located at 33.0° for S1-60 and 33.07° for S1-75. This indicates that when AlN thin films are grown on Ti-underlayer, their microstructure is textured along preferred direction of growth which happens to

be a -axis in this case. To estimate the degree of orientation, corresponding rocking curves were also recorded for both the specimen. The small FWHM of these rocking curves show that reactive assistive IBSD grown AlN thin films were highly textured along a -axis.

As a second step, copper wires of 0.05 mm diameter were used to provide electrical connection between the top and bottom electrodes using silver epoxy. A 12 V DC power supply was used to apply voltages between the electrodes. The voltage dropped across the electrodes was measured using a digital multimeter. This experimental arrangement is shown in figure 6.16.

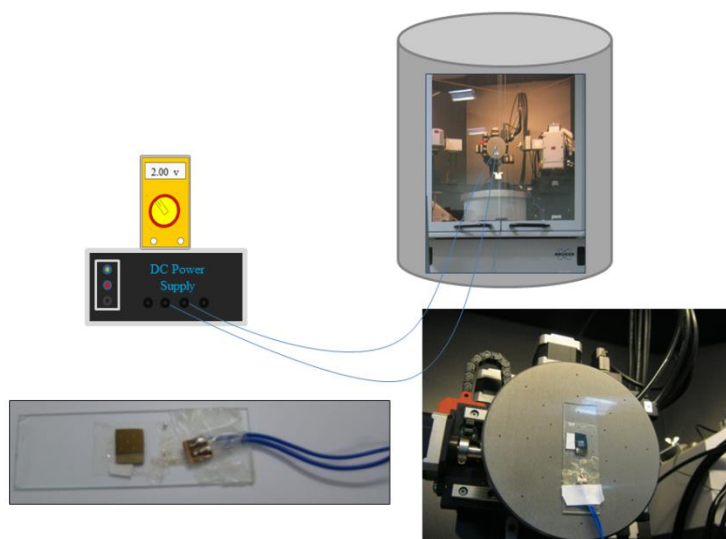


Figure 6.16 Experimental set-up for the measurement of longitudinal piezoelectric coefficient ' d_{33} ' using X-ray diffraction (XRD) on the samples with circular and square top electrodes.

After this, a voltage of 1 V was applied between the electrodes and left for 10 minutes at this voltage. Subsequently, a symmetric scan was performed on the specimen by applying 1V between the electrodes. After the completion of symmetric scan, rocking curve was collected at the same voltage of 1V. This process was repeated by increasing the voltage in steps of 1V and collecting

symmetric diffraction patterns and corresponding rocking curves upto a voltage of 5V. The change in FWHM of peaks obtained in symmetric diffraction pattern and rocking curves thus obtained in the unipolar voltage range of 0-5V were analysed to obtain the value of $d_{33(eff)}$. As only one Bragg peak was observed in symmetric scan, it was fitted with a Voigt-type line profile. The Cauchy and Gauss fractions of this single Bragg peak can then be used to extract the effects of size and strain broadening. It has already been established that a Cauchy-type broadening results from crystallite size while strain broadening is associated with a Gauss profile. Thus after fitting the single Bragg peak in symmetric scan, the FWHM of Cauchy (β_C) and Gauss (β_G) parts of measured profile ($h(2\theta)$) and instrumental profile ($g(2\theta)$) can be used to obtain the FWHM of specimen-broadening profile ($f(2\theta)$) by using following equations [19]:

$$\beta_C^f = \beta_C^h - \beta_C^g \quad (19)$$

$$(\beta_G^f)^2 = (\beta_G^h)^2 - (\beta_G^g)^2 \quad (20)$$

The β_G^f thus obtained can be used to determine weighted-average strain ($\bar{\epsilon}$) present in the specimen using following equation [19]:

$$\bar{\epsilon} = \frac{1}{4} \beta_G^f \cot \theta \quad (21)$$

This procedure was applied to analyse the Bragg peak obtained in symmetric scan for each voltage ranging between 0V to 5V. The microstrain thus obtained was plotted against applied electric field to extract $d_{33(eff)}$. The results of measuring the piezoelectric properties by XRD are presented in figure 6.17 which shows a systematic shift in rocking curve for the (100) reflection of AlN under different voltages applied between the electrodes.

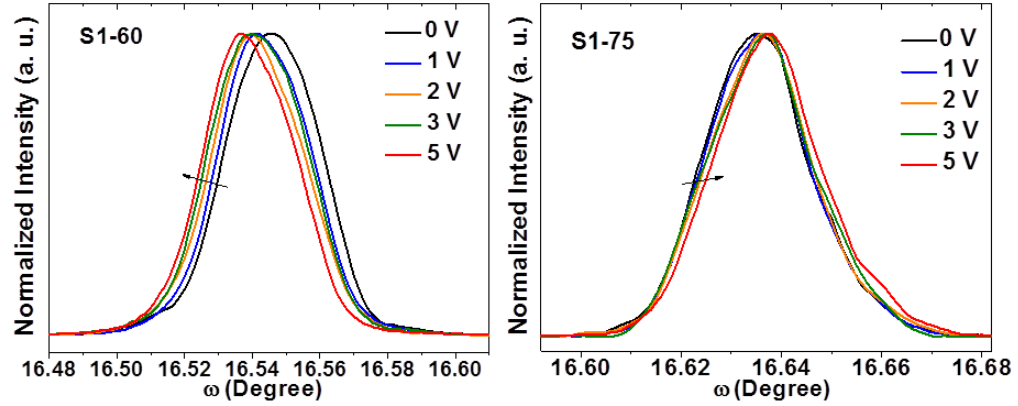


Figure 6.17 Change in the position and full width at half maxima (FWHM) peaks in the rocking curves for the (100) reflection from a crystalline wurtzite hexagonal AlN thin films under the voltage ranging between 0-5V applied between the electrodes.

The values of $d_{33(\text{eff})}$ thus calculated for S-60 and S-75 are shown in figure 6.18.

Inset of figure 6.18 shows the variation of weighted-average strain in the AlN thin film as a function of applied electric field. from equation (20) and (21) are in good agreement with those obtained from PFM measurements.

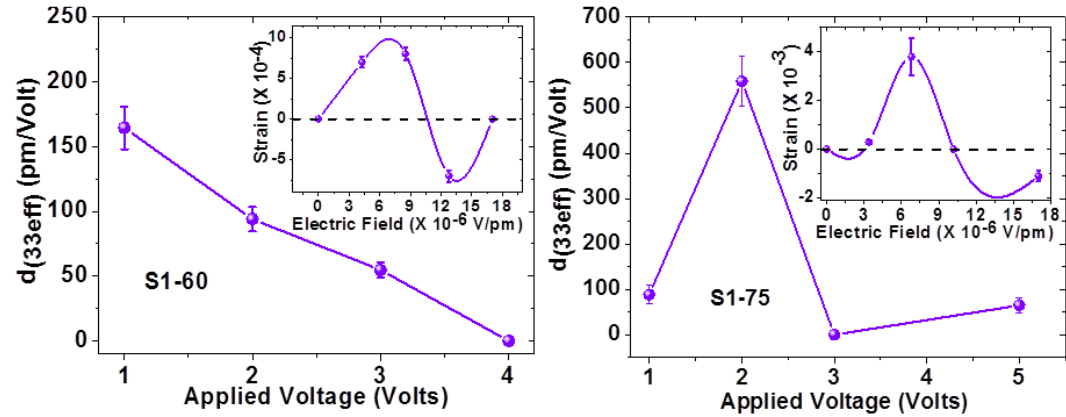


Figure 6.18 Variation of longitudinal piezoelectric coefficient $d_{33(\text{eff})}$ of AlN thin films obtained for 60 minutes (S1-60) and 75 minutes (S1-75). Insets show the change in strain as a function of applied electric field corresponding to S1-60 and S1-75.

6.10 Longitudinal Piezoelectric Coefficient by C-V Measurements

Capacitance of a dielectric thin film is given by the equation [20]:

$$C_0 = \frac{\epsilon_0 \epsilon A}{t} \quad (22)$$

Where ϵ_0 is the permittivity of vacuum, ϵ is the relative permittivity or dielectric constant of the thin film, t is the thickness of the thin film, and A is the area of the capacitor.

By measuring the capacitance of AlN thin film using equation (22), $d_{33(\text{eff})}$ can also be calculated. Figure 6.19(A) shows an AlN thin film sandwiched between two circular electrodes forming Ti/AlN/Ti heterostructure. When a DC voltage is applied between the electrodes, thickness of the film will either expand

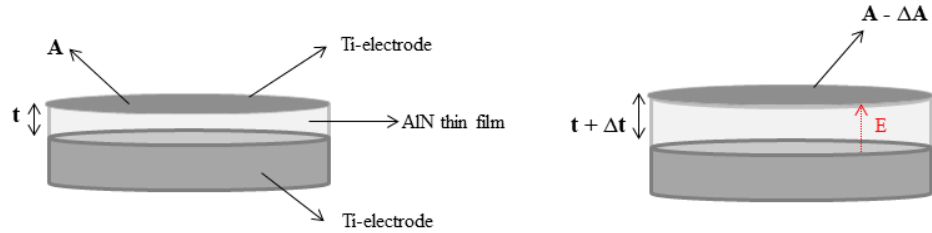


Figure 6.19 Piezoelectric response of AlN thin films sandwiched between two titanium electrodes. (A) no voltage between the electrodes, (B) when voltage is applied between the electrodes.

or contract along with its area depending on the polarity on its surface [10]. Then using equation (6), strain in thin film thickness can be calculated as following:

$$\frac{\Delta t}{t} = V d_{33} \quad (23)$$

This modification in film dimensions will be translated into a change in its capacitance whose approximate value can be calculated by using formula for parallel plate capacitor:

$$C_V = \epsilon_0 \epsilon \frac{(A - \Delta A)}{(t + \Delta t)} = \frac{\epsilon_0 \epsilon A}{t} \frac{\left(1 - \frac{\Delta A}{A}\right)}{\left(1 + \frac{\Delta t}{t}\right)}$$

Using equation (22),

$$C_V = C_0 \frac{\left(1 - \frac{\Delta A}{A}\right)}{\left(1 + \frac{\Delta t}{t}\right)} \quad (24)$$

Consider,

$$\frac{\Delta t}{t} = -\delta \frac{\Delta A}{A} \quad (25)$$

Equation (24) can then be written as following:

$$\frac{\Delta t}{t} = \frac{(1 - C_r)}{(C_r - \delta^{-1})} C_r \quad (26)$$

This equation (26) can be used to calculate the change in thickness direction [21, 22]. Strain in thickness thus calculated can then be plotted as a function of applied electric field, slope of which yields the value for $d_{(33eff)}$. Figure 6.20 shows the C-V curves obtained for both S1-60 and S1-75 samples.

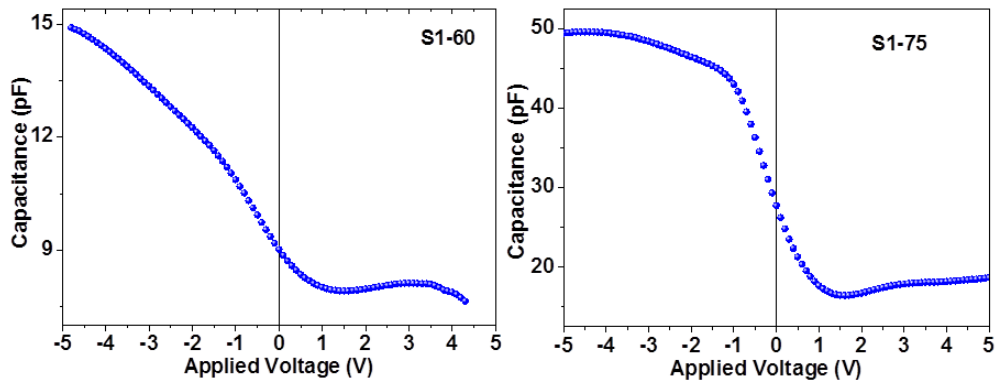


Figure 6.20 Capacitance-voltage (C-V) curves of AlN thin films grown for 60 minutes (S1-60) and 75 minutes (S1-75).

These curves were further analysed to obtain the strain in thickness of S1-60 and S1-75 thin film specimen using equation (26). Value of $d_{(33eff)}$ thus obtained are displayed in figure 6.21 and are in good agreement with the values obtained from PFM and XRD techniques.

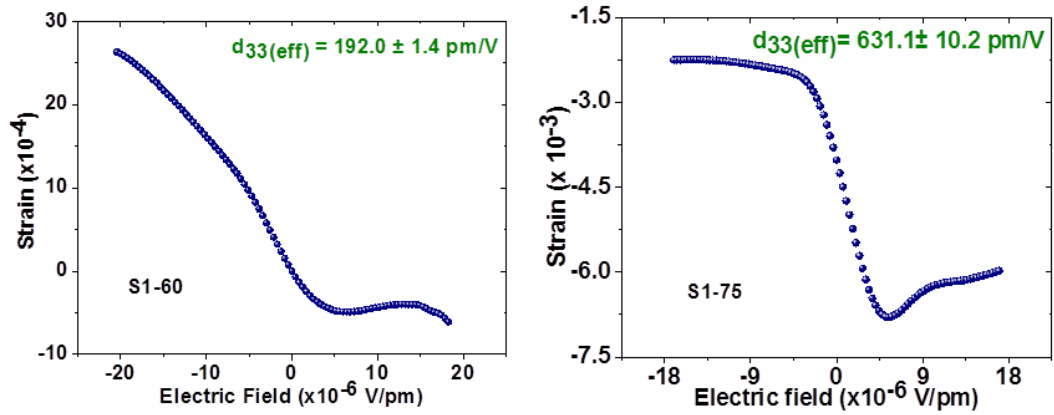


Figure 6.21 Longitudinal piezoelectric coefficient $d_{(33eff)}$ of AlN thin films grown for 60 and 75 minutes (S1-60 and S1-75). For S1-75, a negative strain axis indicated that the direction of applied electric field and resulting strain in thickness are in opposite directions.

6.11 Origin of High Piezoelectricity in a-axis Oriented AlN Thin Films

Since IBSD has inherent ion beam induced effects, presence of charged point defects, mainly V_{Al}^- and V_N^+ in the film microstructure, is quite possible. To confirm the presence of these charged point defects, PL measurements were carried out on S-60 and S-75. Both specimens were found to exhibit nearly similar spectra, shown in figure 6.22, substantiating the presence of V_{Al}^- and V_N^+ . PL peak centered at 2.60 eV is the primary indicator of V_N^+ while that at 2.8 eV is attributed to isolated V_{Al}^- .

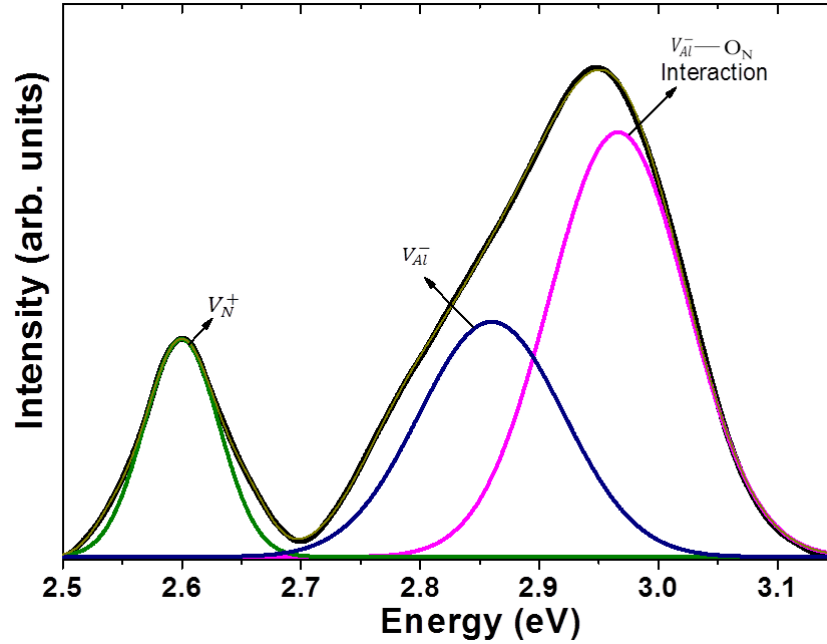


Figure 6.22 Photoluminescence (PL) measurements of S1-60 and S1-75 confirming the presence of V_{Al}^- and V_N^+ .

The intensity as well as area under each peak remains same for both samples (figure 6.22) implying that they have defects of similar nature with comparable concentrations available in their microstructure. This behaviour, observed by XRD and PL measurements together (figures 6.12 and 6.22), can be explained by the formation of randomly oriented AlN grains, point defects V_{Al}^- , V_N^+ which nucleate at the AlN/Ti interface and align themselves in the preferred direction of growth with the increase in film thickness forming a pseudomorphic heteroepitaxial thin film [23]. It is expected that this could be the origin of enhanced $d_{33(\text{eff.})}$ values. In order to justify the role of V_{Al}^- and V_N^+ towards enhanced piezoelectric response of reactive assistive IBSD grown AlN thin films, a mechanism based on these charged defects in the dielectric continuum and their response to the applied bias voltage is being proposed.

Point defects in their charged state significantly influence the microstructural polarization and associated molecular field intensities in a solid. Also, these charged defects order themselves in the growth direction whenever circumstances permit and become the integral part of textured thin films [14]. But to maintain the stoichiometry and preserve electrical neutrality, vacancy defect concentration of Al^+ and N^- -sublattice must be balanced. This is possible when both of these sublattices have vacancies forming Schottky and Frankle defects [14]. Herein, a mechanism based on these defects is being proposed to account for the enhanced piezo response as depicted in figure 6.23.

The pseudomorphic heteroepitaxial growth of an a-axis oriented AlN thin film on Si(100) substrate is illustrated in Figure 6.23(A). When an N^- -ion is absent from its normal lattice site, a vacancy is created with a virtual opposite charge of +1, V_N^+ as shown in figure 6.23(B-i). The primary assumption here is based on Born's classical model. A number of researchers have extended this theoretical model to explain the defect properties of these crystals and collection of these works are extensively reviewed by Barr and Lidiard et al. [24]. According to them, the nearest Al^+ ions surrounding V_N^+ in the form of a tetrahedron, are displaced slightly outwards due to repulsive coulombic interaction. As each of the N^- ion is shared between four such tetrahedras, presence of a V_N^+ and consequent displacement of Al^+ ions around V_N^+ will create a hollow space between them with net positive charge +q on its surface as shown in figure 6.23(B-ii).

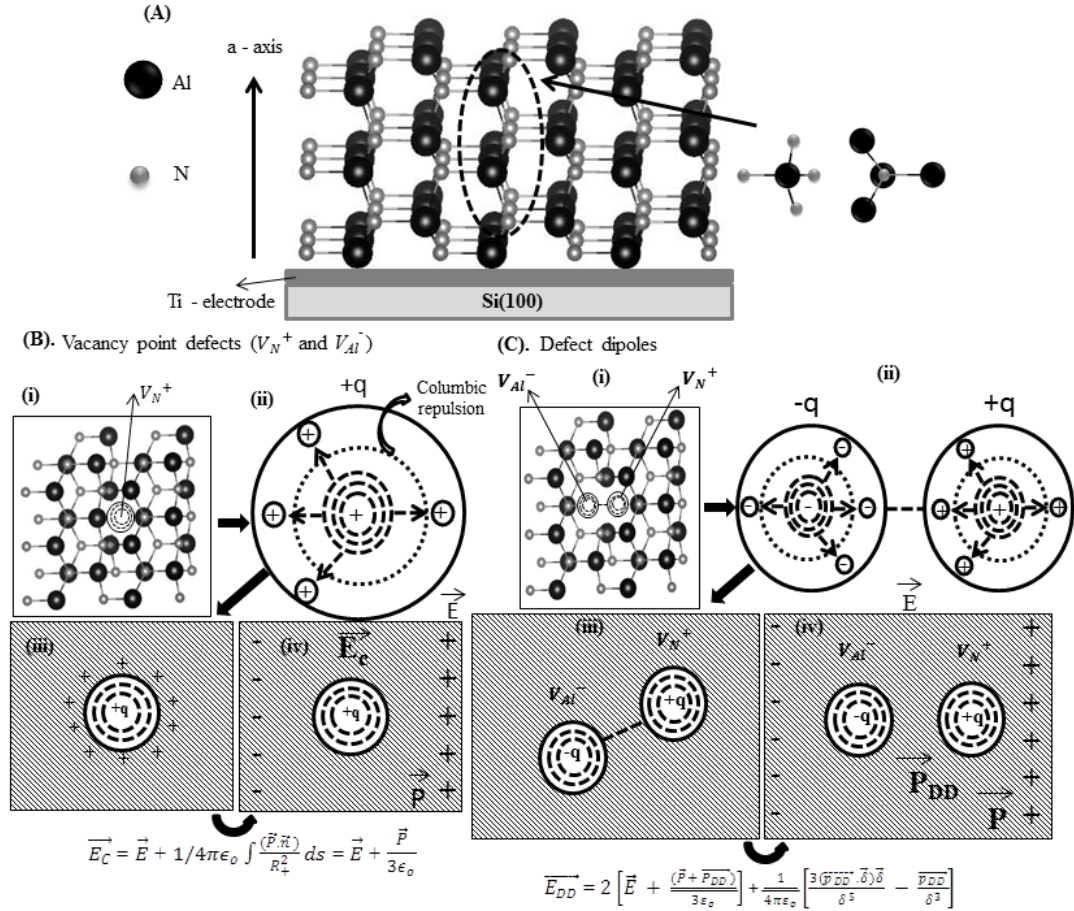


Figure 6.23 Model for charged vacancy induced enhancement in lattice polarization, (A) a-axis oriented AlN/Ti/Si(100) heterostructure, (B) V_{Al}^- and V_N^+ as spherical cavities in a dielectric, (C) Formation of defect dipoles by the presence of two spherical cavities of opposite surface charge at the nearest possible distance.

This hollow site can then be treated as a spherical cavity of radius R_+ in a dielectric continuum as suggested by Jost et al. [25]. Presence of such spherical cavities can lead to a gain in polarization and hence in the internal electric field of the lattice. This scenario is depicted in figure 6.23(B-iii). In a similar way, a hollow site created by V_{Al}^- can also be treated as a spherical cavity of radius R_- with a net charge of $-q$ bound on its surface. When external electric field is applied, a macroscopic electric field \vec{E} gets established in the dielectric medium

and polarizes the lattice in the direction of the field with polarization vector \vec{P} . In addition to this, every spherical cavity incorporated inside the dielectric medium also experiences a larger local polarization field \vec{E}_C as given by [26]:

$$\vec{E}_C = \vec{E} + 1/4\pi\epsilon_o \int \frac{(\vec{P} \cdot \vec{n})}{R_+^2} ds = \vec{E} + \frac{\vec{P}}{3\epsilon_o} \quad (27)$$

Where \vec{s} is the surface area vector, \vec{n} is the vector normal to the surface and ϵ_o is the permittivity of free space. This is shown in figure 6.23(B-iv). If there are m such cavities, then the net internal field in the film will be given by:

$$\vec{E}_N = \vec{E} + m(\vec{E}_C) = (m + 1)\vec{E} + m\frac{\vec{P}}{3\epsilon_o} \quad (28)$$

This enhancement in the internal macroscopic field will exert an additional force on the surrounding ions of the lattice. Consequently, they experience larger elastic displacements which depend strongly on the elastic strength of the vacancy as suggested by Hardy and Lidiard [18]. Thus the film microstructure undergoes a substantial piezoelectric strain on the application of external electric field which gets translated into large $d_{33(eff)}$ values.

In another possibility, a V_N^+ can encounter a V_{Al}^- at the nearest possible distance (figure 6.23(C-i)). In this case, they can interact with each-other forming a ‘*defect dipole*’ as shown in figure 6.23(C-ii and C-iii). When external electric field is applied, these defect dipoles get oriented in the direction of the field with a net polarization vector \vec{P}_{DD} . If there are m^* such defect dipoles, all of them will

contribute an additional electric field at a position $\vec{\delta}$ inside the dielectric lattice given by [26]:

$$\vec{E}_N^* = (2m^* + 1)\vec{E} + \frac{2m^*(\vec{P} + \vec{P}_{DD})}{3\epsilon_o} + \frac{m^*}{4\pi\epsilon_o} \left[\frac{3(\vec{p}_{DD} \cdot \vec{\delta})\vec{\delta}}{\delta^5} - \frac{\vec{p}_{DD}}{\delta^3} \right] \quad (29)$$

Where dipole moment $\vec{p}_{DD} = q\xi$, ξ is the smallest possible distance between the spherical cavities. This scenario is shown in figure 6.23(C-iv). This brings about lattice contributing towards enhanced piezoelectric strain and $d_{33(eff)}$ values. In a typical situation, a combination of cases shown in figure 6.23(B) and 6.23(C) is likely to take place. As S-75 has a higher degree of orientation, simultaneous occurrence of both the phenomena is expected to be the genesis of its higher piezoelectric response as compared to S-60. As $d_{33(eff)}$ of S1-60 and S1-75 is similar to that of S-60 and S-75, this model can be applied for S1-60 and S1-75 also confirming the microstructural uniformity of reactive assistive IBSD grown *a*-axis oriented AlN thin films.

6.12 Conclusion

In summary, *a*-axis oriented AlN thin films were grown in the form of AlN/Ti/Si(100) and Ti/AlN/Ti/Si(100) hetrostructures by varying deposition time of AlN to 60 and 75 minutes using reactive assistive IBSD. Films thus grown were investigated for their piezoelectric response using three different techniques, namely, PFM, XRD and C-V. Phase and amplitude scans of PFM measurements on these specimens clearly establish that both the variants of AlN thin films under investigation are N-polar exhibiting high piezoelectric amplitude. Values of piezoelectric coefficient $d_{33(eff)}$ obtained from all the three techniques are found to

be in good agreement with each-other. The origin of this enhanced piezoelectric response of reactive assistive IBSD grown a-axis oriented AlN thin films is attributed to the charged vacancies incorporated into film microstructure during growth process. These vacant sites act as spherical cavities in a dielectric continuum and interact among themselves to form defect dipoles. Presence of these spherical cavities and defect dipoles enhance the lattice polarization manifold and film undergoes substantial piezoelectric strain with enhanced $d_{33(eff)}$ values. In a nutshell, this investigation demonstrates the technical feasibility of synthesizing highly a-axis oriented AlN thin films using reactive assistive IBSD to obtain enhanced $d_{33(eff)}$. This value is substantially higher compared to other piezoelectric thin films currently being used.

References

- [1] B. Jaffe, Piezoelectric Ceramics, Elsevier Science, 2012.
- [2] A.A. Vives, Piezoelectric Transducers and Applications, Springer Berlin Heidelberg, 2013.
- [3] J. Yang, An Introduction to the Theory of Piezoelectricity, Springer US, 2006.
- [4] M.S. Vijaya, Piezoelectric Materials and Devices: Applications in Engineering and Medical Sciences, CRC Press, 2016.
- [5] J. Tichý, J. Erhart, E. Kittinger, J. Přívratská, Fundamentals of Piezoelectric Sensorics: Mechanical, Dielectric, and Thermodynamical Properties of Piezoelectric Materials, Springer Berlin Heidelberg, 2010.

- [6] F. Akasheh, T. Myers, J.D. Fraser, S. Bose, A. Bandyopadhyay, Development of piezoelectric micromachined ultrasonic transducers, *Sensors and Actuators A: Physical*, 111 (2004) 275-287.
- [7] M.-A. Dubois, P. Muralt, Properties of aluminum nitride thin films for piezoelectric transducers and microwave filter applications, *Applied Physics Letters*, 74 (1999) 3032-3034.
- [8] N. Sinha, G.E. Wabiszewski, R. Mahameed, V.V. Felmetger, S.M. Tanner, R.W. Carpick, G. Piazza, Piezoelectric aluminum nitride nanoelectromechanical actuators, *Applied Physics Letters*, 95 (2009) 053106.
- [9] Y. Kumashiro, *Electric Refractory Materials*, Taylor & Francis, 2000.
- [10] X. Wang, J. Zhou, J. Song, J. Liu, N. Xu, Z.L. Wang, Piezoelectric Field Effect Transistor and Nanoforce Sensor Based on a Single ZnO Nanowire, *Nano Letters*, 6 (2006) 2768-2772.
- [11] P. Muralt, N. Ledermann, J. Paborowski, A. Barzegar, S. Gentil, B. Belgacem, S. Petitgrand, A. Bosseboeuf, N. Setter, Piezoelectric micromachined ultrasonic transducers based on PZT thin films, *IEEE Transactions on Ultrasonics, Ferroelectrics, and Frequency Control*, 52 (2005) 2276-2288.
- [12] M.-H. Zhao, Z.-L. Wang, S.X. Mao, Piezoelectric Characterization of Individual Zinc Oxide Nanobelt Probed by Piezoresponse Force Microscope, *Nano Letters*, 4 (2004) 587-590.
- [13] H. Morkoç, *Handbook of Nitride Semiconductors and Devices*, Materials Properties, Physics and Growth, Wiley, 2009.
- [14] R.J.D. Tilley, *Defects in Solids*, Wiley, 2008.

- [15] N. Sharma, K. Prabakar, S. Ilango, S. Dash, A.K. Tyagi, Application of dynamic scaling theory for growth kinetic studies of AlN-thin films deposited by ion beam sputtering in reactive assistance of nitrogen plasma, *Applied Surface Science*, 347 (2015) 875-879.
- [16] S.C. John, Ion-Assisted Sputter Deposition, *Philosophical Transactions: Mathematical, Physical and Engineering Sciences*, 362 (2004) 103-116.
- [17] B.J. Rodriguez, A. Gruverman, A.I. Kingon, R.J. Nemanich, Piezoresponse force microscopy for piezoelectric measurements of III-nitride materials, *Journal of Crystal Growth*, 246 (2002) 252-258.
- [18] C. Cibert, P. Dutheil, C. Champeaux, O. Masson, G. Trolliard, F. Tétard, A. Catherinot, Piezoelectric characteristic of nanocrystalline AlN films obtained by pulsed laser deposition at room temperature, *Applied Physics Letters*, 97 (2010) 251906.
- [19] M. Birkholz, *Thin Film Analysis by X-Ray Scattering*, Wiley, 2006.
- [20] K. L. Chopra, *Thin Film Device Applications*, Springer US, 2012.
- [21] M.A. Ahmad, R. Plana, Piezoelectric Coefficients of Thin Film Aluminum Nitride Characterizations Using Capacitance Measurements, *IEEE Microwave and Wireless Components Letters*, 19 (2009) 140-142.
- [22] T.V. Hemert, D. Sarakiotis, S. Jose, R.J.E. Hueting, J. Schmitz, Exploring capacitance-voltage measurements to find the piezoelectric coefficient of aluminum nitride, in: 2011 IEEE ICMTS International Conference on Microelectronic Test Structures, 2011, pp. 69-73.

- [23] C. Duquenne, M.A. Djouadi, P.Y. Tessier, P.Y. Jouan, M.P. Besland, C. Brylinski, R. Aubry, S. Delage, Epitaxial growth of aluminum nitride on AlGaIn by reactive sputtering at low temperature, *Applied Physics Letters*, 93 (2008) 052905.
- [24] L.W.Barr, A.B. Lidiard, Defects in Ionic Crystals, *Physical Chemistry: An Advanced Treatise X*(1968).
- [25] W. Jost, Diffusion and Electrolytic Conduction in Crystals (Ionic Semiconductors), *The Journal of Chemical Physics*, 1 (1933) 466-475.
- [26] J.R. Reitz, F.J. Milford, R.W. Christy, *Foundations of Electromagnetic Theory*, Pearson/Addison-Wesley, 2009.

Chapter 7

Summary and Future Scope

Present thesis addresses two important aspects. These are:

- (I). Deposition of a-axis oriented AlN thin films by reactive assistive ion beam sputter deposition (IBSD).
- (II). Piezoelectric response of these highly a-axis oriented AlN thin films grown by reactive assistive IBSD.

A summary highlighting the key finding of this work is as follows:

- Growth kinetics of AlN thin films deposited by reactive assistive IBSD has been studied in the frame work of dynamic scaling theory (DST).
- For AlN thin films grown in reactive assistance of N^+/N_2^+ ions, DST confirms surface diffusion as the major roughening phenomena and bulk diffusion leads the smoothening of the film surface.
- To grow wurtzite hexagonal AlN thin films textured along a-axis, main sputter ion energy, assisted ion energy and substrate temperature were optimized at 500 eV, 90 eV and 400°C respectively for a deposition of 60 minutes on Si(100) substrate.
- At these optimized parameters, phase fraction of AlN formed on the surface was estimated to be 74 at. % and 89 at. % at a depth of 50 nm using XPS.

- At optimized parameters, AlN was found to possess an optical band gap of 5.2 eV with an energy tail of 775 meV, refractive index $\sim 2.2 \pm 0.3$ and extinction coefficient 0.143 ± 0.08 .
- Two variants of AlN thin film based heterostructures with Ti top and bottom electrodes were deposited. For this, deposition time of AlN thin film was varied as 60 and 75 minutes.
- Using PFM, both the variants of AlN thin films were found to be N-polar predominantly exhibiting $d_{33(eff)} = 206 \pm 20$ pm/V and 668 ± 60 pm/V for AlN thin film grown for 60 and 75 minutes respectively.
- In XRD investigations, full width at half maxima (FWHM) of the peak pertaining to (100) reflection was used to obtain *microstrain vs. applied DC voltage* to determine the variation of $d_{(33eff)}$. These values of $d_{(33eff)}$ match well with those obtained by PFM.
- By C-V measurements, $d_{(33eff)}$ of AlN thin films were found to be 192 ± 1.4 pm/V and 631 ± 10.2 pm/V for 60 and 75 minutes of deposition respectively. These values were in good agreement with those obtained by PFM and XRD.
- A physical model based on charged vacancies induced enhanced polarization has been proposed for reactive assistive IBSD grown a-axis oriented AlN thin films.

♦ **Implications:**

- Demonstration of reactive assistive IBSD to grow highly textured AlN thin films along a-axis will have decisive impact on scientific

community to adopt this method for the textured growth of other nitrides.

- DST formalism to unravel dynamics of growth and the underlying governing phenomena can be applied to other reactive PVD techniques like magnetron sputtering.
- Due to direct and controlled exposure of film surface to the reactive ions in IBSD, growth of suitable multilayer systems for band-gap engineering will be possible.
- Growth of other bulk piezoelectric materials in thin film form to exhibit enhanced piezoelectric response can be attempted.

♦ ***Future Directions:***

- Curie temperature of reactive assistive IBSD grown *a*-axis oriented AlN thin films should be studied to establish it as a useful material as a transducer in high temperature environments.
- A simulation study can be carried out on the proposed model for charged defect induced enhanced piezoelectric effect in *a*-axis oriented AlN thin films.
- Piezoelectric response as well as Curie temperature has to be studied when AlN is sandwiched between different electrodes like, TiN etc. and by depositing heterolayer unit repetitively.
- After standardizing on silicon, piezoelectric response of AlN heterostructures can be studied on flexible substrates.
- Effect of doping in AlN thin films' piezo response can be studied.